# PART-SCALE THERMAL AND THERMOMECHANICAL FINITE ELEMENT MODELING, AND MODEL VALIDATION FRAMEWORK FOR THE LASER POWDER BED FUSION PROCESS

By

ALAAELDIN OLLEAK

A dissertation submitted to the

School of Graduate Studies

In partial fulfillment of the requirements

For the degree of

Doctor of Philosophy

Graduate Program in Industrial and Systems Engineering

Written under the direction of

Zhimin Xi

And Approved by

_____

_____

_____

_____

New Brunswick, New Jersey

October 2020

**ABSTRACT OF THE DISSERTATION**

PART-SCALE THERMAL AND THERMOMECHANICAL FINITE ELEMENT MODELING, AND MODEL VALIDATION FRAMEWORK FOR THE LASER POWDER BED FUSION PROCESS

by Alaaeldin Olleak

Dissertation Director:

Zhimin Xi

Quality and reliability of additively manufactured (AM) parts using the Laser Powder Bed Fusion (LPBF) process are greatly affected by the thermal history during the manufacturing process. Prediction of thermal history, residual stresses, and distortions of a part during the LPBF process is critical to understand how the process parameters influence the process stability and mechanical properties of the part. Finite element modeling of the LPBF process at part-scale is challenging and requires massive computational time and resources. These models are computationally infeasible if they are not associated with simplifications in the mesh configuration and the heat source model, or with the reduced domain size. Due to the complexity of the computational model itself, uncertainties during the LPBF process are not systematically studied, and their effects on quality and reliability of the parts are not characterized.

The dissertation overcomes the computational expensiveness associated with modeling of the LPBF process on a part-scale level. It presents the use of different adaptive

remeshing techniques that enable the thermal and thermomechanical simulations at the part-scale level without the sacrifice in accuracy. As a result, part-scale thermal and thermomechanical finite element modeling are computationally feasible. This is the first work where an adaptive remeshing framework was developed for the LPBF process, based on an existing general-purpose implicit solver and the tetrahedral mesh. In particular, the tetrahedral mesh can represent parts with complex structures using less elements than the existing remeshing technique. The thermal process modeling presents models for relatively large parts considering different process parameters, and the models can predict location-dependent melt pool size and the lack-of-fusion porosity. The thermomechanical process modeling predicts the thermally induced residual stresses, strains, and distortions for different parts. The model predictions find similar trends with the experimental results from the literature along with achieving a significant reduction in the computational time compared to the state-of-the-art models without using the adaptive remeshing. Furthermore, a general calibration and validation framework for the LPBF process was developed based on multi-fidelity models and limited experimental data. The framework enables the development of highly efficient and accurate models for melt pool predictions under various sets of process parameters through the seamless integration of finite element modeling, machine learning methods, and the model calibration and validation methods. Effectiveness of the framework is demonstrated by experimental data under different sets of process parameters available in the literature.

# Dedication

To my family

# ACKNOWLEDGEMENTS

First and foremost, all praises and gratitude are due to Allah.

I would like to thank my PhD advisor, Dr. Zhimin Xi, whose continuous support, understanding, and encouragement always kept me motivated and eager for achievements. I would like to thank Prof. Elsayed Elsayed, Prof. Yuebin Guo, and Prof. Weihong Guo for their feedback and serving on my dissertation committee. I would also like to acknowledge the support I received from Prof. Mohsen Jafari during my stay at Rutgers.

I am also grateful to the Ansys Nonlinear Adaptivity and Additive Manufacturing teams for their help and software support: Jin Wang, Dave Conover, Vivek Premkumar, Siddhartha Mukherjee, Zack Francis, Joey Xie, and Ryan Gordon. Beside spending two wonderful internships with Ansys, the knowledge and experience I acquired helped me overcome the difficulties in this work.

I am grateful to Prof. Hasan El-Hofy and Prof. Amr Eltawil from E-JUST for their continuous support. I would like to thank all professors at Rutgers university, E-JUST, and Alexandria university who taught me and gave me knowledge.

Last, but not least, I would like to thank my parents who have been an integral part to my success. I would like to express my deepest gratitude to my beloved wife, Aalaa, for her love, patience, support and understanding.

# Table of Contents

# LIST OF TABLES

# LIST OF FIGURES

# 1. Introduction

## *1.1. Laser Powder Bed Fusion Process*

Laser Powder Bed Fusion (LPBF) is an additive manufacturing (AM) process that falls under the category of Powder Bed Fusion (PBF). LPBF enables the production of metallic parts that have complex geometry without the need for the special tooling and multiple processes that traditional manufacturing techniques require, Figure 1.1. Furthermore, LPBF enables manufacturing parts from difficult-to-machine materials, such as Inconel-based [1], titanium and tungsten alloys [2].

The process starts by slicing the 3D CAD geometry file of the parts into multiple layers and a G-code that includes the laser beam movement for the entire build is generated. The G-code includes information about the process parameters such as the laser power and scanning speed and generated based on the layer thickness, hatch spacing, and scanning strategies. During the process, the laser beam moves over the powder bed where the powder particles absorb the laser energy and start to melt forming a melt pool. For perfect bonding, the melt pool depth should always be larger than the layer thickness and its width should be larger than the hatch spacing. After the layer scanning is complete, a new powder layer is added using a recoater. Even though LPBF can work with different metals, a process window for each metal should be determined since their thermal conductivity, melting point, surface tension, and liquid-state viscosity differ [3].

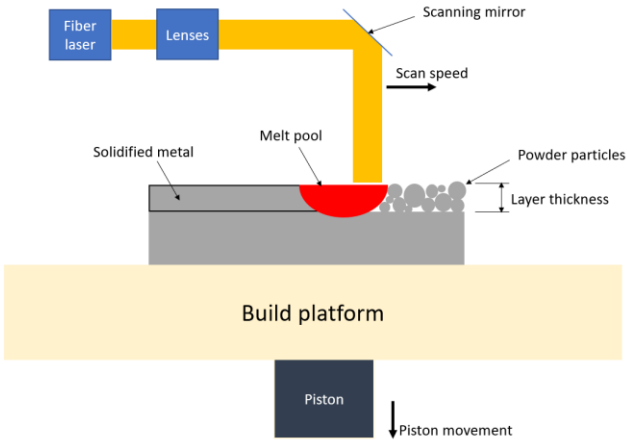


**Figure 1. 1.** Schematic of LPBF process and the melt pool.

The LPBF process parameters include: (1) laser related parameters: laser beam spot diameter $D_{spot}$ (µm), and laser power P (Watt), (2) scan-related parameters: laser scanning speed $V_c$ (mm/s), and hatch spacing h (mm), (3) powder-related parameters: particle shape, size, and distribution, (4) temperature related parameter: powder preheat temperature, and (5) other parameters that include layer thickness, scanning strategy, Figure 1.2 , and part's build orientation [5]. It had been reported that over 130 parameters influence the quality of the final part [6]. There are interactions among these parameters and they significantly affect the process behavior and part quality.

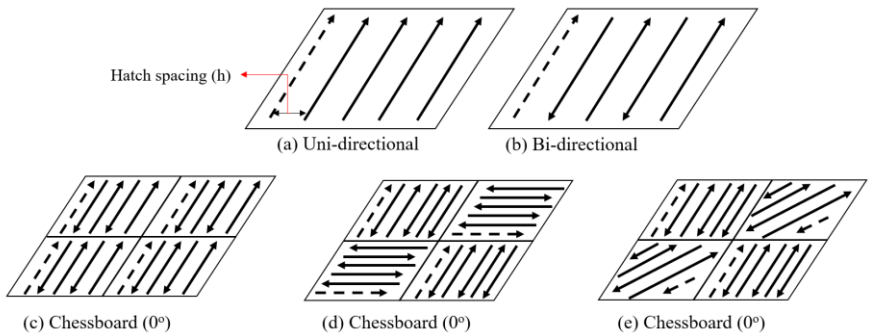


**Figure 1. 2.** Different scanning strategies used for LPBF

## *1.2. Manufactured Part Quality*

### 1.2.1. Porosity

Porosity is one of the important factors that greatly affect the part's mechanical properties. In several studies, the porosity was found to have a great influence on the parts reliability and material fatigue strength since the pores are potential crack initiation points [7, 8]. There are two formation mechanisms of the pores inside the manufactured part. The first formation mechanism takes place when an excessive energy is applied to the powder, causing vaporization of the low evaporating temperature alloy constituents. This vaporization creates a gas bubble inside the melt pool that remains inside the produced part, Figure 1.3. Because of the high solidification rate of the melt pool, the time is not sufficient for this bubble to escape from the melt pool, forming a keyhole [9]. Another pore formation mechanism, called lack of fusion porosity, takes place due to the incomplete melting of the powder due to insufficient energy input [9], or large scan spacing [4]. This porosity type leads to a significant reduction in parts' fatigue and tensile strength since the unmolten powder particles are large and they exist at the interlayer connections. Measuring porosity can be done using the simple Archimedes method as in [4, 7, 10], or by using computed tomography (CT) systems as in [8, 11]. The CT system can show the pores size and their distribution, however, the minimum pore size that can be detected is limited by the minimum voxel size. Reducing the minimum voxel time makes this measurement process expensive.

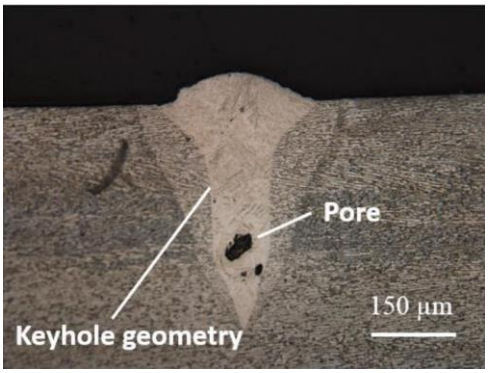


**Figure 1. 3.** Pores due to excessive energy density [9]

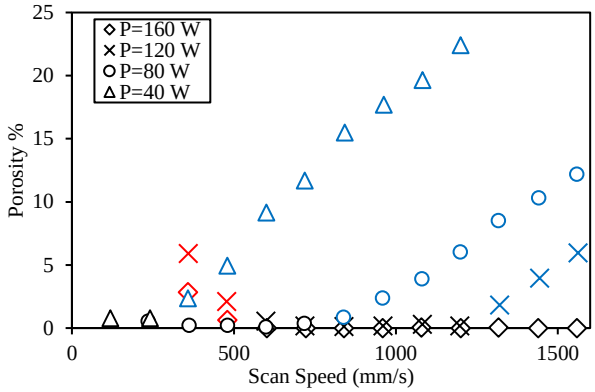


**Figure 1. 4.** Effect of scan speed and power on the porosity at laser spot 100 µm, and layer thickness 0.03 µm (Reproduced from [4])

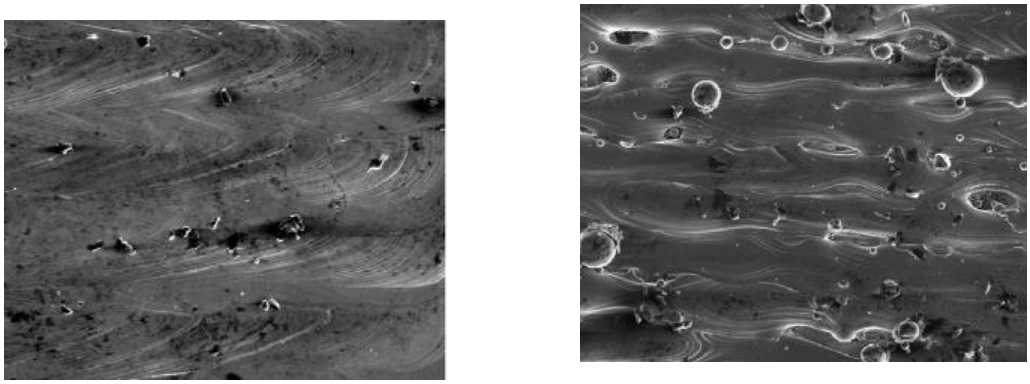

a) P=160 W, V=360 mm/s b) P=160 W, V=1440 mm/s

**Figure 1. 5.** SEM images showing the effect of scanning speed on the porosity [4]

Figure 1.4 clearly shows the interaction between the laser power and scan speed and their effect on the porosity. The trend of the porosity is firstly decreasing, where the keyhole pores are formed, then constant where parts are fully dense, and finally increasing with more lack-of-fusion porosity. The high energy density caused at high power levels 160 W and 120W and low scanning speed results in higher porosity and reduced density. That clearly indicates that this type of porosity was created due to the excessive energy given to the powder (red markers). At high scanning speeds, energy density is reduced, leading to incomplete melting of the particles forming lack of fusion porosity (blue markers). The lack of fusion porosity becomes much higher at reduced laser power (40W). Figure 1.5 shows the differences between the two porosity formation mechanisms.

Porosity can also be influenced by the scanning strategies. The effect of uni-directional and bi-directional scanning strategies was investigated in [10]. Porosity results from bidirectional scanning strategies could be slightly reduced from 0.65% to 0.4% compared to unidirectional scanning strategies. Residual heat effect due to the insufficient cooling time between every two consecutive scanning tracks could be the reason. A further reduction to 0.1% could be achieved by alternating the scanning tracks angle alternation by $90^{o}$.

Table 1.1 shows the porosity results from other studies where the chess-board scanning strategies were investigated. It was also found that bidirectional scanning strategy with $90^{o}$ alternation is the optimum in terms of porosity. These findings were also observed in [10, 12]. The cases involving alternating angle of $45^{o}$ between layers result in higher porosity than $90^{o}$, but less than that of $0^{o}$. The effect that the scanning length on the porosity is

obvious; there is a decreasing trend in the porosity as the scanning length increases (cases 3, 4, 5, and 2 in Table 1.1). This increase could be due to the keyholing porosity caused by residual heat effect. The results of the in-layer alternating angle of the chessboard scanning strategies show that the 45$^{o}$ alternating angle does not reduce porosity. These findings were justified by the residual heat effect which was high for 45$^{o}$ cases due to the shorter scanning length at blocks corners. However, the authors did not show how pores are distributed which can support the hypothesis. Even though the 45$^{o}$ alternating angle looks unfavorable for porosity, this scanning strategy may have a positive effect on the residual stresses.

Table 1. 1 **:** Effect of chessboard scanning strategy on the porosity [14]

| Case | In-layer strategy | Angle | Scan length (mm) | Porosity % |
|---|---|---|---|---|
| 1 | Bi-directional | 45 | 30 | 0.3 |
| 2 | Bi-directional | 90 | 30 | 0.1 |
| 3 | Chess-board (0) | 90 | 2 | 0.9 |
| 4 | Chess-board (0) | 90 | 3 | 0.3 |
| 5 | Chess-board (0) | 90 | 5 | 0.2 |
| 6 | Chess-board (45) | 90 | 5 | 0.3 |
| 7 | Chess-board (90) | 90 | 5 | 0.1 |

For certain cases, high porosity up to 50% is considered favorable. These cases include porous implants where pores are needed for implants to integrate with the human cells, and when the part weight needs to be minimized. In such cases, the hatch spacing plays an important role in defining the material porosity. The minimum pore size must be larger than particles size. According to Zhang et al. [13], a pore size of 400 µm could be achieved with a scan line spacing of 700 µm, with a laser that has a power of 130 W and spot

diameter of 150 μm. The effect that porosity has on mechanical strength and post processing methods that reduce porosity will be discussed in later sections.

### 1.2.2. Microstructural evolution

Investigating the microstructural evolution during LPBF is crucial since it offered a good understanding between LPBF process parameters and manufactured part quality, mechanical properties, and strength [10]. The size, fraction, and arrangement of the microstructure control the elastic modulus, tensile and fatigue strength, ductility, and oxidation resistance for manufactured part [14]

For instance, Ti-6Al-4V is a two-phase α+β alloy, with 6% aluminum and 4% vanadium, where the aluminum acts as α phase stabilizer, and the vanadium acts as β phase stabilizer. This alloy microstructure is controlled by the part thermomechanical history, and heat treatment operations. The effect of the microstructure arrangement, and size on the material properties is explained in [14]. In addition to that, the microstructure arrangement can result in anisotropy in the manufactured parts [15].

Thijs et al. [10] investigated the scan speed, hatch spacing, and scanning strategies on the manufactured part microstructure. Because of the high temperature gradients during the LPBF process, a fine micro-structure consisting of martensitic primary α phase formed within prior β grains. The grains in most cases are aligned or tilted with the building direction following the maximum heat flux direction coming from the melt pool.

The top view of the micro-structure from the bi-directional scanning strategy is shown in Figure 1.6. Bi-directional scanning strategy results in individual tracks that are tilted with

opposite angles, each track width equals to the hatch spacing (75 µm). The dependence between the grain inclination angle and scan vector direction is due to heat conduction direction.

The effect of scanning speed on micro-structure is also shown in Figure 1.6: a, b, and c. Reducing scanning speed results in porosity due to excessive energy input. Furthermore, scanning at low scanning speeds may result in melt pool instabilities that lead wider track width varying between 62 µm and 232 µm. Reducing hatch distance results in higher energy density. Therefore, more porosity and smaller melt pool width are achieved. Figure 1.6-d shows the existence of pores compared to larger hatch distance, Figure 1.6: a and e. Furthermore, individual track width also depends on hatch distance. Thus, the hatch distance can be used to control the individual grain width in the top view. The effect of hatch distance on the grain direction in the side view was not significant.

The effect of the scanning strategies is shown in Figures 1.6 and 1.7. The tilting angle of the grains in the top view is consistent for the unidirectional scanning strategy, Figure 1.6-f, compared to the bidirectional scanning strategy, Figure 1.6-a. Furthermore, alternating the scanning vectors from a layer to layer by $90^{o}$ results in equiaxed microstructure leading to more isotropic mechanical properties. Scanning strategies also influence grain direction with respect to building direction, Figure 1.7. For non-alternating scanning strategies, grain direction is slightly tilted with the building direction. This tilting angle increases as the scanning speed increases. For alternating strategies, two grain directions exist in the building direction, each is parallel to the building direction in one view and tilted in the other view. Since the grain direction follows the melt pool, parts produced by LPBF are

anisotropic. Therefore, grain direction and part building orientation play a significant role on parts mechanical properties. Such behavior was observed in [16] where it was found that the yield strength, young's modulus, ductility, and ultimate strength change significantly with the building orientation for a porous structure of Ti-6Al-4V alloy.

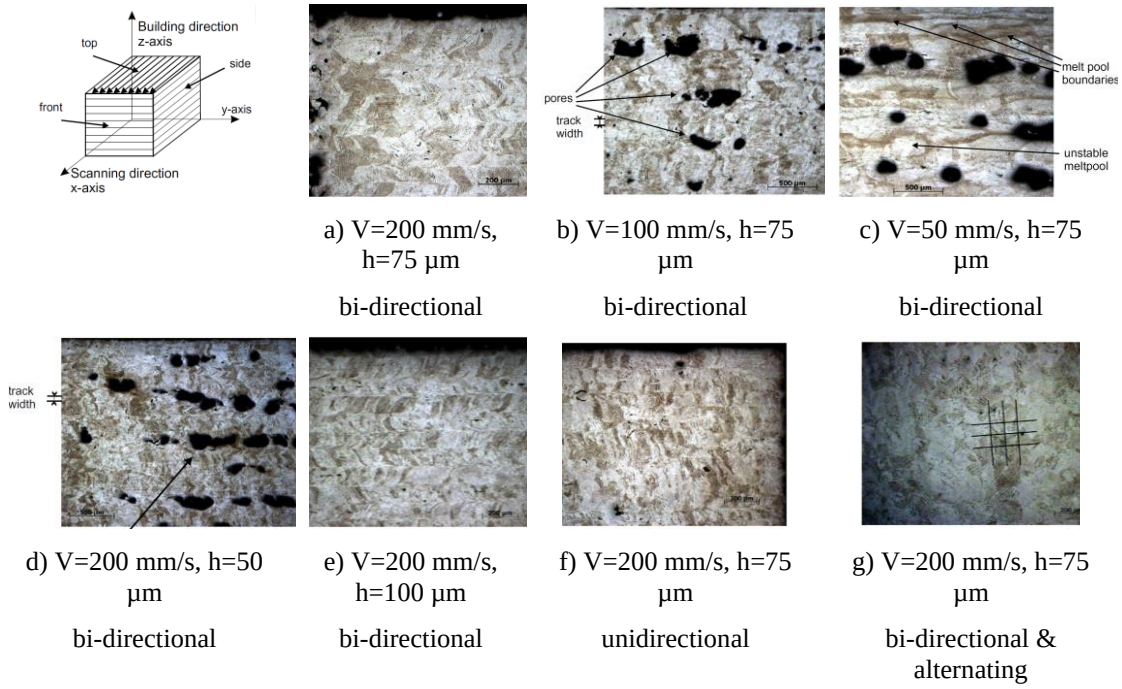


a) V=200 mm/s, h=75 µm bi-directional

b) V=100 mm/s, h=75 µm bi-directional

c) V=50 mm/s, h=75 µm bi-directional

d) V=200 mm/s, h=50 µm bi-directional

e) V=200 mm/s, h=100 µm bi-directional

f) V=200 mm/s, h=75 µm unidirectional

g) V=200 mm/s, h=75 µm bi-directional & alternating

**Figure 1. 6.** Top view of samples [10].

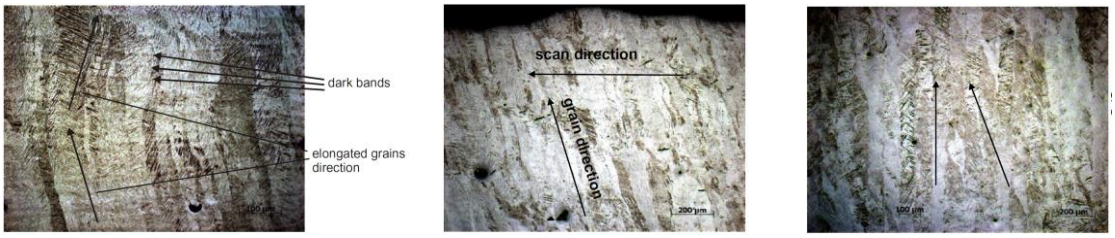


a) bi-directional

b) unidirectional

c) 90 alternating bi-directional

**Figure 1. 7.** Side view V=200 mm/s, and h=75 µm [10]

### 1.2.3. Mechanical Properties

As mentioned earlier, the microstructure for parts manufactured by LPBF is a very fine martensitic primary α phase, therefore, the Ti-6Al-4V parts manufactured by LPBF have low ductility and tend to be brittle [10, 17]. Compared to wrought Ti-6Al-4V that has 16% elongation [14], the maximum elongation for as-built Ti-6Al-4V parts was about 9% [7]. Furthermore, because of the high α fraction, parts produced by LPBF have higher yield and ultimate strength than wrought Ti-6Al-4V parts [7, 10, 20-21], and different elasticity modulus, Figure 1.8. Since the microstructure also depends on process parameters, the material ductility changes as the process parameters vary. It was observed that the ductility changes with the scanning speed in [7], and with part orientation in [16, 17]. In Figure 1.8, the high reduction in the material ductility and strength when the scanning speed is high (V=1500 mm/s) suggests that the effect of large lack-of-fusion porosity becomes dominant along with material brittleness. Tensile test showed that the fracture type at this case was brittle and initiated from the pore [7].

The fatigue performance was also investigated. The effect of parts building orientation on its life was investigated in [19, 20]. Per their findings, building orientation significantly affects the fatigue strength and part life. As mentioned earlier, the residual stresses and microstructure change as the part building orientation changes. Figure 1.10 shows the results from a AlSi12Mg parts fatigue experiments where the part fractured because of a large pore at the surface [20]. The S-N curves, Figure 1.9, for parts produced by different scanning speeds were studied in [7]. It is obvious that parts manufactured by LPBF at low scanning speed have a high fatigue strength than parts manufactured at high scanning

speeds. The main reason for this is that at low scanning speeds, pores size is smaller. This clearly shows how significant the scanning speed and resulting porosity are for the part life and fatigue strength.

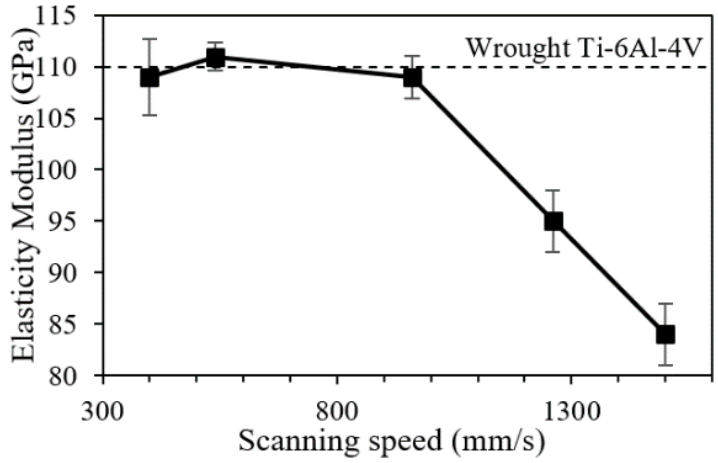


(a) Elasticity modulus

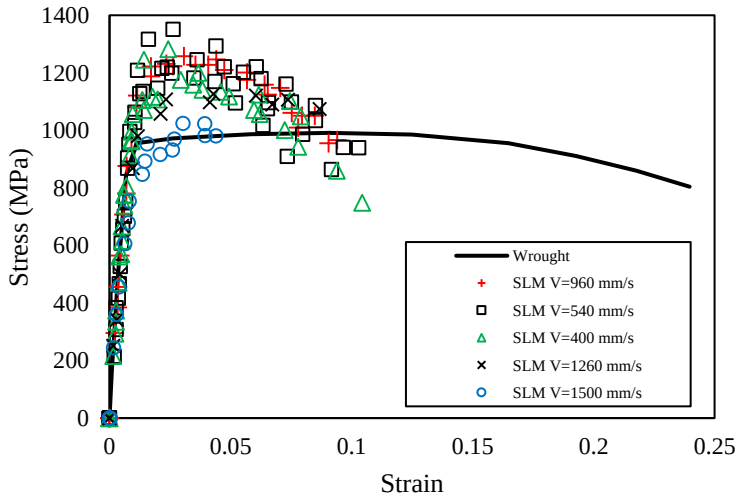


(b) Stress-strain curves

**Figure 1. 8.** Effect of scanning speed on the elasticity modulus and ultimate strength [10]

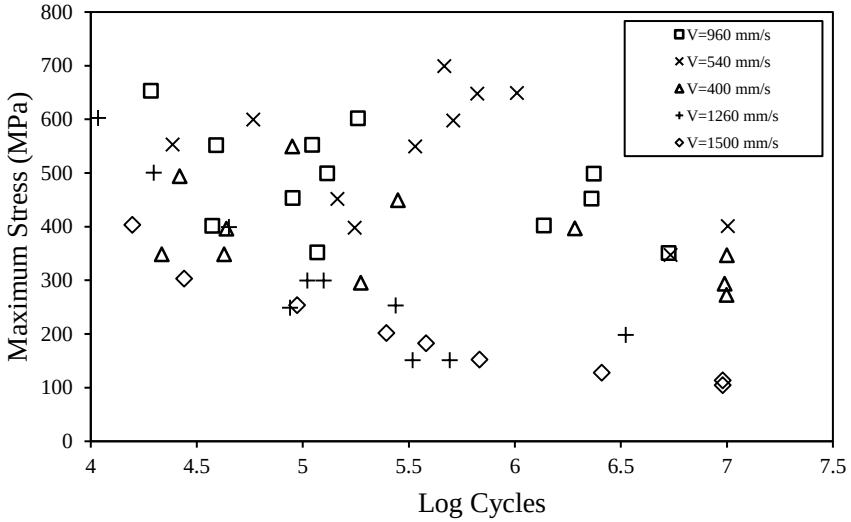


**Figure 1. 9.** Effect of scanning speed on fatigue strength [10]

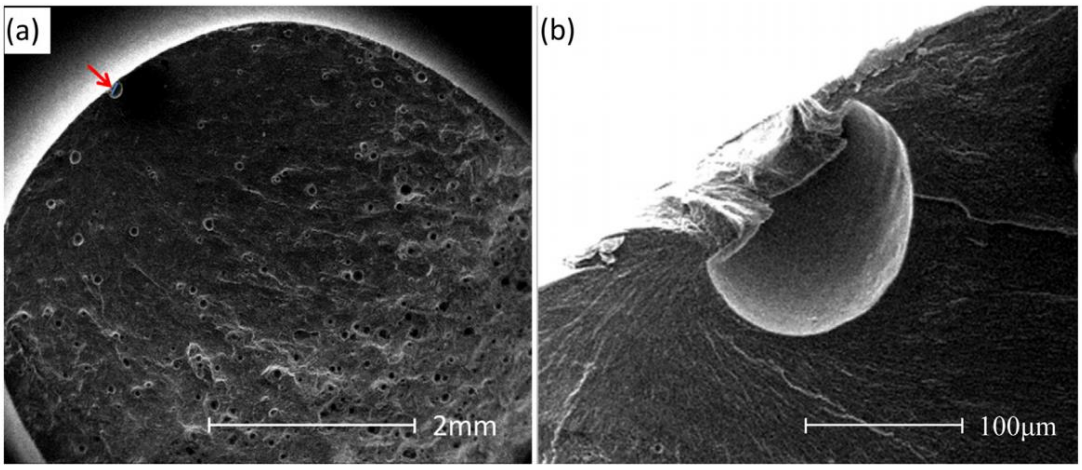


**Figure 1. 10.** Specimen fracture surface: (a) fracture surface and crack initiation point (arrow), and (b) crack initiation point [20]

### *1.3. Post processing*

Even though post processing steps are costly, they are important to improve the part quality in terms of porosity, residual stresses, and microstructure. Various post processing techniques presented in the literature are discussed in this section.

Machining can be used as a post processing step. Edwards [19] conducted fatigue experiments for as-built and machined specimens to quantify the effect of the as-built surface roughness. It was found that at the same applied stress and two different building orientations, machined specimens lasted longer than as-built parts, Figure 1.11. The rough surface in as-built parts plays a dominant role in crack initiation resistance. In addition, machining can also introduce compressive residual stresses that improve crack propagation resistance. Polishing also was found to improve the surface roughness, and the fatigue strength. Polished specimens were also found to have higher fatigue strength (endurance limit was improved from 210 MPa for as-built part, to 500 MPa for polished part) [21]. Machining and polishing methods are limited to simple geometries or external features, and they cannot improve porosity.

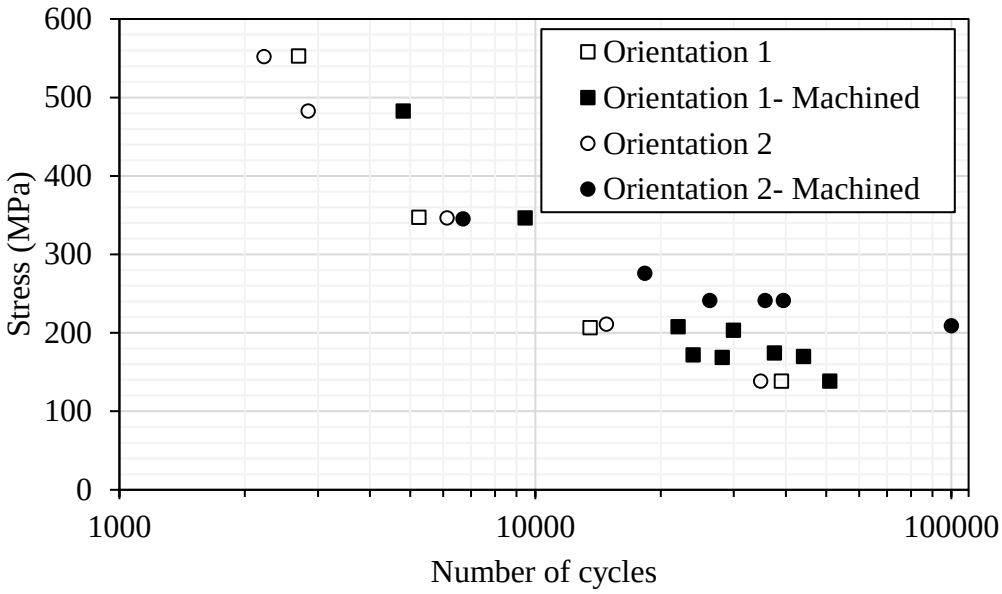


**Figure 1. 11.** S-N curved for as-built and machined specimens (Reproduced from [18])

Hot isostatic pressing (HIP) was found to be beneficial for parts produced by SLM. When parts are heated at high temperature (920$^{o}$ C) and pressure (1000 bar), pores size, residual stresses, and material ductility are improved. In Leuders' study [8], due to the microstructural fraction and size changes, Figure 1.12(c), the HIP was found to improve the material ductility (from 1.6% elongation for as-built part to 8.3% elongation for HIPed part). However, this improvement is associated with a slight reduction in the part ultimate and yield strengths ($\sigma_y$ reduced from 1008 MPa to 912 MPa). The ductility improvement led to longer life (up to 2 million cycles), compared to the as-built part which did not last for more than 27000 cycles. In addition, the pores size can be significantly reduced using HIP, Figure 1.13. The pores size could be reduced to undetectable range (less than 22 µm).

Heat treatment was also found to improve the part quality. The heat treatment can be done below or above the β transus temperature, which is 980$^{o}$ C [14]. Heat treating the as-built

parts at temperature of 800$^{o}$ C, which is below the transus temperature, for 2 hours significantly reduces the residual stresses (from about 235 MPa to -5 MPa) and improves the fatigue strength and life from 27000 cycles for the as-built part to 93000 cycles, without a significant effect on the microstructure and material strength, Figure 1.12 (b). Heat treating at 1050$^{o}$ C for 2 hours improves material ductility, fatigue strength, and part life (93000 cycles), associated with a reduction in the material strength. These changes are due to the microstructure evolution, increased α grains size, β formation during the heat treatment shown in Figure 1.12 (d).

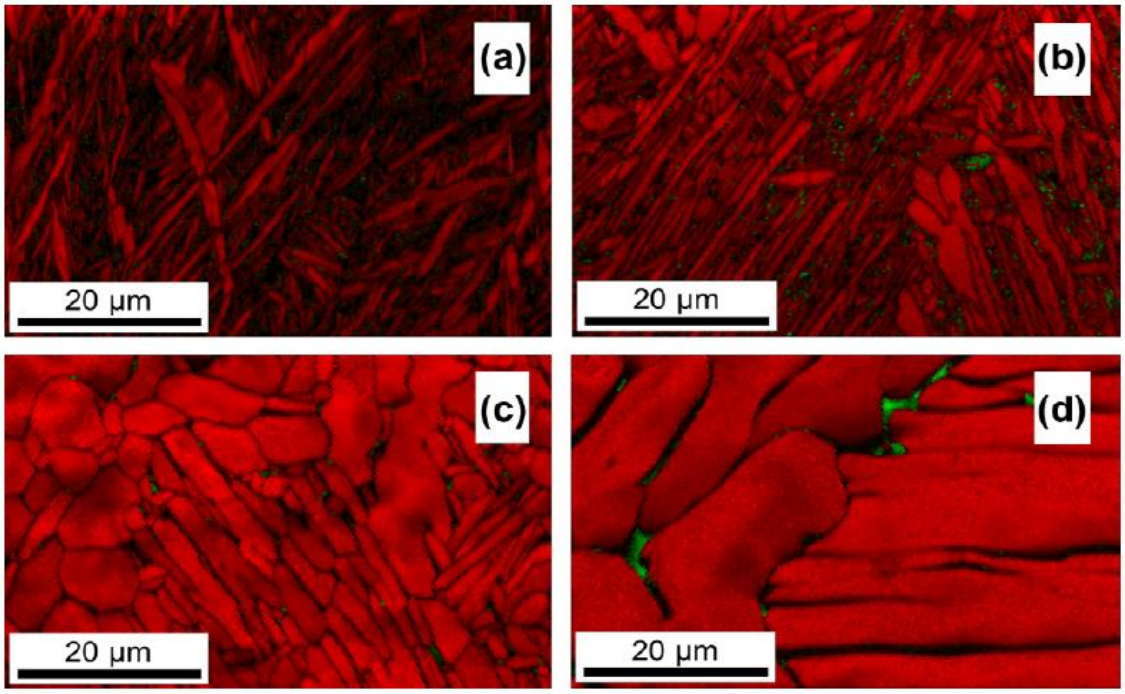


**Figure 1. 12.** Microstructure of: (a) as built, (b) Heat treated at 800 C, (c) HIPed, and (d) Heat treated at 1050 C. [8]

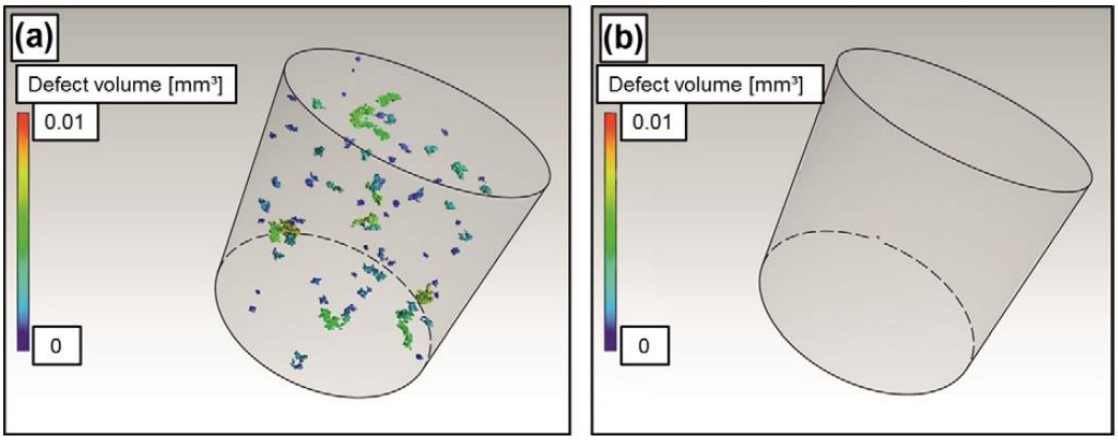


**Figure 1. 13.** CT images for porosity for (a) as-built part, and (b) HIPed part. [8]

# 2. Thermal Modeling of LPBF Process

## *2.1. Literature Review*

Predicating the thermal history parts experience during the build process is crucial; such predictions can help delivering critical insights to analysts and operators to avoid the high costs associated with failed or distorted parts during the building process or after becoming in service. The LPBF process parameters can be changed to avoid these failures, especially for parts with complex features or thin walls. Although, analytical methods were developed to predict temperature distributions, they are always associated with simplifications such temperature-independent material properties and may not be able to capture the complexity of the process physics. Numerical methods, where the domain can be discretized into grid, such as finite difference, finite volume, or finite element provide helpful tools to predict thermal history considering material properties temperature dependency and scanning strategies. With complete understanding of the part thermal history, decision could be made to improve the parts porosity, residual stresses, and microstructure.

Thermal modeling of the LPBF process using finite element modeling (FEM) is challenging for many reasons. Firstly, the heat source model should represent a laser beam with a diameter ranges between 50 μm to 250 μm, therefore, a fine mesh is needed to accurately represent this Gaussian profile of the heat source, which makes the problem computationally expensive. Secondly, the phase changes associated with that problem adds high nonlinearity to the problem, which encounter convergence difficulties and require using iterative procedure.

Single track simulations that consider powder particle distribution were helpful to understand physics and defects that take place during the process and validate the computational model. Khairallah et al. [22] investigated the fluid flow and elastic-plastic material response during LPBF process using mesoscopic simulation model. In a later study, Khairallah et al. [23] investigated the pore formation mechanisms. In the two studies, the authors developed a finite element model using Arbitrary Lagrangian Eulerian (ALE) approach considering a stainless-steel powder bed with particle size measured experimentally. Mindt et al. [24] also developed a micromodel which considers the powder particle, and predicts porosity, surface roughness, and melt pool characteristics. Although models addressed by this approach help in understanding the thermal cycles, material consolidation quality, and identifying process window for each material, they are computationally expensive since each powder particle is represented by set of elements. Thus, utilizing such approach for multiple scanning vectors and part-scale levels is computationally infeasible.

Macroscale models, where the element cannot represent the powder particles distribution, were also used to determine the melt pool characteristics and to predict the influence of process parameters and scanning strategies on the temperature distribution and induced residual stresses. Though several research studies where well-developed finite element methods were used to study and investigate the LPBF process, part-scale simulations were not well addressed. Some of these studies were simplified so that they limited to: (1) single layer analysis [25]–[29],(2) coarse mesh [26], (3) bulk layer assumption (scaling up the build layer thickness)[30], and (4) even simplifying the heat source model to Gaussian line

heat source [31] or uniform heat source over the entire layer. These simplifications could make the problems computationally feasible, however, they are always associated by a sacrifice in accuracy. For example, using bulk layer or simplifying the heat source model result in inaccurate temperature history for the part. In addition, using coarse mesh results in large discretization error, which may make the results unreliable. Therefore, there is a challenge to keep the problem size feasible without a significant loss in accuracy.

The element birth and death approach was found to be useful to simulate the addition of new layers [32]. It is currently adopted in the AM commercial packages simulations (ANSYS Additive, Simufact Additive, etc.). This technique works by dividing the part geometry into layers, generating the mesh for all layers once, and mathematically killing or deactivating the elements that are above the build layer by multiplying its thermal conductivity by low number ($10^{-6}$). Once the current build layer simulation is complete, the following layer elements are activated, and simulation is solved for the new layer. The disadvantages of this approach are: (1) though the elements are deactivated, they still exist in the stiffness matrix and the problem size is similar for any build layer, and (2) the elements size is restricted by the layer thickness. Thus, the computational time using this approach is still expensive. Although the commercial software simplify the problem by assuming a bulk layer or mechanical equivalent layer and uniform heat source that is applied once throughout the build layer, the element birth and death approach is still expensive for large parts.

Another approach based on super-position was found to be helpful reducing the computational time from 33 years to 3 months for 5 mm x 5 mm x 2 mm part [33].

However, the approach was helpful only when linear heat equation is considered, and the thermal conductivity and specific heat are assumed temperature independent.

Adaptive remeshing provides a solution to overcome the high computational time and resources needed to simulate LPBF problems. The mesh is continuously changing during the solution so that fine mesh always exists where the temperature gradient is high, and coarse mesh elsewhere. Pal et al. [25] and Patil et al. [34] developed adaptive remeshing framework for a single layer where there is a moving refined mesh area that shares its boundary nodes with the part coarse mesh, Figure 2.1 (a). A similar technique was adopted to simulate part-scale build process [35], Figure 2.2. A layer-wise adaptive remeshing approach is currently developed in the commercial AM software NetFabb for small scale parts, Figure 2.1 (b). Although these approaches were helpful improving model fidelity with reduced computational time, it is limited to hexahedron elements and uniform mesh. In addition, meshing using hexahedron elements can be very time consuming for complex parts that are easier to mesh with tetrahedron mesh. Thus, remeshing with hexahedral elements is more suitable for very simple parts that do not include curvatures since remeshing with this element shape considering keeping all part curvatures for complex parts might be very expensive. Another problem is that the current commercial packages do not have the capability of having customized remeshing techniques, therefore, the authors had to develop their own thermal solvers which might not be as accurate as the existing and well-developed commercial solvers.

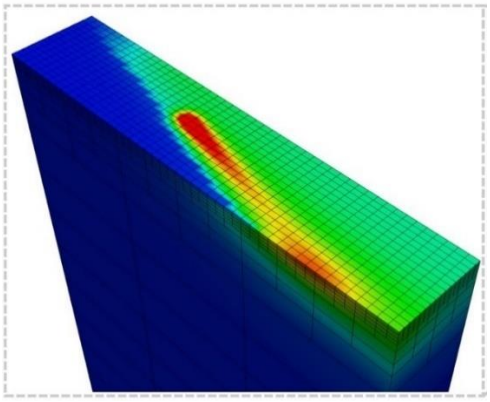

Pan Computing (Now NetFabb) [36]

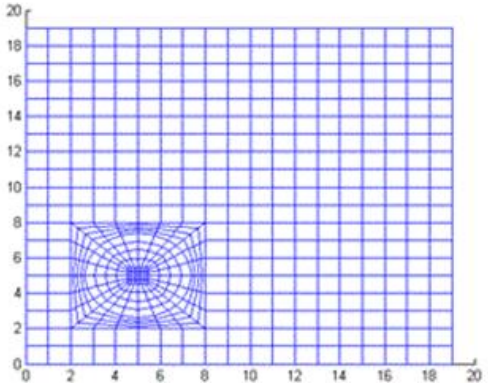


3DSIM mesh Configuration (Now ANSYS Additive) [34]

**Figure 2.1:** LPBF thermal simulations with adaptive remeshing (Available in commercial packages)

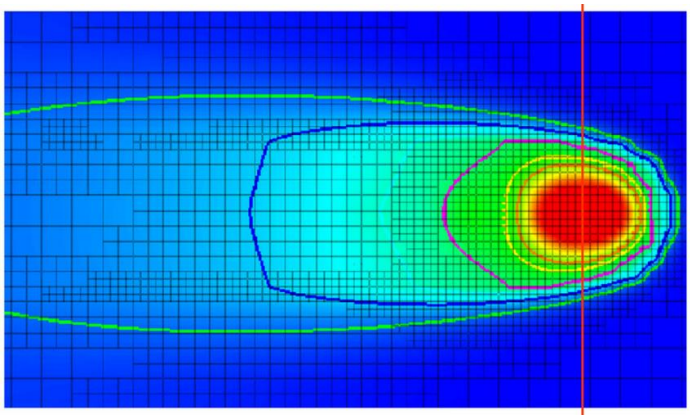

**Figure 2.2:** Mesh configuration for simulation with adaptive remeshing [35]

## *2.2. Research Motivation*

As previously mentioned, thermal modeling for part-scale using the traditional method is computationally infeasible unless there are assumptions by which the problem could be

simplified. The reason is that the laser spot size is too small compared to the part, and having fine mesh everywhere is computationally expensive.

The motivation of this dissertation is to reduce the computational time for thermal modeling of LPBF process and to make these simulations feasible on modest computational resources. This motivation was driven by the need to run many simulations for the uncertainty analysis. Therefore, an adaptive remeshing framework was developed with the aim of reducing the size of the stiffness matrix. The previously aforementioned published adaptive remeshing techniques rely on the use of hexahedron mesh or voxels, which are not able to capture the features that complex parts have. Unlike previously published studies, this work is the first study where an adaptive remeshing framework utilizing a commercial solver is developed. Every single step of the framework was computationally optimized, and minimum computational time was achieved. In addition, the use of tetrahedral mesh was introduced for the first time, which is more advantageous representing complex parts with high element growth rate. Thus, less elements and nodes are needed.

## *2.3. Model Description*

### 2.3.1. The Adaptive Remeshing Framework

In this dissertation, adaptive remeshing is applied in two ways: layer-wise and scan-wise adaptive remeshing. The layer-wise adaptive remeshing is more efficient for smaller parts as a new mesh is generated for each newly added layer. When the part is large, the number of steps and nodes become large, therefore, there is a need to utilize a scan-wise adaptive

remeshing technique. In both approaches, since there is a mesh change, a framework where results are transferred from the old mesh to the new mesh is developed. Although this remapping framework may add to the total computational time, the reduction is the total computational time is much more significant.

*2.3.1.1. Single Track with Adaptive Remeshing*

The purpose of the single-track model is to validate the numerical model and to understand how the process parameters and their variation affect the melt pool size. This model captures the powder layer properties with 10µm element size, Figure 2.3. Thus, adaptive remeshing for this model is essential to save computational time. For minimal computational time, all the mesh configurations and temperature remapping equations for this model were generated in advance so that no remeshing or temperature remapping will take place during the solution, Figure 2.4. The run time for each single case using this model is approximately 15 minutes.

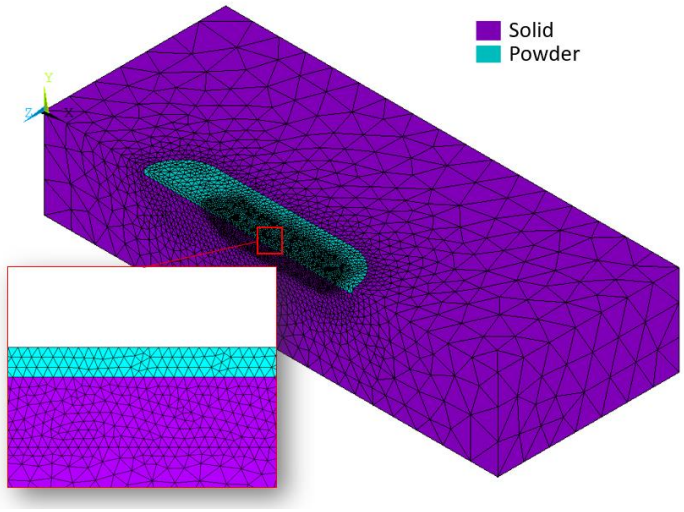

**Figure 2.3:** Mesh Configuration for Single Track Simulation

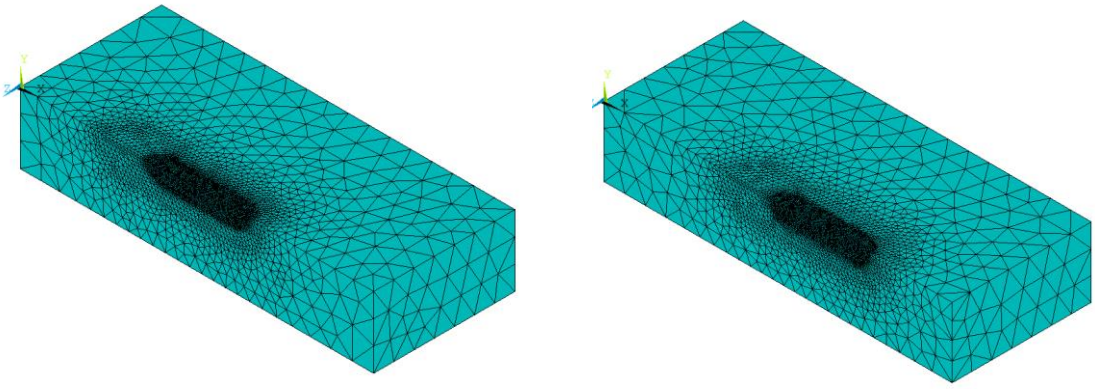

Mesh 4 Mesh 5

**Figure 2.4:** Mesh configuration for two consecutive simulation tasks

*2.3.1.2. Layer-wise Adaptive Remeshing*

The layer-wise adaptive remeshing is used for the layer-by-layer build, where the mesh is always kept fine at the powder layer and high temperature gradient region, and coarse elsewhere, Figures 2.5. A typical element size at the powder layer using this approach is set to the layer thickness, e.g. 30 μm. This adaptive remeshing approach is suitable for small parts and when lack-of-fusion porosity predictions is needed. Considering this approach, accounting for the powder-to-solid transition and assigning powder material properties to layer elements is feasible, Figure 2.6. The framework for the analysis with layerwise adaptive remeshing is simple. After solving the thermal problem for the first layer, a new mesh is generated for the second layer and the temperature solution is mapped from the old mesh to the new mesh. This process continuous until all layers are complete. During the solving, the temperature history of elements is checked, and if all the element's nodes exceed the material melting temperature, the material assignment of the element is

changed to solid material, Figure 2.7. After the completion of solving each layer, a new mesh with the new powder layer is generated. By the end of each layer analysis, the remaining powder elements are considered lack-of-fusion pores since the powder particles melting is incomplete. The drawback of this approach is that partial melting of powder particles is ignored and predicted lack-of-fusion porosity will always be higher than experimentally measured values.

Figure 2.8 shows the significant reduction in the number of nodes when layerwise adaptive remeshing is used compared to the case without adaptive remeshing. The 90% reduction in the number of nodes leads to a much smaller stiffness matrix that is much faster to solve. In addition, the number of nodes when this layer adaptive remeshing technique with tetrahedral mesh is used is much less than required when using the voxels-based approach, Figure 2.9. For complex geometries that include curvatures and thin walls, having voxels that keep part's complex feature is computationally.

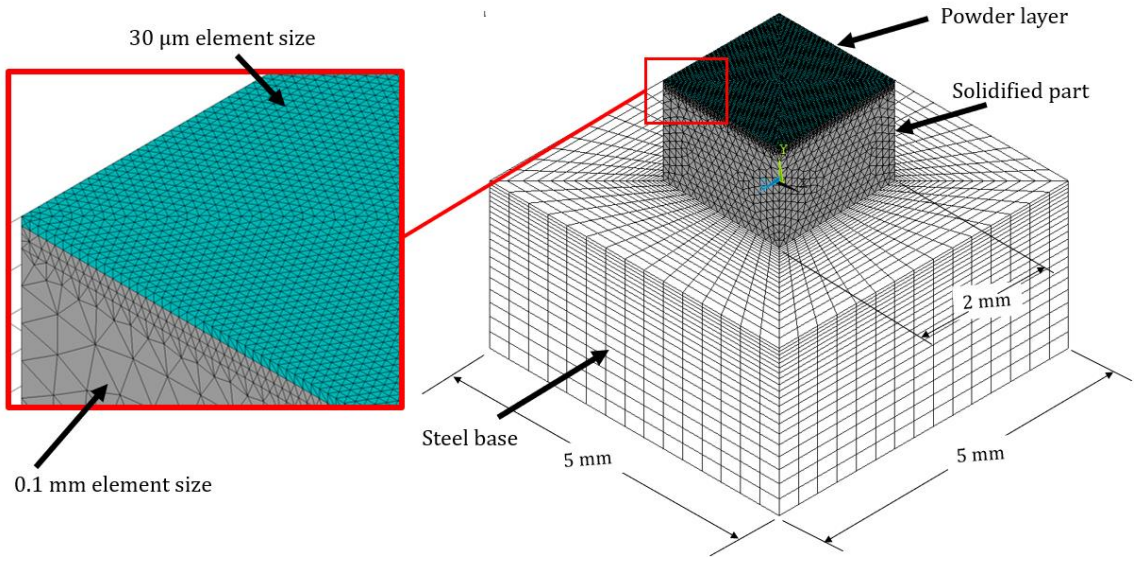


**Figure 2.5:** Build part including powder layer on a base plate

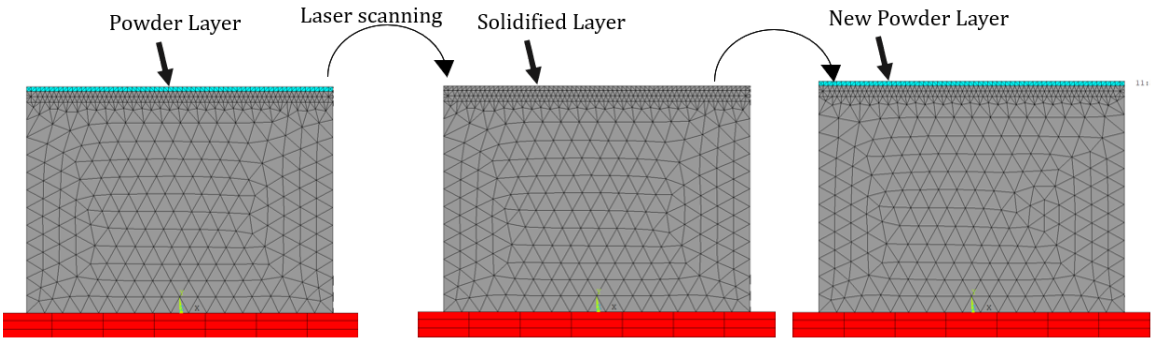


**Figure 2.6:** Layer-wise adaptive remeshing configuration for: (a) Layer 49 at the beginning, (b) Layer 49 after entire layer is scanned, and (c) Layer 50, after addition of one powder layer

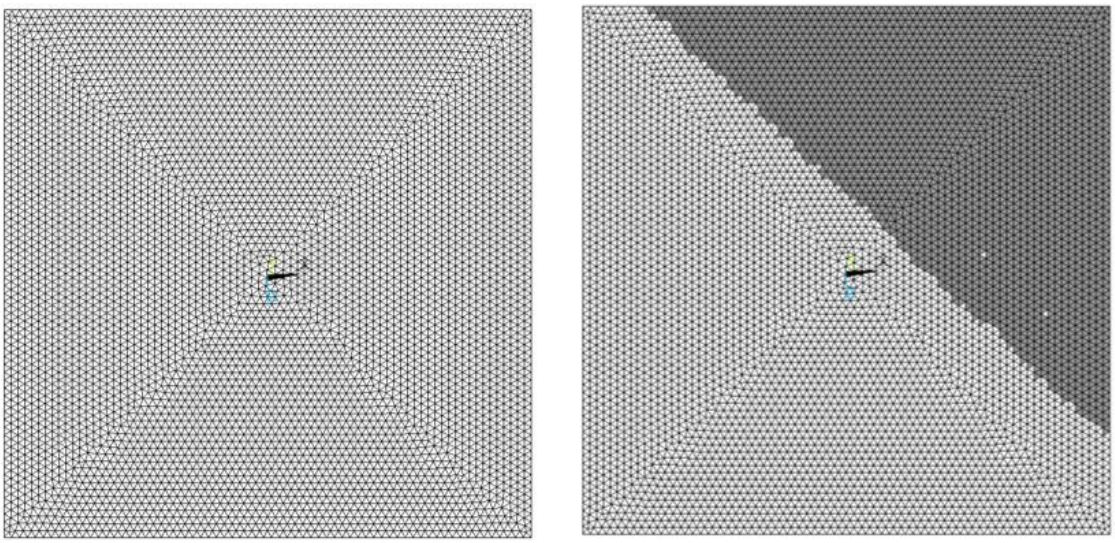

**Figure 2.7:** Element material change once the element nodes temperature exceeds the melting temperature

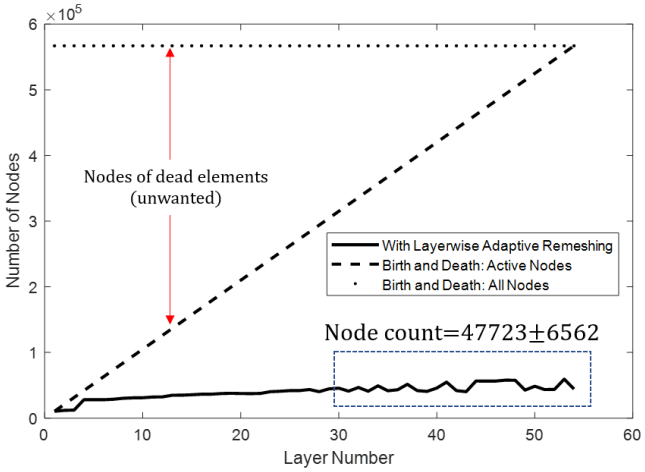


**Figure 2.8:** Comparison between the stiffness matrix size for model includes remeshing, and birth and death approach

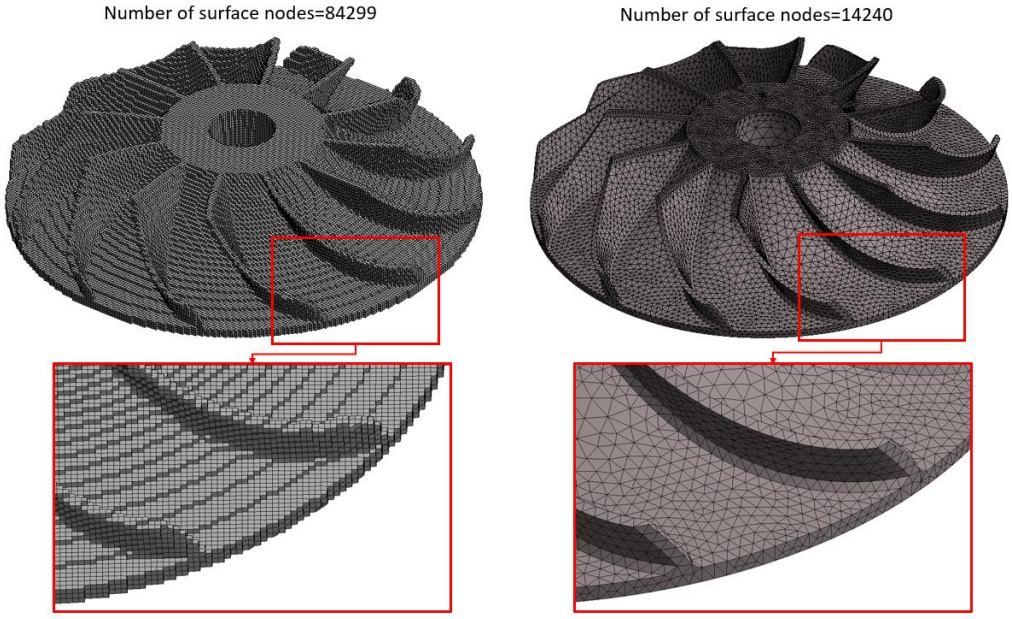


**Figure 2.9:** Mesh configuration for complex geometry considering both cubic-shape and tetrahedral elements with layer element size 1 mm.

*2.3.1.3. Scan-wise Adaptive Remeshing*

The second remeshing approach was based on the continuous mesh refinement and coarsening based on the location of laser beam. This approach relies on the remeshing tool that ANSYS software is using for the Nonlinear Adaptivity (NLAD) features. The NLAD framework works for high deformation problems where elements are distorted, they are sent to the remeshing tool for remeshing or refining. This remeshing task is essential to have a convergent analysis. Similarly, in the thermal problem, the coarse elements, where high temperature gradient is expected, are sent to the remeshing tool for refinement. This refinement is essential to capture the high temperature gradient region and to accurately represent the heat source, Figure 2.10. With this approach, the refinement is mainly controlled by the refinement length, Figure 2.11. A long refinement length results in large number of nodes, but less remeshing and remapping tasks. A short refinement length results in lower number of nodes, but more remeshing and remapping tasks. In addition, there is a fixed time associated with launching the solver and reading the input files. Therefore, the optimal remeshing length cannot be easily determined, and it may vary from a case to another. Compared to the layer-wise remeshing approach, this approach requires more remeshing and remapping tasks, but more suitable for large parts. However, a drawback of this approach is that powder-to-solid transition cannot be considered since adding such constraint to the remeshing problem will make it computationally expensive. When using this approach, it is always essential to make sure that the element edge length is small enough so that multiple nodes can represent the heat source. A histogram of the refined elements' edge size is shown in Figure 2.12. The framework for the thermal analysis with scan wise adaptive remeshing is shown in Figure 2.13.

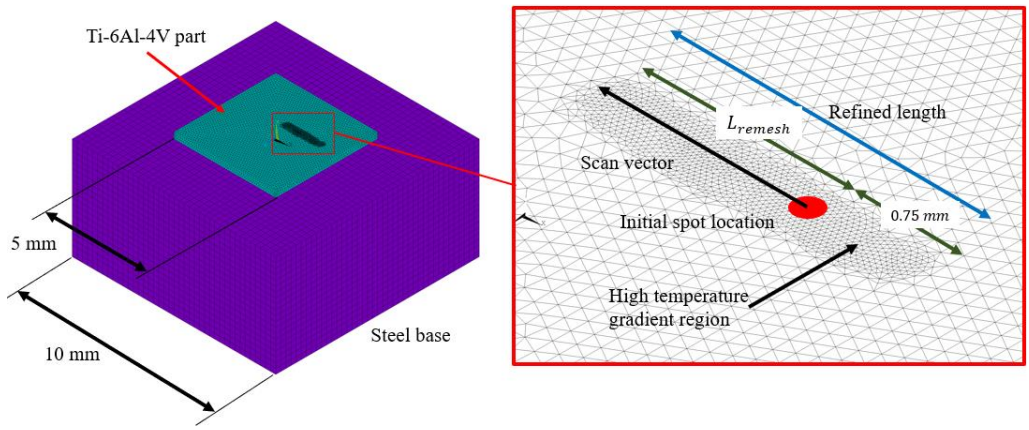


**Figure 2.10:** Mesh configuration for the scan-wise adaptive remeshing approach

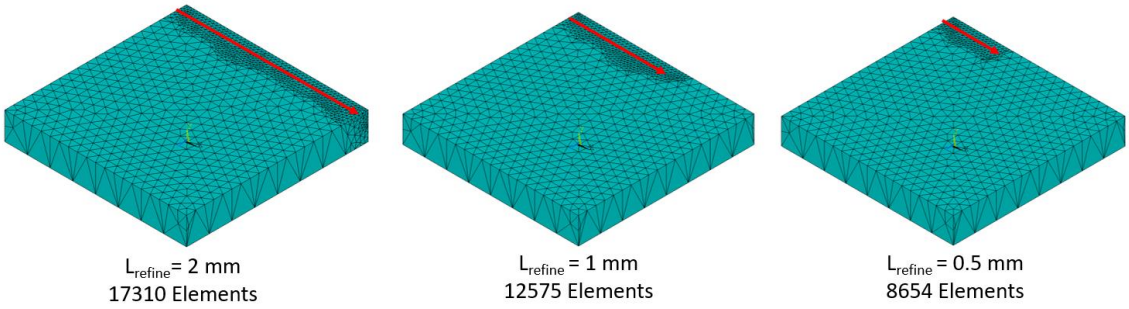


**Figure 2.11:** Effect of the refinement length on mesh density

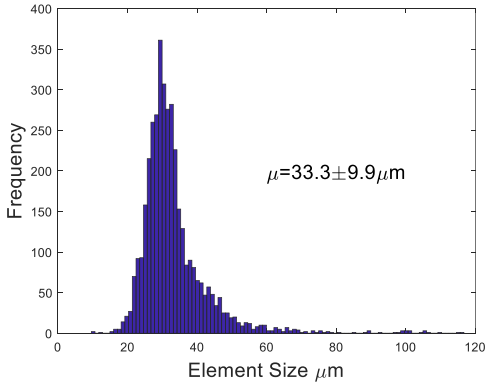


**Figure 2. 12.** Element size distribution at the refined area

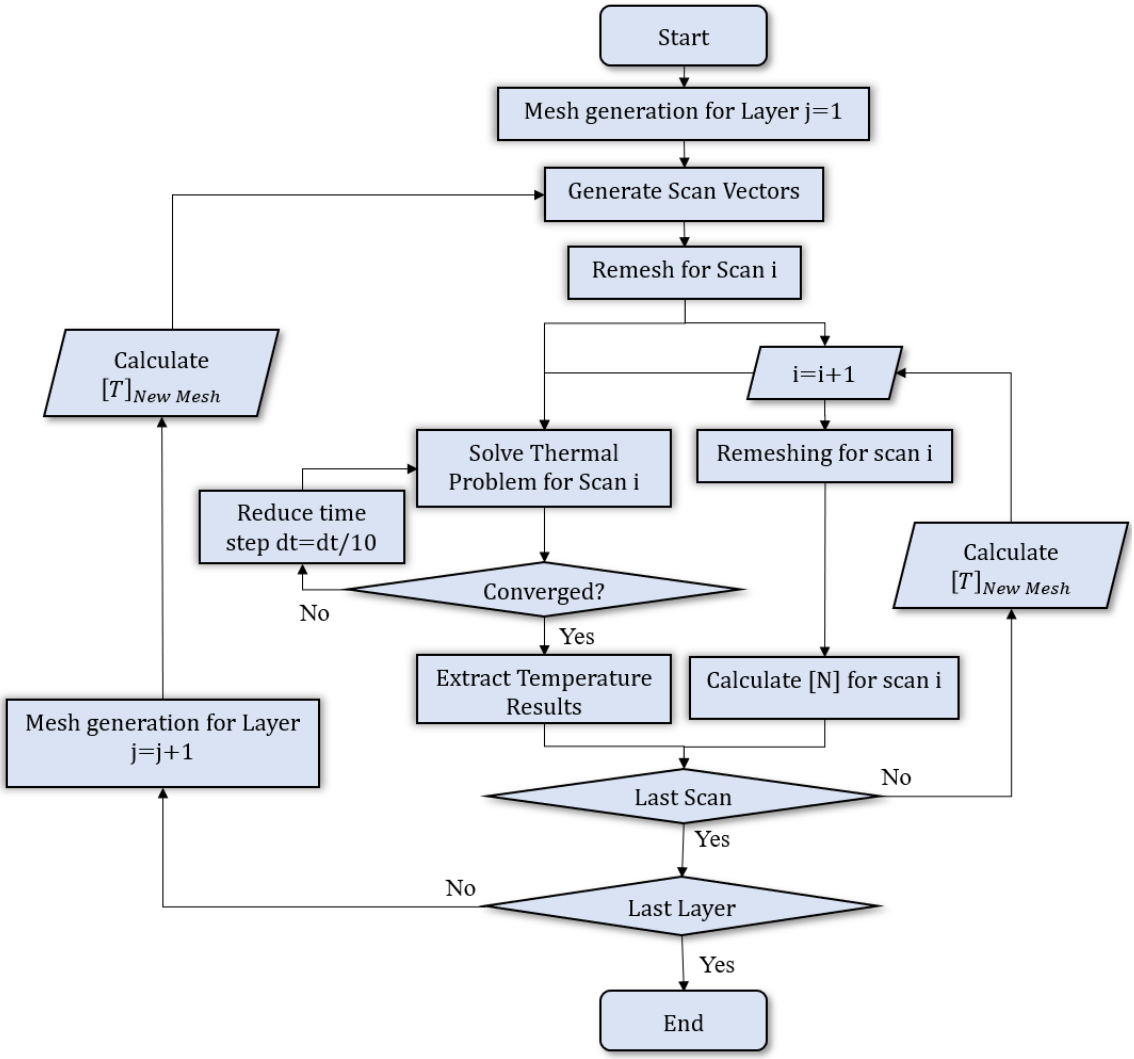


**Figure 2.13:** Framework for the Thermal simulation with scan-wise adaptive remeshing

### 2.3.2. Temperature Remapping

When using adaptive remeshing, remapping procedure must be used to transfer the temperature results from the previous mesh before remeshing to the newly generated mesh. In addition, the remapping framework enables tracking the thermal history at any location

of interest even if no nodes exist at that location. In the current work, two remapping algorithms were considered:

*2.3.2.1. Distance-based remapping*

With this approach, the new mesh nodes' temperature is calculated from the old mesh nodes based on the nearest K nodes. In addition, a simplification can be made such that if the old node is too close, the temperature results are just transferred. Therefore, the temperature of a node *i* in the new mesh can be calculated as

$$T_i(t) = \begin{cases} T_j & d_{ij} \leq 2.5\ \mu m \\ \dfrac{\sum_{j \in N} \frac{T_j(t)}{d_{ij}}}{\sum_{k \in N} \frac{1}{d_{ik}}} & d_{ij} > 2.5\ \mu m \end{cases} \qquad \text{Eq 2. 1}$$

Where $T_i$ is the temperature of the new node *i*, $T_j$ is the temperature of the old node *j*, $d_{ij}$ is the distance between the new node *i* and old node *j*, and *N* is the set of nearest *K* nodes. This approach is too fast and easily to implement, however, it is not suitable when coarse elements are also changed since it will be associated by a significant loss of data.

*2.3.2.2. Shape function-based remapping*

The shape function is the function by which the solution at any point inside the element can be interpolated from discrete values obtained at the element nodes. The shape function for the 4-nodes (SOLID70) and 10-nodes (SOLID87) tetrahedral elements, Figure 2.14, are shown in Equations 2.2 and 2.3, respectively.

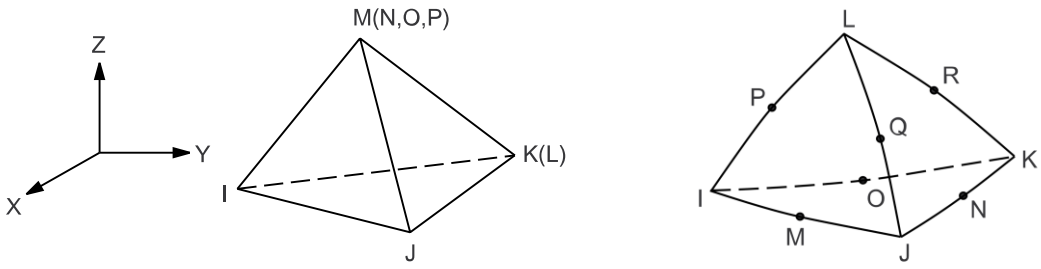


SOLID70 SOLID87

**Figure 2.14:** 3D Thermal Elements used for the thermal simulation

$$T = N_1 T_I + N_2 T_J + N_3 T_K + N_4 T_M \quad \text{Eq 2. 2}$$

$$T = N_1(2N_1 - 1)T_I + N_2(2N_2 - 1)T_J + N_3(2N_3 - 1)T_K + N_4(2N_4 - 1)T_L + 4N_1N_2T_M + 4N_2N_3T_N + 4N_1N_3T_O + 4N_1N_4T_P + 4N_2N_4T_Q + 4N_3N_4T_R \quad \text{Eq 2. 3}$$

Where $N_i$ is the shape function value for node i, and $T_i$ is its temperatures. The shape function can be calculated as:

$$N_i = \frac{\alpha_i + \beta_i x + \gamma_i y + \delta_i z}{6V} \quad \text{Eq 2. 4}$$

Where V is the element volume and can be obtained as:

$$V = \frac{1}{6}\begin{vmatrix} 1 & x_1 & y_1 & z_1 \\ 1 & x_2 & y_2 & z_2 \\ 1 & x_3 & y_3 & z_3 \\ 1 & x_4 & y_4 & z_4 \end{vmatrix} \quad \text{Eq 2. 5}$$

And the coefficients $\alpha_i$, $\beta_i$, $\gamma_i$, and $\delta_i$ are given by

$$\alpha_1 = \begin{vmatrix} x_2 & y_2 & z_2 \\ x_3 & y_3 & z_3 \\ x_4 & y_4 & z_4 \end{vmatrix}, \beta_1 = -\begin{vmatrix} 1 & y_2 & z_2 \\ 1 & y_3 & z_3 \\ 1 & y_4 & z_4 \end{vmatrix}, \gamma_1 = \begin{vmatrix} 1 & x_2 & z_2 \\ 1 & x_3 & z_3 \\ 1 & x_4 & z_4 \end{vmatrix}, \delta_1 = -\begin{vmatrix} 1 & x_2 & y_2 \\ 1 & x_3 & y_3 \\ 1 & x_4 & y_4 \end{vmatrix} \quad \text{Eq 2. 6}$$

$$\alpha_2 = -\begin{vmatrix} x_1 & y_1 & z_1 \\ x_3 & y_3 & z_3 \\ x_4 & y_4 & z_4 \end{vmatrix}, \beta_2 = \begin{vmatrix} 1 & y_1 & z_1 \\ 1 & y_3 & z_3 \\ 1 & y_4 & z_4 \end{vmatrix}, \gamma_2 = -\begin{vmatrix} 1 & x_1 & z_1 \\ 1 & x_3 & z_3 \\ 1 & x_4 & z_4 \end{vmatrix}, \delta_2 = \begin{vmatrix} 1 & x_1 & y_1 \\ 1 & x_3 & y_3 \\ 1 & x_4 & y_4 \end{vmatrix} \quad \text{Eq 2. 7}$$

$$\alpha_3 = \begin{vmatrix} x_1 & y_1 & z_1 \\ x_2 & y_2 & z_2 \\ x_4 & y_4 & z_4 \end{vmatrix}, \beta_3 = -\begin{vmatrix} 1 & y_1 & z_1 \\ 1 & y_2 & z_2 \\ 1 & y_4 & z_4 \end{vmatrix}, \gamma_3 = \begin{vmatrix} 1 & x_1 & z_1 \\ 1 & x_2 & z_2 \\ 1 & x_4 & z_4 \end{vmatrix}, \delta_3 = -\begin{vmatrix} 1 & x_1 & y_1 \\ 1 & x_2 & y_2 \\ 1 & x_4 & y_4 \end{vmatrix}$$

Eq 2. 8

$$\alpha_4 = -\begin{vmatrix} x_1 & y_1 & z_1 \\ x_2 & y_2 & z_2 \\ x_3 & y_3 & z_3 \end{vmatrix}, \beta_4 = \begin{vmatrix} 1 & y_1 & z_1 \\ 1 & y_2 & z_2 \\ 1 & y_3 & z_3 \end{vmatrix}, \gamma_4 = -\begin{vmatrix} 1 & x_1 & z_1 \\ 1 & x_2 & z_2 \\ 1 & x_3 & z_3 \end{vmatrix}, \delta_4 = \begin{vmatrix} 1 & x_1 & y_1 \\ 1 & x_2 & y_2 \\ 1 & x_3 & y_3 \end{vmatrix}$$

Eq 2. 9

In order to use this approach, it is important to know in which old element the new node exists. So, firstly, a search algorithm where all nodes from the new mesh are assigned to elements from the old mesh. A node is assigned to an element only if it falls within that element domain such that:

$$\sum_{n=1}^{nF} I_{in} = \begin{cases} 4 & if\ nF = 4\ (SOLID70) \\ 16 & if\ nF = 10\ \ (SOLID87) \end{cases} \qquad \text{Eq 2. 10}$$

where *nF* is the number of element's faces, and $I_{in}$ is an indicator function that is equal 1 if the node is in appropriate location from the element face. It can be obtained as:

$$I_{in} = \begin{cases} 1 & [A_n][X_i] \leq 1 \\ 0 & [A_n][X_i] > 1 \end{cases} \qquad \text{Eq 2. 11}$$

$$[A_n] = [a_n \quad b_n \quad c_n] \qquad \text{Eq 2. 12}$$

$$[X_i] = \begin{bmatrix} x_i \\ y_i \\ z_i \end{bmatrix} \qquad \text{Eq 2.13}$$

$a_n$, $b_n$, $c_n$ are obtained from the element's face plane equation and represent the coefficients of x, y, and z of the plane equation, $[X_i]$ represent the new node locations. After the old element is determined, the new node temperature can be calculated as previously shown in Equations 2.1 and 2.2 depending on the element type. This approach is more accurate than the distance-based remapping approach. However, having curved surfaces, it might be possible that a new node cannot be located in any old element. The

temperature for these specific nodes can be calculated using the distance-based approach. A result from the shape-function based remapping approach is shown in Figure 2.15.

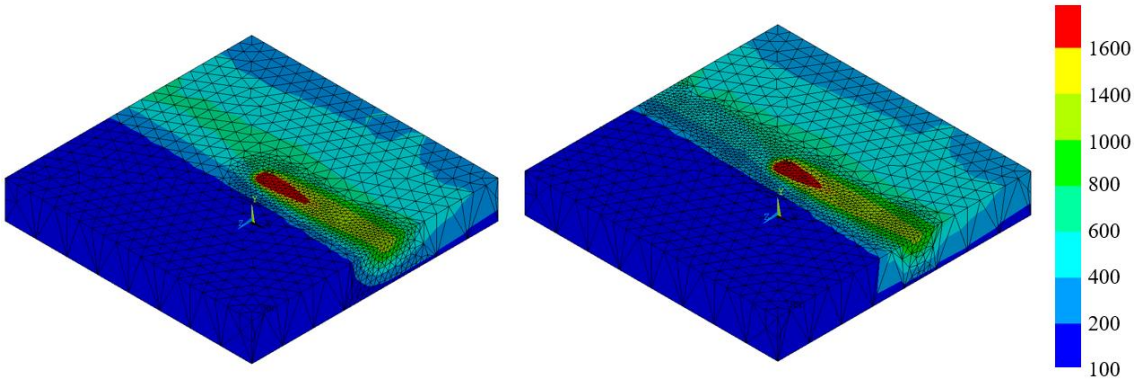


**Figure 2.15:** Temperature distribution before and after remeshing

*2.3.2.3. Remapping Time optimization*

The time spend in remapping constitutes a large portion of the total computational time during modeling this problem with adaptive remeshing. In general, the idea of remeshing is used to improve the quality of distorted elements during the solution in large deformation models. In this case, remeshing and improving the mesh quality is a must for convergent analysis and it does not take place before mesh is distorted. However, for the thermal problem, there is no mesh distortion during solution and all remeshing configurations, which are controlled by the laser beam movement, are known in advance. In other words, for the thermal problem, we can generate all the mesh configurations before knowing any thermal solution. Similarly, remapping can be done even if the thermal solution is unknown, by just finding the coefficients of $T_i$ in equations 2.1 and 2.2. This approach was utilized and was found significantly reducing the computational time. For further significant reduction in the computational time, the part is divided into smaller subdomains

and remapping was performed for each subdomain individually, Figure 2.16. With running parallel remapping tasks, over 90% of the remapping time could be reduced compared to a single task for the entire part, Figure 2.17.

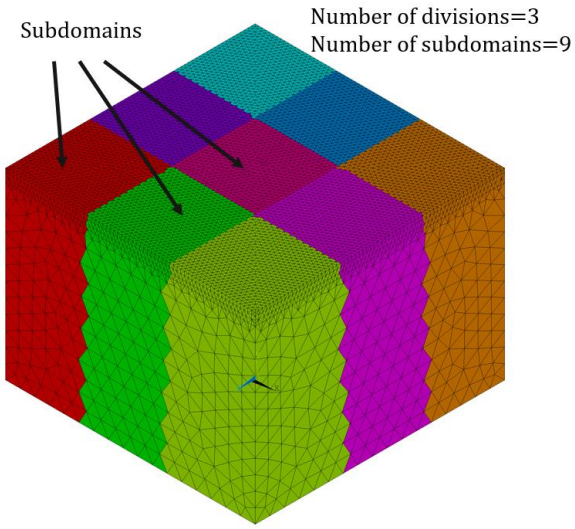


**Figure 2.16:** Schematic drawing showing the domain division into 9 subdomains (Number of divisions=3)

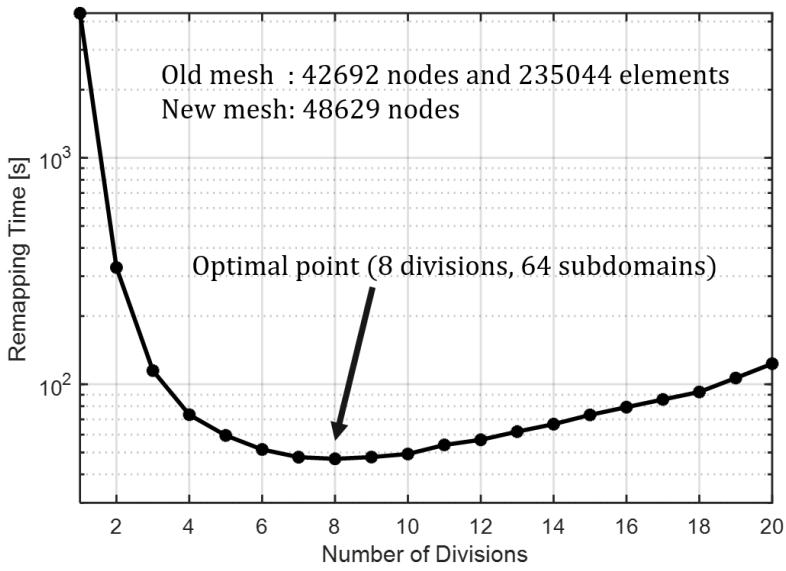


**Figure 2.17:** Effect of remapping number of divisions on the remapping time.

### 2.3.3. Boundary Conditions

Modeling the heat source is crucial for accurate melt pool size predictions. The Gaussian heat source model, shown in equation 2.14, was widely used in LPBF numerical models [37]. The heat flux as a function of time for any node *i* with coordinates ($x_i$ ,$y_i$) was simplified to be calculated as:

$$Q_i(t) = \begin{cases} \frac{2aP}{\pi r_{spot}^2} e^{-2\left(\frac{r_i(t)}{r_{spot}}\right)^2} & if\ r_i(t) < r_{spot} \\ 0 & otherwise \end{cases} \quad \text{Eq 2. 14}$$

$$r_i(t) = \sqrt{(x_i - V_x t)^2 + \left(y_i - V_y t\right)^2} \quad \text{Eq 2. 15}$$

where $r_i(t)$ is the Euclidean distance between node *i* and laser beam center at time *t*, *a* is absorptivity, *P* is the laser power, $r_{spot}$ is the laser spot radius, and $V_x$ and $V_y$ are the scanning speed components in x and y directions. With this heat source model, it is assumed that only nodes on the surface are exposed to the laser beam. This assumption may not well represent the real case due to the variation in the powder particles size and the laser beam scatter between the powder particles [38]. In addition, as will be discussed later, the model includes some uncertain parameters like the absorptivity, and the laser spot diameter. Another model based on Gaussian heat source considering the laser penetration depth, Eq. 2.16, was used for EBM and LPBF simulations in [39].

$$Q_i(t) = \begin{cases} \frac{6\sqrt{3}aP}{r_{spot}^2\, c\, \pi\sqrt{\pi}} e^{-3\left(\frac{(x_i - V_x t)^2 + (y_i - V_y t)^2}{r_{spot}^2} + \left(\frac{z_{surface} - z_i}{c}\right)^2\right)} & if\ r_i(t) < r_{spot} \\ 0 & otherwise \end{cases} \quad \text{Eq 2. 16}$$

where $z_{surface}$ is the current build layer height, and c is the laser beam penetration depth. This model is more accurate since it can predict deeper melt pool. However, this model

adds another uncertain parameter, which is the penetration depth (c). In addition, it requires finer mesh at the spot region so that volumetric heat source be captured. Other simplifications to the heat source include simplifying the heat source from to line as in [31], or uniform across the layer as in [30]. These simplifications are basically used to reduce the number of simulation steps.

### 2.3.4. Material Properties

Since both powder and solid material are included in the single-track model and layer-wise remeshing approach, two material models were assigned to the build part. The material thermal properties were assumed temperature dependent, where the phase changes are included by considering the material latent heat. With the inclusion of the phase changes, the maximum temperature values become more realistic, however, the problem becomes highly nonlinear and Newton-Raphson procedure use is a must for better convergence behavior. In most simulations, Ti-6Al-4V was considered, since this material is used in many applications where reliability is required. For the solid material, the temperature dependent specific heat and density were taken from [40]. The specific heat was calculated with the assumption of powder porosity value of 0.4, although this parameter is also uncertain and may change based on location. The thermal conductivity of Ti-6Al-4V powder adopted were measured experimentally in [41]. It is assumed that the thermal conductivity of both powder particles and solid material behave similarly beyond the melting temperature. The thermal properties curves are shown in Figure 2.18.

It is worth mentioning that material model itself not only controls solution accuracy, but also the convergence behavior. The increase of the heat capacity (latent heat of fusion and

vaporization) was smoothened by the inclusion of multiple points to improve line searching during solution for better convergence behavior. Although the temperature may exceed the boiling temperature during the simulation, which may be considered as unrealistic, this is mainly because of the gradual increase of the volumetric heat capacity curve beyond the boiling temperature. Otherwise, the solution may not converge.

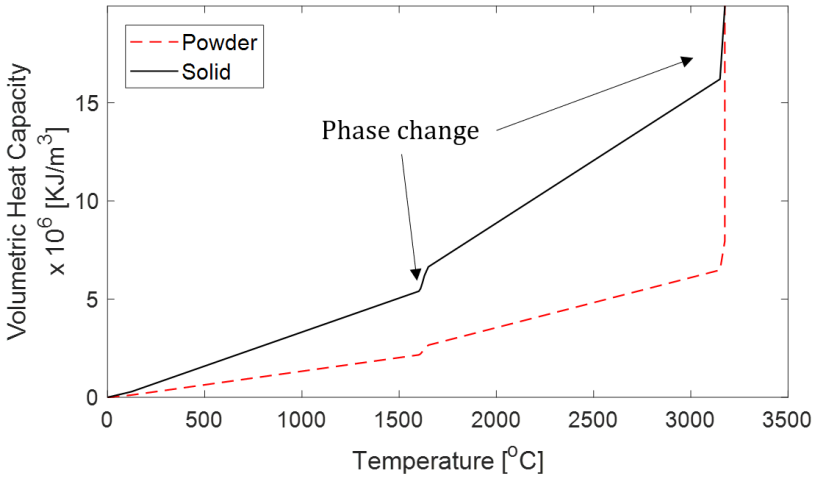


(a) Volumetric heat capacity

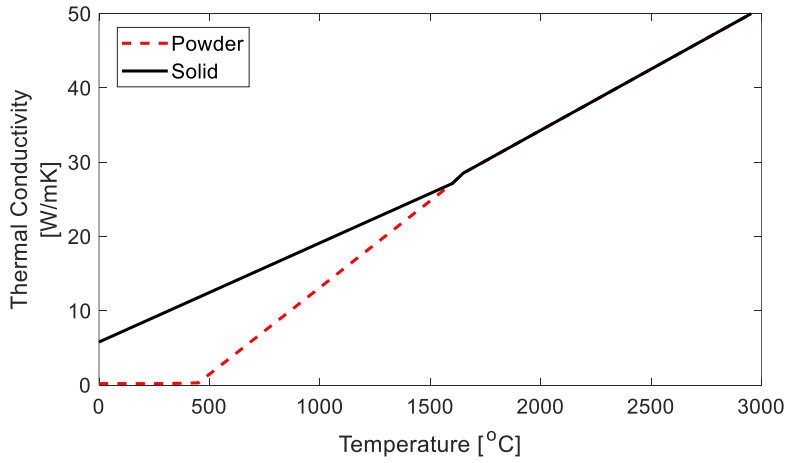


(b) Thermal conductivity

**Figure 2.18:** Temperature dependent thermal properties

### *2.4. Single Track Thermal Modeling*

The single-track model is used to validate the numerical model assumptions by comparing the melt pool prediction to the experimental results. Figure 2.19 shows the predicted melt pool width and depth by the finite element model compared to previously measured values in [42], where the absorptivity value was assumed 0.6 considering the heat source model in equation 2.14. Results show that the numerical model can predict the effect of the laser scanning speed and power. As the scanning speed increases, the melt pool size become smaller. As the laser power increases, the melt pool size becomes larger. However, there is a considerable difference between the predicted and measured values due to different reasons. Firstly, the actual process parameters in experiments may deviate from the nominal values, which is related to the experiment error. Previous measurements showed that actual process parameters may vary during the process [43, 44]. Secondly, the assumed absorptivity and surface heat flux may not represent the actual situations. Lastly, the simplifications which lead to inherent model inadequacy for representing the real physical systems. In addition, the finite element model may not be able to capture other physical phenomena such as the keyholing that takes place at high energy density and results in deeper melt pool [9]. Also, at some process parameters, the proposed numerical model is not capable of predicting the keyholing which takes place at high energy densities. As will be discussed later, the single track model is also used to calculate the heating time and maximum temperature to be applied as boundary conditions to the structural problem [45].

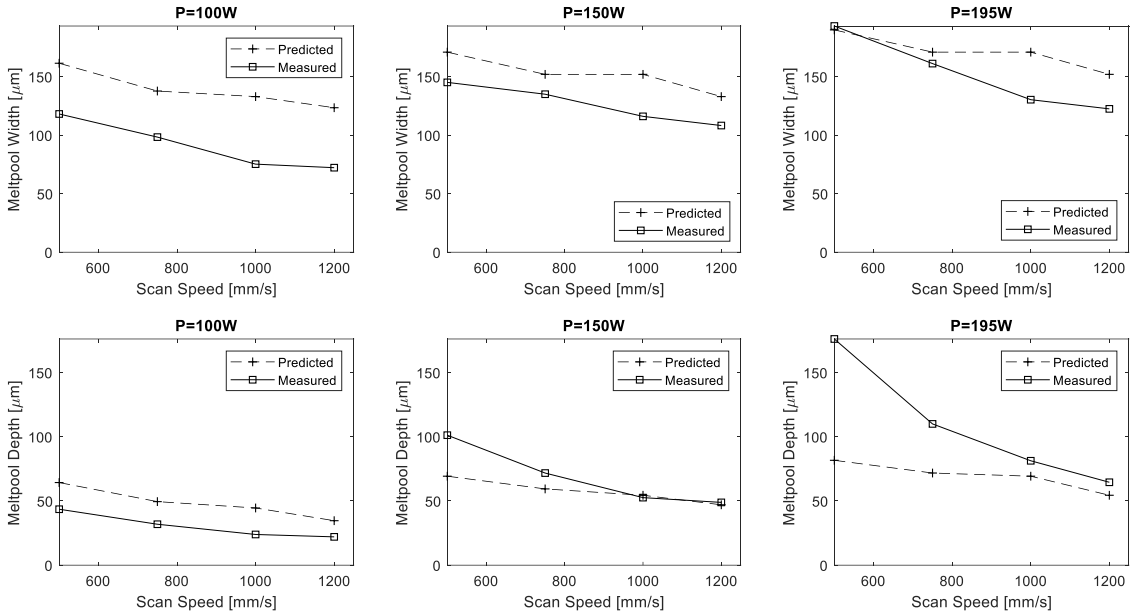


**Figure 2.19:** Melt pool size predicted by FEM compared to the experimental results in [42]

## *2.5. Part-scale Thermal Modeling*

Thermal modeling of parts manufactured by LPBF is helpful to understand the effect of process parameters on the thermal history, lack of fusion porosity, and melt pool size variation over the powder bed. As previously mentioned, part-scale modeling of LPBF without adaptive remeshing is massively computational expensive. Thus, both layer-wise and scan-wise adaptive remeshing were utilized to make the modeling computationally feasible and to understand how the these adaptive remeshing techniques affect the computational time. To investigate these, two different geometries were considered for part-scale modeling; a cube of different edge sizes (2 mm and 5 mm) as in Fig 2.11, and the cantilever structure shown in Fig 2.20.

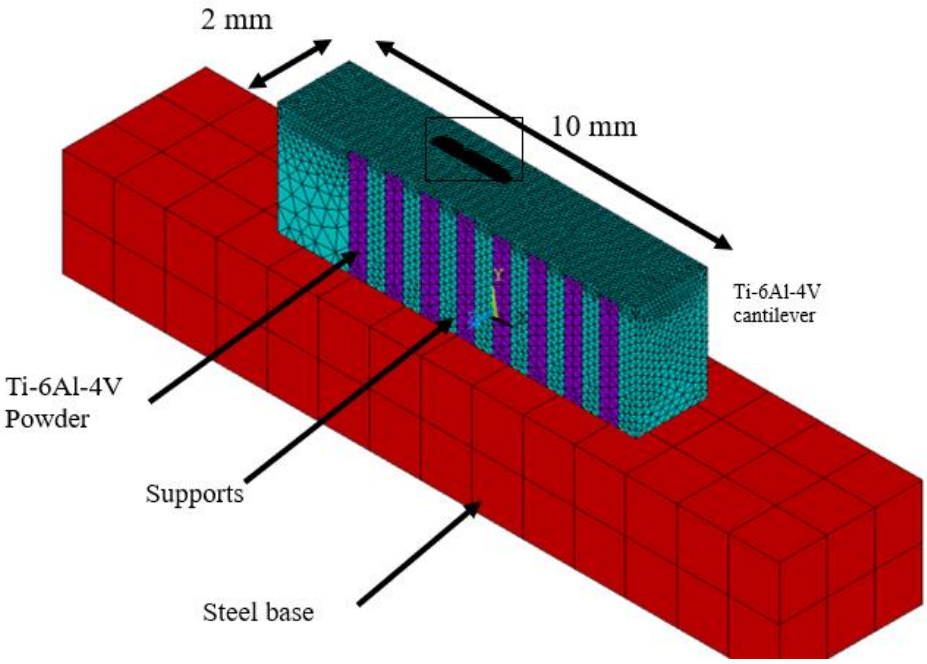


(a) Mesh configuration

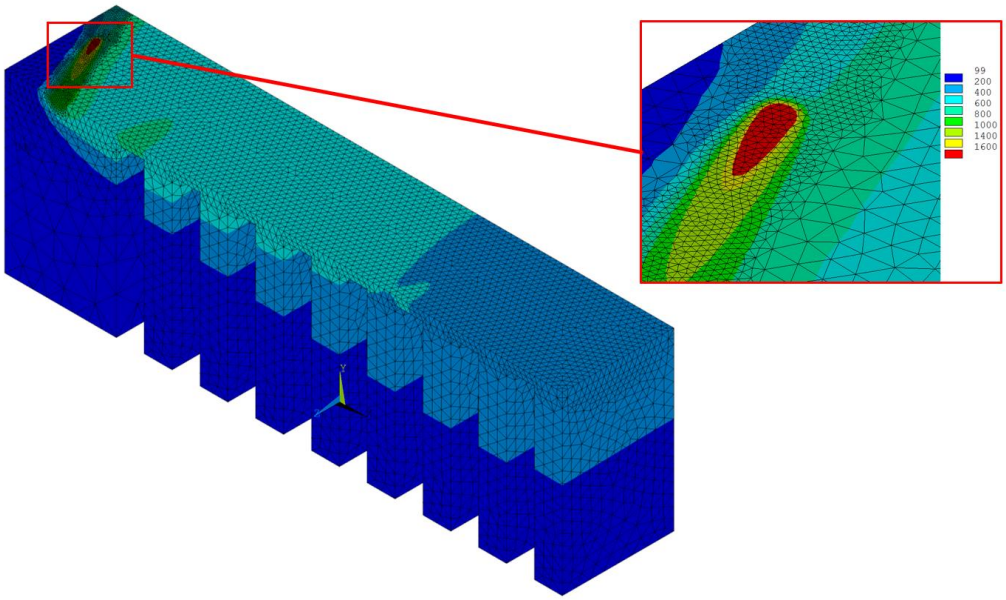


(b) Thermal solution

**Figure 2.20:** Thermal Simulation of part-scale models

### 2.5.1. Melt Pool Size

Figure 2.21 shows the melt pool size close to the part center at four levels of different processing parameters (laser power and scanning speed) predicted for 2x2 $mm^2$ layer area with layer-wise adaptive remeshing. It is obvious that the melt pool is slightly wider and also deeper at the lower level of scanning speed 500 mm/s when compared to the 750 mm/s case. The power effect on the melt pool size finds an opposite trend where the melt pool was found to be larger at the higher power level. These predicted results can find an agreement with the experimental results in [42]. The melt pool dimensions statistics is shown in Fig 2.22 where the melt pool width is overestimated and depth is underestimated from the experimentally measured values in [42]. The melt pool size in Fig 2.21 at part scale is larger than that predicted by single-track model shown in Fig 2.19 because, firstly, the melt pool size is affected by the previous scanning track which contributed to higher part temperature and residual heat effect. Secondly, the melt pool size continuously changes based on location and tend to be larger and deeper closer to the edges. The effect of the process parameters on the heat affected zone (HAZ), where the microstructural changes and induced residual stresses take place, behaves similarly as the melt pool, Figure 2.21. A larger HAZ region takes place with increased power level and/or reduced scanning speed.

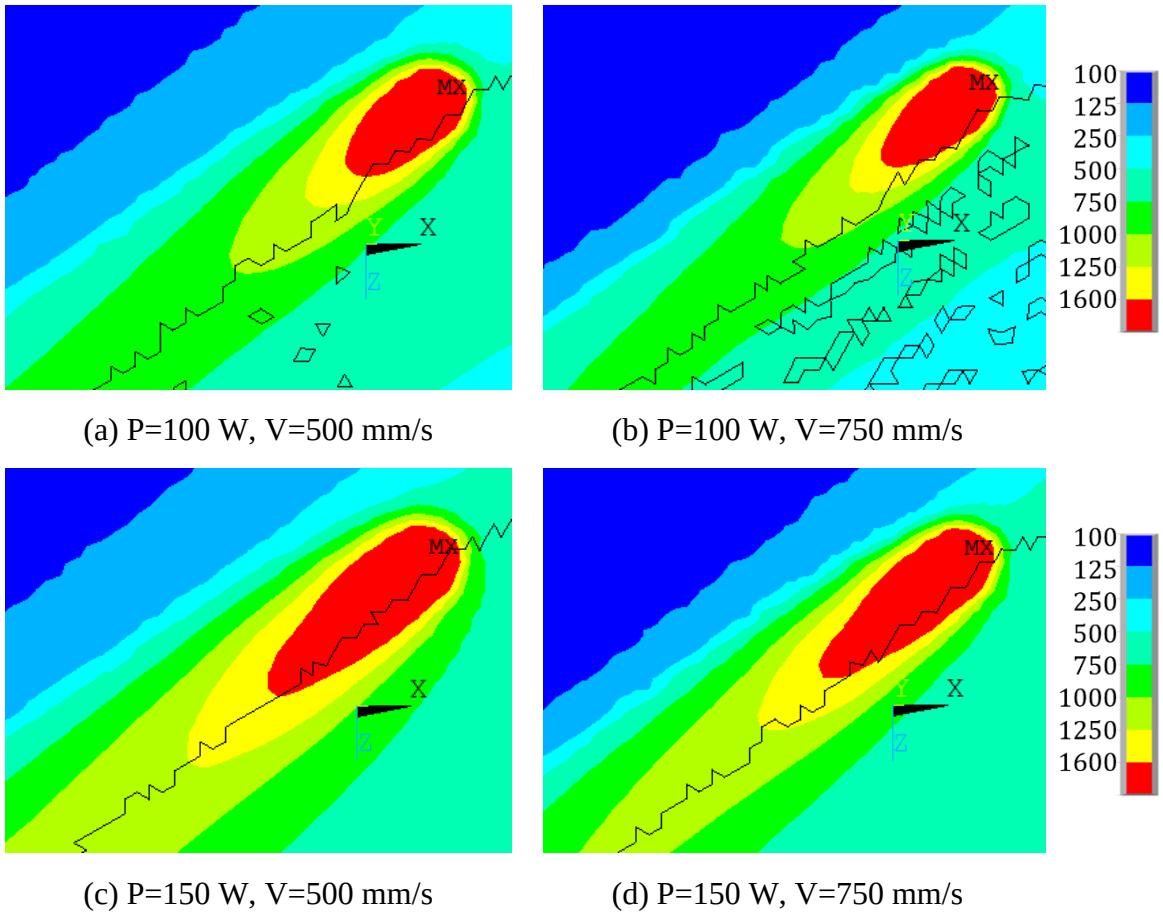


(a) P=100 W, V=500 mm/s (b) P=100 W, V=750 mm/s

(c) P=150 W, V=500 mm/s (d) P=150 W, V=750 mm/s

**Figure 2.21:** Temperature distribution during LPBF simulation with different process parameters

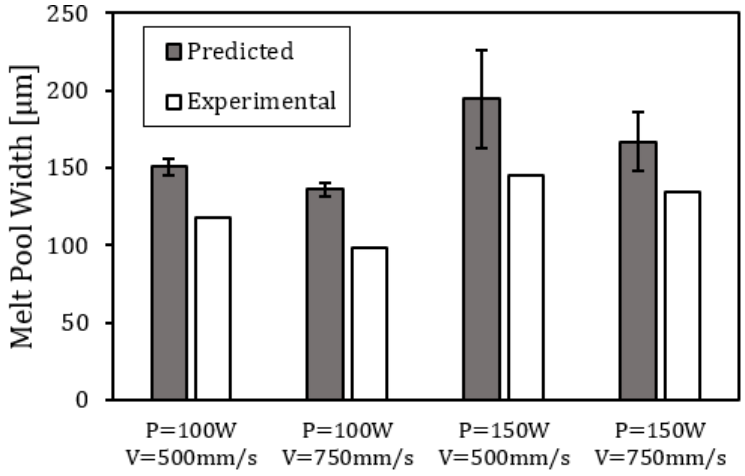


(a) Melt pool width

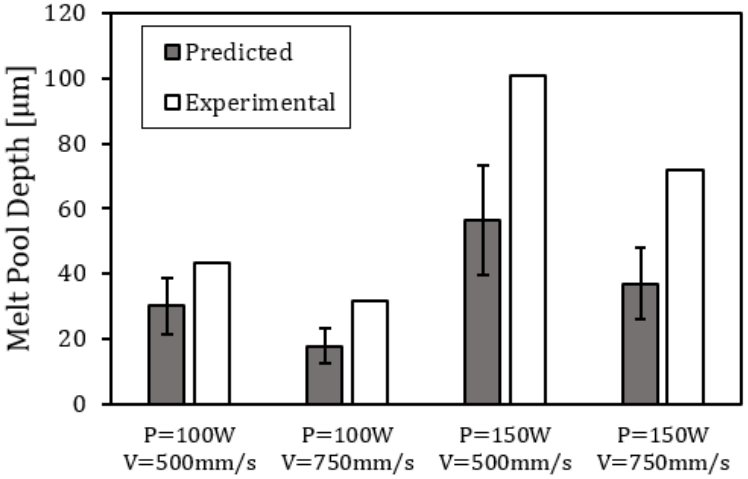


(b) Melt pool depth

**Figure 2.22:** Melt pool dimensions for different process parameters

Knowing the melt pool size location dependency is very advantageous since it delivers insights on identifying critical locations and understanding how parts' design or process parameters can be changed to avoid manufacturing defects. For instance, the large melt pool can be an indication of possible keyholing, while a small melt pool can represent potential lack-of-fusion porosity location. Although process monitoring techniques can be helpful observing melt pool length and width, the depth cannot be easily observed with

etching parts after manufacturing. Predicting location-dependent melt pool size for large parts is feasible without massive computational resources with the scan-wise adaptive remeshing approach. Figure 2.23 describes the methodology by which the melt pool size at any location can be measured. Multiple lines that are colinear and perpendicular to the scanning track across the depth, width, and length are generated. Each line includes equally spaced 250 points at which temperature results are mapped, where the melt pool size can be measured by the number of points exceeding the melting temperature. An example of the mapped temperatures and melt pool dimensions are shown in Figure 2.24. The main reason why multiple lines are used is to capture the maximum width and depth which are not always at the laser spot center.

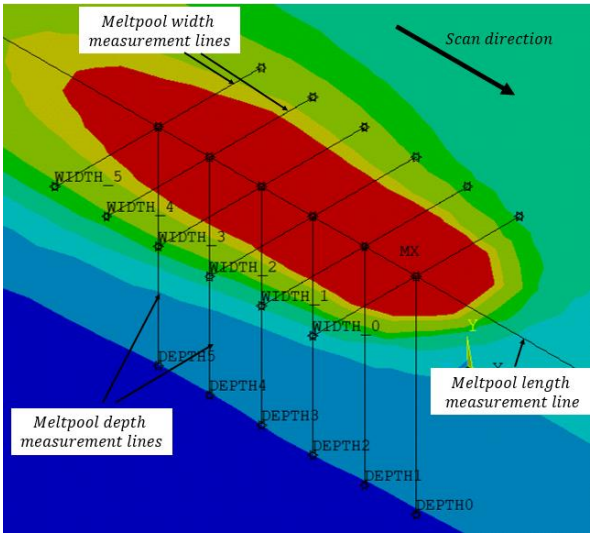


**Figure 2.23:** Melt pool measurement lines

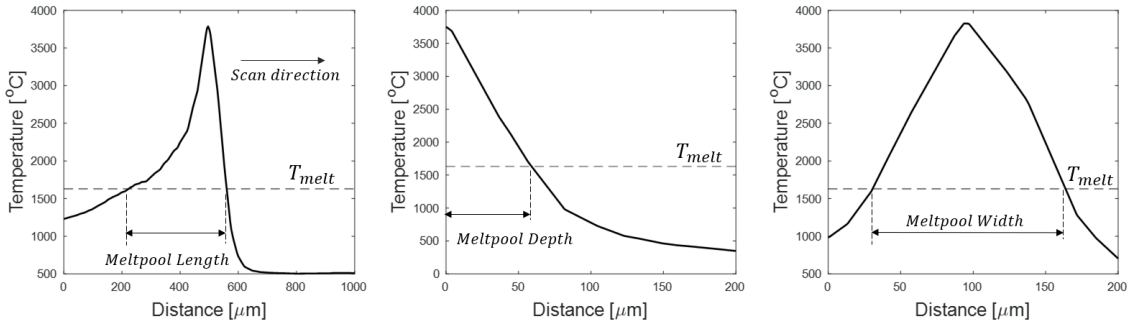


Length line Depth line Width line

**Figure 2.24:** Melt pool measurement method

To demonstrate the ability to handle large parts, a single layer of a relatively larger cantilever with support structure was considered. The layer 105 at height 3.15 mm was considered (overhang at 3 mm). The main reason why this specific layer was selected is to understand how the melt pool size is affected at overhangs. It is assumed that the last temperature after the interlayer cooling is uniform and equal to 100 $^{o}$C to avoid simulating the entire part. This assumption is valid if the part can easily lose the heat within the dwell time. Three different scanning angles for running this analysis were considered (67, 0, and 90). The location dependent melt pool size considering these different configurations is shown in Figures 2.25, 2.26, and 2.27, where the melt pool size is greatly affected at the overhangs for some scanning strategies. The variation in the melt pool size at different scanning strategies is due to the residual heat effect when the cooling time between two consecutive scanning tracks is insufficient. Figs 2.25 and 2.26 show that melt pool size variation is larger when the scanning tracks are short. However, that high variation is not the case when the long scanning tracks at scanning angle 0$^{o}$. The sudden and high variation shown in Figure 2.27 at the center is due to the mesh change. Thus, the effect of overhangs and layers underneath becomes more significant when the cooling time is insufficient.

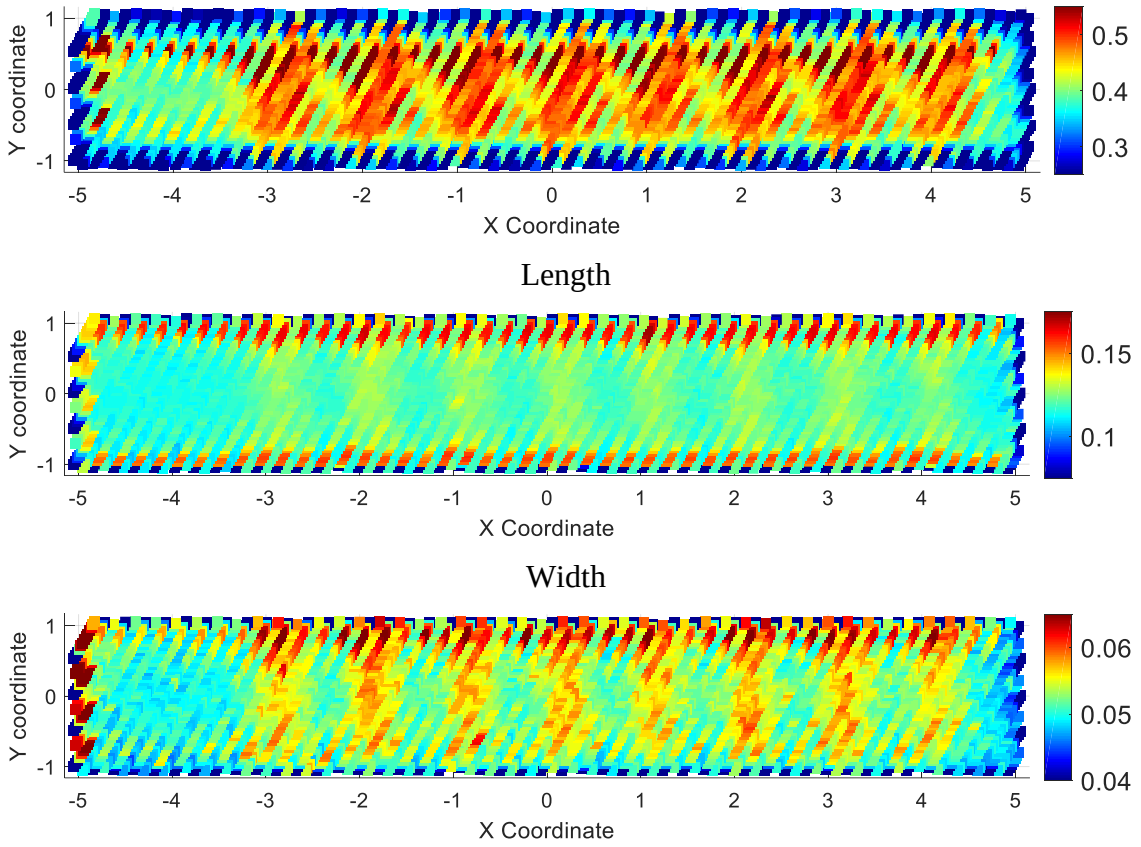


**Figure 2.25:** Melt pool size distribution for configuration 1 [46]

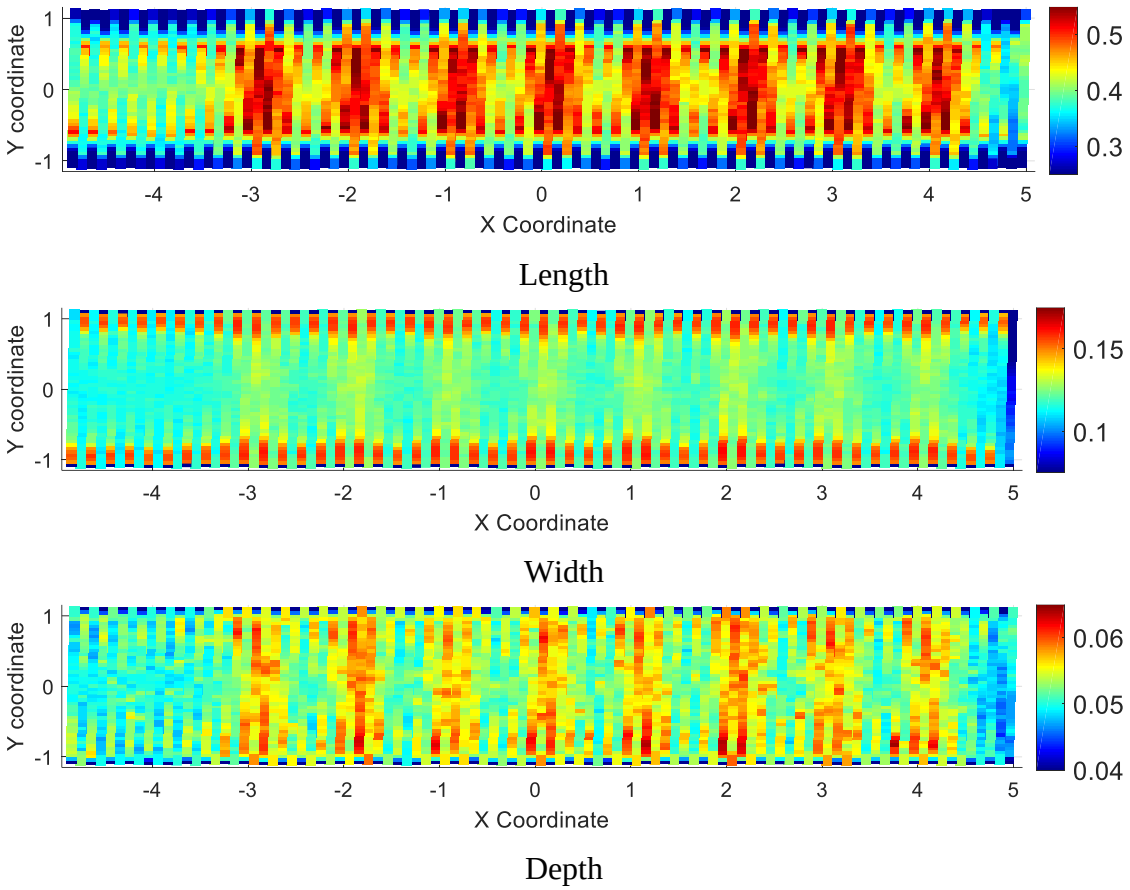


**Figure 2.26:** Melt pool size distribution for configuration 2 [46]

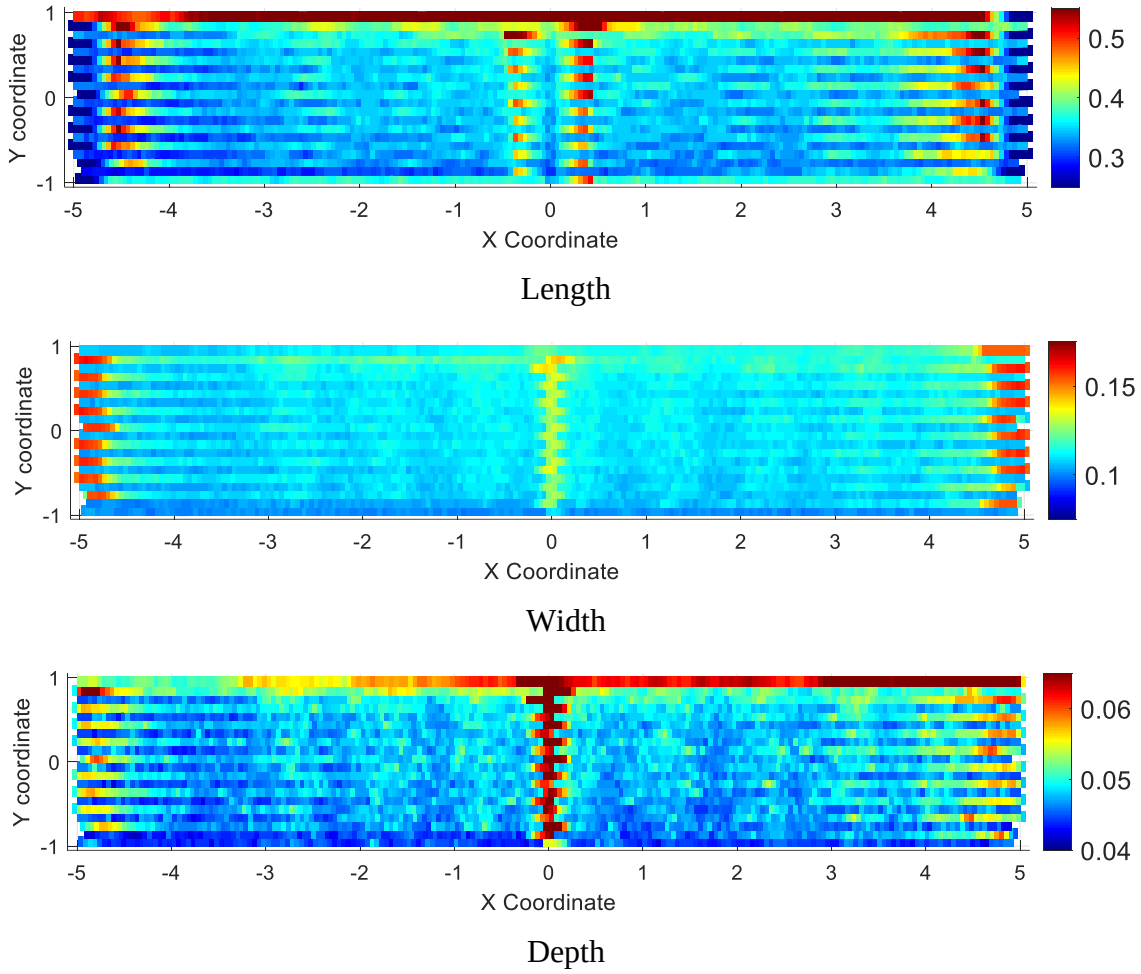


**Figure 2.27:** Melt pool size distribution for configuration 3 [46]

### 2.5.2. Lack of Fusion Porosity

As previously mentioned, lack of fusion porosity takes place due to insufficient energy density or large hatch spacing value causing incomplete melting of the powder particles. To predict lack of fusion porosity, only three consecutive layers were considered where the element size used for each layer that represents prediction accuracy is 10 µm, Figure 2.28.

The element material assignment is changed from powder to solid if all its nodes exceeded the melting temperature, even at different times. This could be an overestimation of porosity since it ignores the case of partial melting. Figure 2.29 shows the unmolten powder elements at different hatch spacing values. The fraction of these elements volume to the entire layers volume represents the porosity percentage.

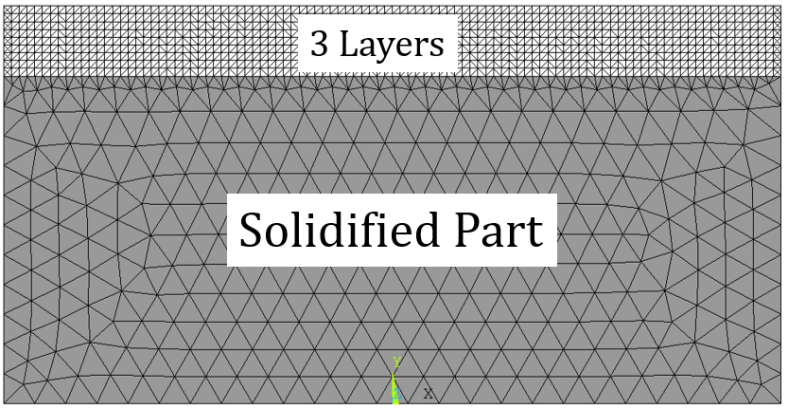


**Figure 2.28:** Mesh scheme for porosity prediction model

The effect of hatch spacing on the porosity is shown in Figure 2.30 (a). At large hatch spacing value, the melt pool overlap is insufficient to keep fully dense parts, and consequently, large pores due to un-molten particles take place. This observation finds an agreement with the experimental observations in [4]. The percent porosity values at different process parameters are shown in Figure 2.30 (b). At high power levels (P=150 W and P=195 W), parts were found fully dense. When the energy density is decreased by lowering power values, lack of fusion porosity takes place. It is obvious from the figure that at reduced power levels, or increased scanning speed, porosity is higher. These trends find an agreement with the experimental measurements in [7, 42].

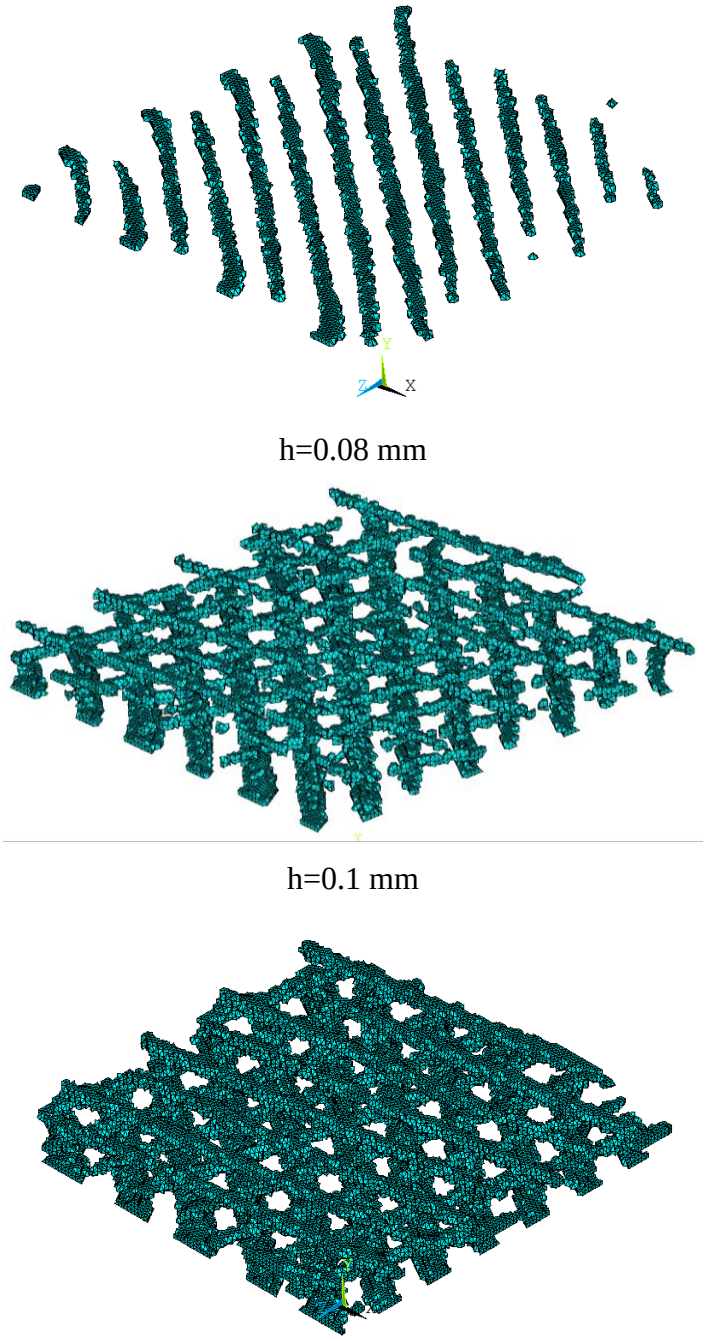

h=0.08 mm

h=0.1 mm

h=0.12 mm

**Figure 2.29:** Unmolten powder elements at different hatch spacing (h) value (P=50 W and V=500 mm/s)

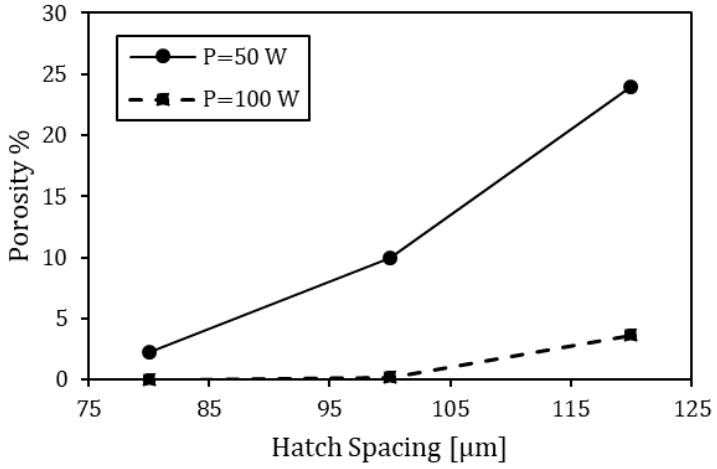


Effect of hatch spacing

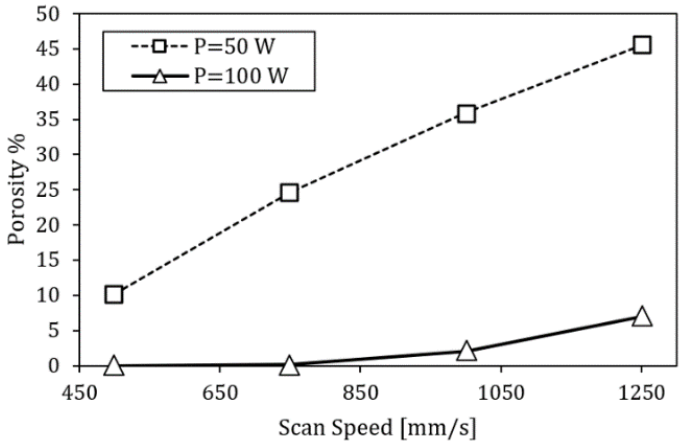


Effect of scanning speed

**Figure 2.30:** Lack of fusion porosity at different process parameters

### 2.5.3. Thermal History and hotspots identification

Tracking the thermal history is crucial to ensure all powder particles were melted and exceeded the melting temperature, understand the heating and cooling cycles, and to predict the microstructural evolution throughout the process. Figure 2.31 shows the temperature history at the center of layer 15 during the build of three consecutive layers

(layers 15 to 17). The effect of process parameters on the maximum temperature and melting cycles is significant. The maximum temperature is higher and could be close to the boiling point at increased power level and reduced scanning speed due to the higher energy density. This high temperature could be an identification of material vaporization and keyhole formation as was observed in [9, 42].

The effect of scanning the subsequent layers on the heating cycles are shown in Figure 2.31 b and c. If the melt pool is deeper than the powder layer, the material at any given point would be re-melted during scanning the following layers making a strong bond across consecutive layers. At the point of interest, the material was re-melted at the scanning layer #16 at all process parameters shown in Figure 2.31 b, and was again re-melted at the layer #17 for P=150 W and V=500 mm/s.

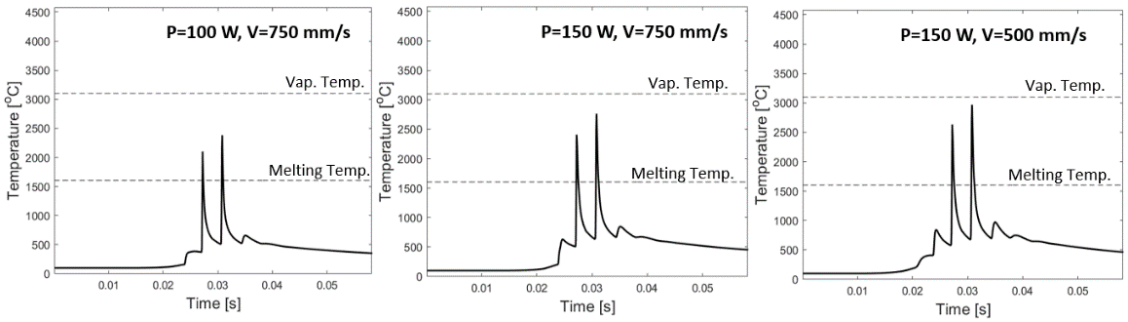


(a) Layer 15

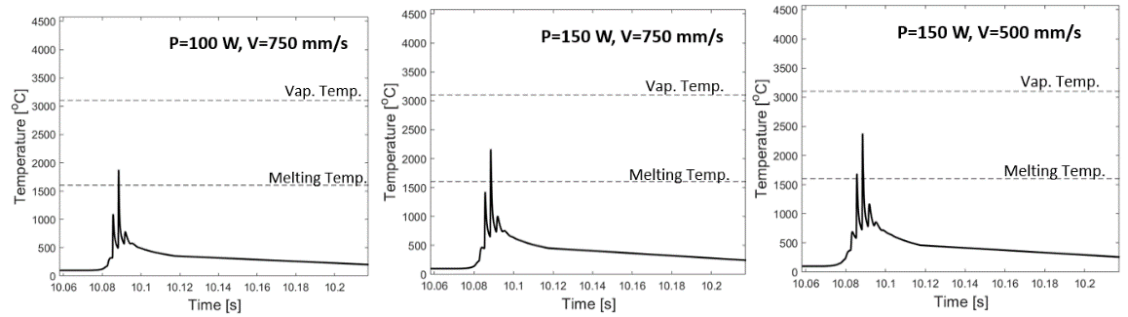


(b) Layer 16

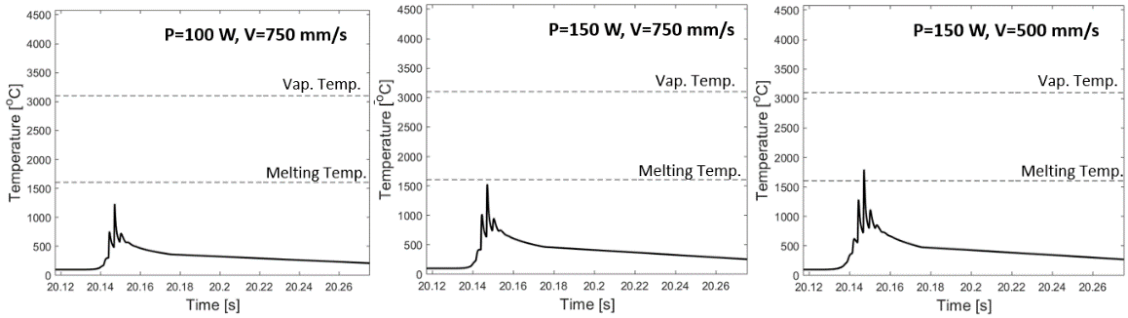


(c) Layer 17

**Figure 2.31:** Temperature history of a center point located at layer #15 in the scanning process of three consecutive layers (i.e., layer 15, 16 and 17) considering four set of process parameters

### 2.5.4. Effect of Adaptive Remeshing on Computational Time and Results

The effect of different adaptive remeshing approaches on the computational time was studied. The layer-wise and scan-wise adaptive remeshing techniques were investigated considering a simple cube with different layer areas. Figure 2.32 shows the computational time comparison between the uniform mesh case and adaptive remeshing with layer-wise adaptive remeshing. It is obvious that the computational time increases exponentially with layer area increase when uniform mesh is used. The reduction in the computational time when layer-wise adaptive remeshing is evident especially when the layer area is large. Considering a cube with layer area of 4 $mm^2$, the computational time per step and average number of nodes for the uniform mesh, layer-wise adaptive remeshing, and scan-wise adaptive remeshing is shown in Figure 2.33. The high reduction in the number of nodes when scan-wise adaptive remeshing is used reduced the stiffness matrix size and is the main reason why solver time per step is much lower than other cases.

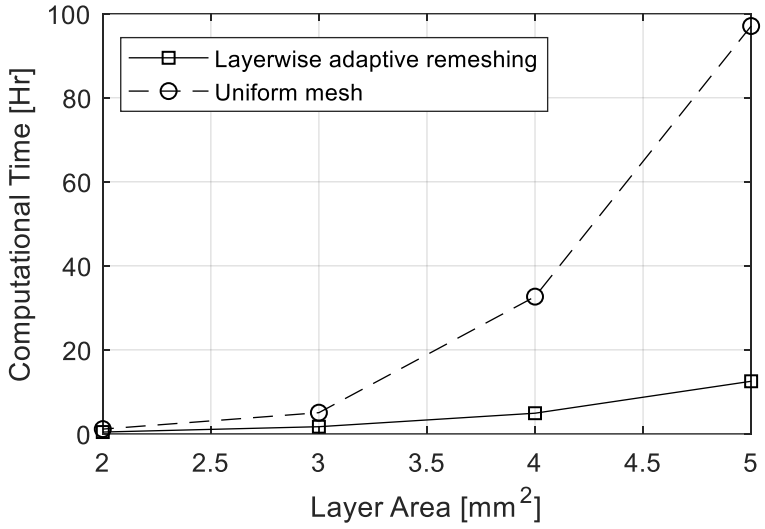


**Figure 2.32:** Computational time comparison between layerwise adaptive remeshing and uniform mesh

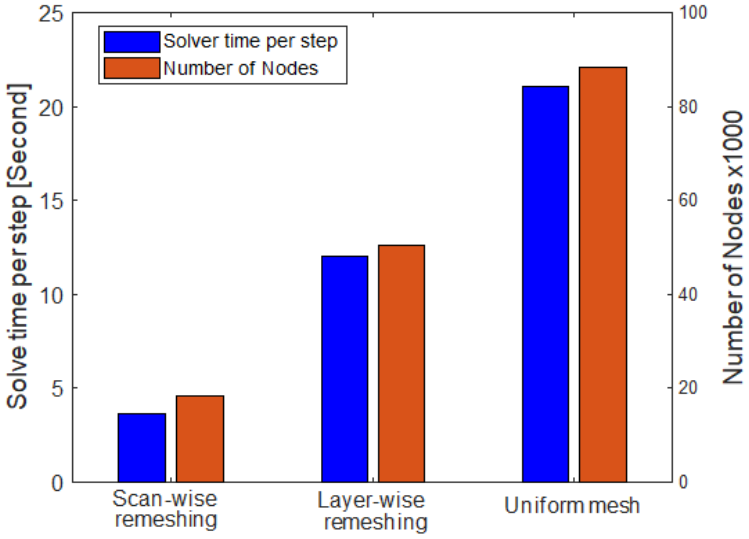


**Figure 2.33:** Computational time comparisons for 2x2 $mm^2$

Scan-wise adaptive remeshing is the most efficient solution when thermal history and melt pool size predictions are the objectives. However, as mentioned earlier, scan-wise adaptive remeshing itself requires optimization to determine the optimal refinement length value at which computational time is minimized. Thus, the effect of the refinement region length on the computational time was also studied at different layer areas (4 $mm^2$ with 3 layers, 25 $mm^2$ with a single layer). Figure 2.34 shows the total time spent in remeshing and remapping, and solver time for different refinement region length values. It was found that the total time spent in remapping and remeshing significantly reduces as the refinement region length increases due to the reduced number of tasks. From the solver side, reducing the refinement region length does not necessarily mean that the solver time will reduce since there is a fixed time associated with launching the solver and reading input files, Figure 2.34. A high solver time was associated with the minimum refinement region length since the solver was launched more times. As the refinement region length increases, the

solver time reduces until reaching an optimal refinement region length, which is 1 mm for the two cases. As refinement region length value increases, the solver time starts increasing again. Since remapping and remeshing, and solving are executed in parallel, the total of the computational time is considered the maximum of each. Figure 2.35 shows how the refinement region length affects the number of nodes and solver time per step. Both the number of nodes and solution time per step increase as the refinement region length increase, which can justify the behavior shown in Figure 2.34.

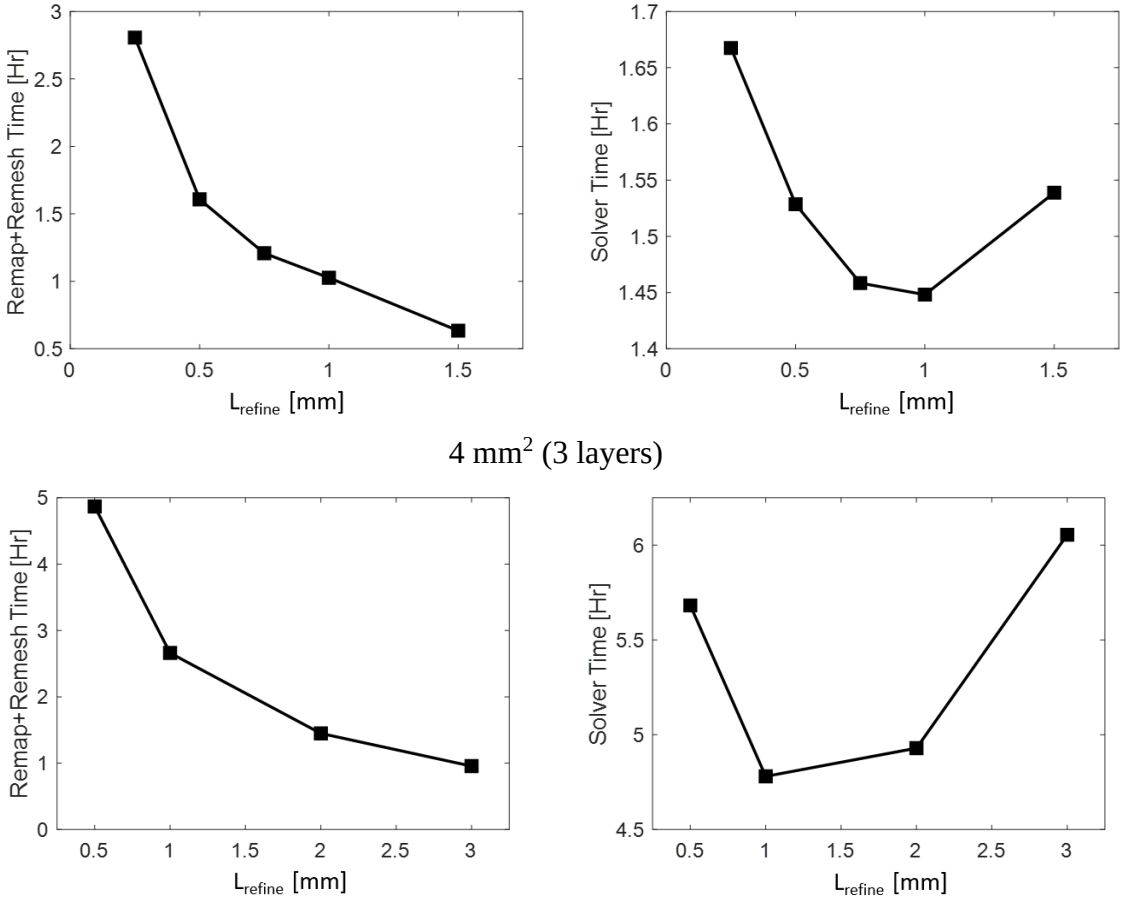


**Figure 2.34:** Effect of refinement region length on computational time.

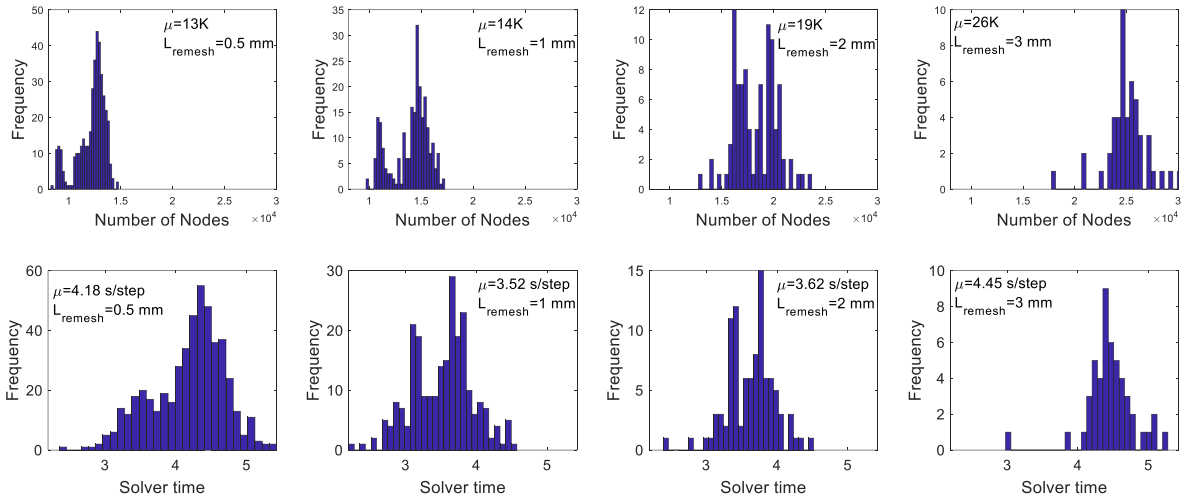


**Figure 2.35:** The effect of refinement length on the number of nodes and solver time per step for 25 mm2 area

# 3. Thermomechanical Modeling of LPBF

## *3.1. Introduction*

Residual stresses can be classified into three types [47]. Type I residual stresses are macroscopic stresses and act on part scale. Type II residual stresses are called intergranular stresses and take place due to the microstructural effects. Type III residual stresses form at the atom scale due to the vacancies. The focus in this chapter and in literature was given to type I residual stresses as this type has the most significant influence on the mechanical properties. Residual stresses can be measured by nondestructive diffraction methods such as neutron diffraction, X-ray diffraction, and the contour methods [48].

Parts manufactured by LPBF exhibit high residual stresses due to the expansion and shrinkage cycles caused by melting and solidification during the process. These residual stresses can significantly cause parts failure or distortion during manufacturing or reduce the parts' fatigue strength. Thus, understanding the residual stresses formation mechanisms is crucial since it can help towards improved quality and successful builds and avoid recoater damage. In general, parts manufacturing by LPBF are associated with high tensile residual stresses at the part surfaces and compressive residual stresses closer to the center. The high tensile residual stresses can cause parts distortions during supports removal or removing the part from the build plate and reduce fracture toughness causing quality and reliability issues. Although post-processing techniques such as heat treatment, HIP, and machining can reduce the residual stresses, optimizing the process to reduce residual stresses is still crucial to minimize the product cycle time.

The thermally induced residual stresses change from a location to another and are affected by the parts' features, material thermomechanical behavior, LPBF process parameters, base plate temperature, preheat temperature, and dwell time (time between scanning two consecutive layers). For example, the material properties were proven to have a significant effect on the residual stresses. The average residual stresses decreases as the thermal diffusivity (D) and thermal conductivity (k) increase [47, 49]. Higher material yield strength and ultimate strength increase also leads to higher residual stresses. Gu et al. [50] also reported that the thermal expansion coefficient (α) and Young's modulus (E) have a significant effect on the residual stresses as they lead to high thermal strain values. The residual stresses also depend on the process parameters including the laser power, scanning speed, hatch spacing, scanning strategy. It was reported that increasing the power level or reducing the scanning speeds contributes to higher residual stresses for different materials [51]. In addition, increasing the powder preheat temperature can significantly lead to reduced distortions and residual stresses [52].

## *3.2. Predictive Modeling Approaches*

### 3.2.1. Analytical Solution

Analytical solutions might provide a fast and efficient methods to calculate residual stresses and distortions in LPBF. Since the residual stresses are induced by the temperature gradient, the temperature solution must be obtained in advance. In an attempt to calculate the residual stresses and distortion solution during LPBF, Ning et al [53] developed a fast analytical model to calculate distortions for Ti6Al4V cantilever. Firstly, the temperature solution is obtained from analytical thermal model for single track which assumes heat

input from moving laser and heat loss due to convection and radiation. The resulted temperature solution is then added to the part through superposition method. Secondly, the temperature distribution is used to calculate the thermal stresses from which residual stresses and distortions can be calculated [54]. The predicted distortions were almost identical to the experimentally measured value and could be calculated in less than 10 seconds. The yield strength, one of the most important parameters when calculating distortions, was, however, not mentioned.

Although analytical methods are fast and efficient, they must be associated with multiple assumptions that keep accuracy questionable. For example, it is assumed that the material properties used in both the analytical thermal and stress models are constant, and temperature independent. With this assumption, the material behavior at high temperature will be misrepresented. Another assumption that was made in the analytical model is the 2D plane strain model. While this can work with some simple parts, complex parts will require the development of the 3D analytical models that are more complex to solve. Thus, relying on analytical models is not enough and the use of 3D/2D FEM is still advantages.

### 3.2.2. Numerical Solutions

Finite element models have been widely used to predict the induced residual stresses and distortions during the LPBF process. Unlike the thermal problem where there is only one degree of freedom at each node, the structural problem is more expensive since each node has three degrees of freedom. Thus, the stiffness matrix is three times larger and running simulations with the spot heat source is infeasible for large parts even with adaptive remeshing.

The multi-physics governing the Laser Powder Bed Fusion (LPBF) are sophisticated. Mesoscale finite element models that were able to represent the powder particles size and distribution randomness have been developed in [22, 23] to investigate the fluid flow, elastoplastic response and pore formation mechanisms during the LPBF. These sophisticated models were helpful to understand the complex physics behind the process but were computationally expensive. Thus, such approach for part-scale is infeasible. Macroscale single-track finite element models could also help understanding the accumulation of residual stresses during the layer-by-layer build process [49]. Such modeling methodology for part-scale is, however, infeasible because of the high number of simulations steps associated with simulating the 100μm laser beam movement along with having fine mesh representing the 30μm layer thickness. Therefore, without simplifications like the mechanical layer equivalent, where multiple true layers are merged into one layer for the structural simulation, and assumption of uniform heat source that is applied once and uniformly to the entire layer.

Unlike the thermal problem, the use of element birth and death in the thermomechanical problem is essential. The element birth and death technique was widely used to simulate the addition of new layers [32, 36, 45, 54–56]. Initially, a finite element mesh that divides the build part into multiple layers based on the assumed layer thickness is generated where all elements are deactivated. The build process is simulated by activating the layer's element layer by layer with applying the appropriate boundary condition until all layers are complete, Figure 3.1. Deactivating the elements mathematically works by multiplying each element material property by a very small number ($10^{-6}$ e.g.) [57]. As the layer is being

activated, its elements' stiffness matrix is restored to the original value based on the parts mechanical and thermal properties. It is worth mentioning that the global stiffness matrix includes the nodes of both active and deactivated elements. In other words, the stiffness matrix size does not change as the layers being activated.

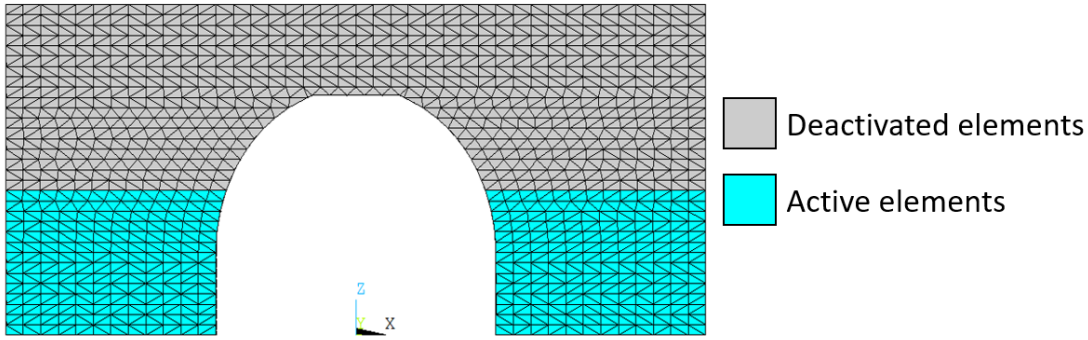


**Figure 3. 1.** Mesh configuration for thermomechanical modeling

Two approaches are widely used to simulate the structural problem for the LPBF build process. The first approach is the inherent strain (assumed strain), where there is a uniform strain value is applied to each layer as it is being activated [56, 58, 59]. This approach requires obtaining the assumed strain value through calibration against experiment solution [60], or calculation from detailed and expensive thermomechanical modeling [56]. Calculating the inherent strain from detailed thermomechanical models with a moving laser beam was proven to have poor accuracy as it is associated with some uncertainties and ignores the effect of the fluid dynamics [60]. The calibration-based approach was proven to be efficient when applied for the same geometry at which strain is calibrated. However, it fails to predict deformation and residual stresses when applied to different geometries[60]. In addition, the author believes that the inherent strain calibration framework should also include residual stresses.

The other approach relies on the thermo-mechanical simulation approach, where the thermal problem is solved first, and then the temperature history is imported to the structural problem as boundary conditions. This approach requires more time than the assumed strain approach since more time is needed to solve the thermal problem.

There was significant number of research studies where the residual stresses during LPBF were studied. Hussein et al [26] developed a small-scale model where a single layer with multiple scan-tracks were simulated for SS316L. It was observed that stresses exhibit cyclic behavior, where tensile stresses are induced during heating, and compressive during cooling due to the shrinkage. Li et al. [55] developed a framework for the thermo-mechanical simulation using ABAQUS and hexahedral elements to predict distortions and residual stresses and distortions for part-scale. Firstly, a single-track thermal simulation is used to calculate the heating time. Secondly, the layer-by-layer part-level thermal simulation with body heat flux boundary condition that lasts for the period of the heating time is solved. Finally, the temperature history is imported to the structural problem as a body force. The framework was validated by AlSi10Mg cantilever example where the distortions and residual stresses were validated against experimental solution. As per their finding, the distortion solution after cutting the support structure follows a similar trend of experimentally measured values. However, the distortion solution was underestimated compared to the experimental solution by 28%. In a later study, they developed models for different parts including bridge structural and L-shaped bar to investigate the effect of the heat flux when in patterns that are like the scanning strategy and [45]. As per their findings, slight differences in the distortion solutions were obtained. The predicted residual stresses

for the L-shaped bar, and curling angle for the bridge structure could found an agreement with the experimental solution. In addition, as the number of layers representing parts increases from 5 to 20 layers, solution becomes closer to the experimental solution. It is believed that the authors were unable to investigate with larger number of layers due to the computational expensiveness of this problem. Ganeriwala et al. [61] developed a finite element model to predict part distortions and residual stresses using the Multiphysics code Diablo developed at Lawrence Livermore National Laboratory considering the strain rate effects. The predicted strain components distributions could find acceptable agreement with the experimental solution. Furthermore, the consideration of strain rate sensitivity was found to be insignificant on the solution.

Thermomechanical modeling with the assumptions of uniform heat source along with mechanical equivalent layers was proven to be efficient predicting residual stresses and distortions. However, the computational expensiveness of this problem remains a challenge. Although it was reported that having a large number of layers representing parts improves models accuracy in [45], having large number of layers might be infeasible for large parts as it will result in a greater number of nodes, larger stiffness matrix size, and number of solution steps. Thus, there is an optimal layer thickness by which a compromise between accuracy and efficiency can be achieved.

Layer-wise adaptive remeshing in LPBF thermomechanical modeling could help reducing the computational time by coarsening the mesh where the temperature and strain gradients are low and keeping fine mesh at the build layers where high temperature and strain gradients are expected. Previous framework where adaptive remeshing was used for the

LPBF thermomechanical problem was discussed by Gouge et al. in [36] and currently available in Autodesk NetFabb. Their proposed mesh coarsening approach relies on the use of voxels and octrees adaptivity by which every 8 voxels are merged into one coarser voxel and their averaged solution is mapped to the new voxel. The first limitation of the software is that only cubic shaped elements are used. Thus, parts' curvatures and complex features are not well represented using coarse mesh, and fine elements are needed to maintain geometrical complexity, Figure 3. 2. Secondly, the adaptive meshing framework is associated with a simplification in the element formation as there is no mesh connectivity at the coarse element mid-side node. In addition to that, the software utilizes a multi-scale modeling approach in which a small-scale model is used to calculate basic variables such as temperature, strains, and stresses and then results are mapped to the large-scale model. What is being mapped and how the framework works remain proprietary.

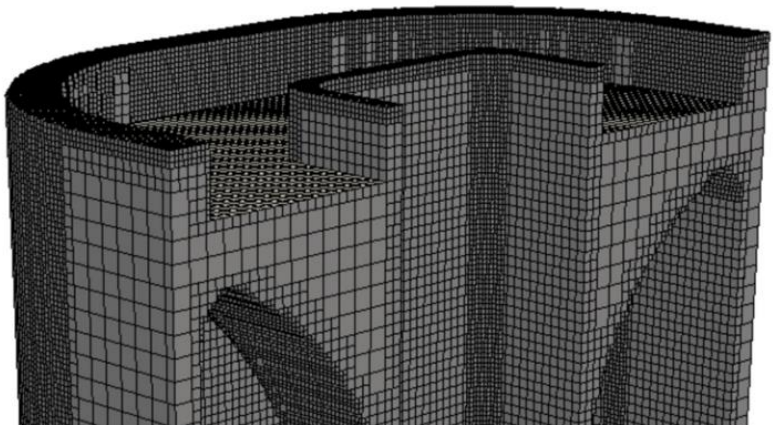

**Figure 3. 2.** Autodesk NetFabb Adaptive Meshing with 2 levels of mesh adaptivity [36]

### *3.3. Research Motivation and Contribution*

Although there had been some research studies where well-developed finite element models were described, the computational time for this problem is still a challenge. Since the model accuracy improves as the assumed mechanical equivalent layer thickness becomes closer to the true layer thickness [45], a compromise between accuracy and computational time must be achieved. Like the thermal problem, the use of adaptive remeshing in the thermomechanical problem can make this problem more efficient and feasible on modest computational resources. Applying adaptive remeshing in the structural problem is however difficult and effortful as more iterations are needed to reach equilibrium state after each remeshing task.

The motivation in this chapter is develop an understanding of the induced residual stresses and distortions during LPBF and to develop a complete framework where adaptive remeshing can be applied to the thermomechanical problem utilizing existing well-developed general-purpose solver, like ANSYS, and with using tetrahedral mesh that can represent parts complex features with less number of nodes compared to the previously developed framework using voxels [36]. The adaptive remeshing technique utilized in this work is similar to the nonlinear adaptivity (NLAD) framework developed by ANSYS [62] and also adopted in machining and forming simulations [63] to tackle large deformations. The use of adaptive remeshing in NLAD and large deformation applications has however different objective. In large deformation applications, the adaptive remeshing is needed to replace the old deformed and distorted mesh with a new mesh with acceptable element shape. For such applications, adaptive remeshing criteria is controlled by different

measures like elements shape, energy, etc. The objective of using adaptive remeshing in AM simulation is different as AM or LPBF simulations are not involved with large deformations like machining or forming. It can however help keeping fine mesh at the high stress and strain gradients regions, and coarse elsewhere achieving a significant reduction in the stiffness matrix size and computational time as will be discussed later in this chapter.

The developed adaptive remeshing framework for the structural problems contributes to the literature by being the first where a complete framework to efficiently solve the thermomechanical problem is developed utilizing general-purpose ANSYS solver. The framework makes use of the higher-order quadratic tetrahedral elements (SOLID187) that can help avoiding the drawbacks of the voxels-based adaptive remeshing by representing all parts' curvatures and thin features with a smaller number of nodes.

The thermomechanical modeling of LPBF using finite element is validated using multiple 3D models from different materials (Ti6Al4V bridge, IN718 canonical, and IN625 NIST AMB2018-01 cantilever parts).

## *3.4. Thermomechanical Modeling Description*

### 3.4.1. Boundary Conditions

As mentioned earlier, unlike the thermal problem, the addition of new layers in the thermomechanical is represented by the element birth and death. The powder material properties are applied to all part's layer before building any layer. A schematic about the boundary conditions used in the thermomechanical modeling is shown in Figure 3.3. The material melting temperature is used as a temperature boundary condition for each new

layer at the same step of activation. During this step, the layer slightly expands due to the assumed low thermal expansion coefficient of the powder. This heating step is followed by a cooling step where the layer material assignment changes from powder to solid and heat loss is allowed by convection (h=10 W/m$^2$K and T=25 $^o$C) at the build layer. During this cooling step, the shrinkage due to the reduced temperature results in accumulating residual stresses that may remain until the build is complete. It is worth mentioning that build part is bonded to the build plate by a Multi Point Constraint (MPC) contact formulation where heat transfer by conduction is also allowed.

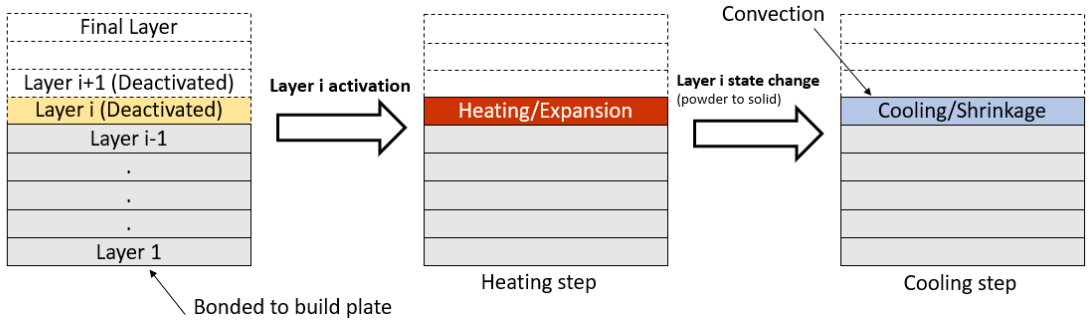


**Figure 3. 3.** Boundary Conditions for LPBF process thermomechanical modeling

### 3.4.2. Adaptive Remeshing Framework

The thermal part of the thermomechanical problem is very similar to what was previously discussed in chapter 2. The adaptive remeshing mechanisms are however different. In the layerwise adaptive remeshing, a new mesh was being generated for each new layer. For the structural problem, generating a new mesh every layer is computationally expensive as mapping the structural problem solution (e.g. stresses, strains, etc.) requires performing iterations until equilibrium state is achieved. Thus, the adaptive remeshing in the

thermomechanical model is set to be less frequent and controlled by the number of layers being solved before remeshing takes place (N). Like the thermal problem, the Ansys remeshing engine was utilized to handle all remeshing tasks.

The Ansys rezoning feature was used to map the solution at the changed mesh region. The rezoning feature current limitation is that it does not run in distributed mode. Thus, structural problem remapping computational time is longer than that that of the thermal problem discussed in section.

The mesh configuration adopted in this analysis relies on the use of tetrahedral elements available in Ansys (Solid87 for the thermal problem, and Solid187 for the structural problem). These tetrahedral elements are nonlinear and high-order which have ten nodes and are supported by the advanced Ansys remeshing engine and rezoning features. As mentioned earlier, the use of this tetrahedral element is advantageous as it allows having high mesh growth rate and representing curvatures with less elements compared to the voxel-based remeshing approach. During simulation, each part being built is divided into three regions: 1) *N* layers being solved, 2) previously solved layers, and 3) future layers to be solved. The mesh must be kept fine at the layers being solved, and coarse at both the previously solved and future layers to reduce the size of the stiffness matrix. An example of the initial mesh configuration where all part elements are deactivated considering $N$=10 is shown in Figure 3.4. After activating and solving each *N* layers, mesh is coarsened at these layers and refined at the following *N* layers, Figure 3.5.

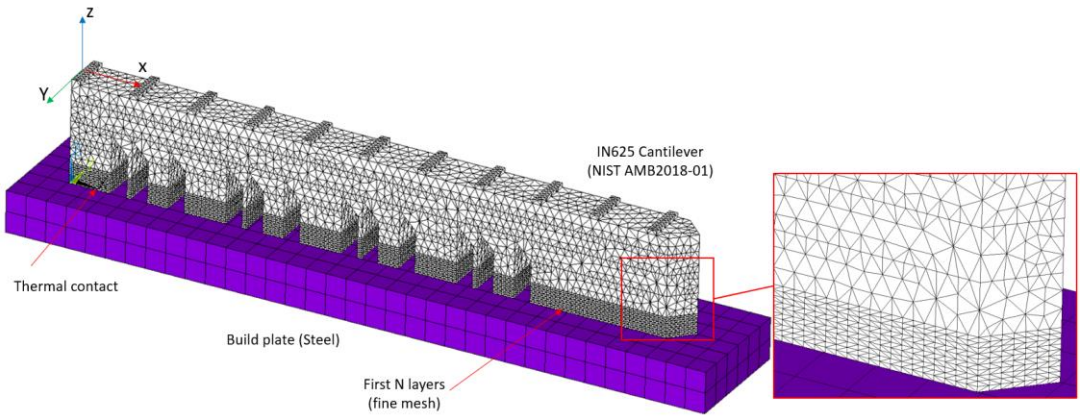


**Figure 3. 4.** Mesh and adaptive remeshing configuration for NIST cantilever

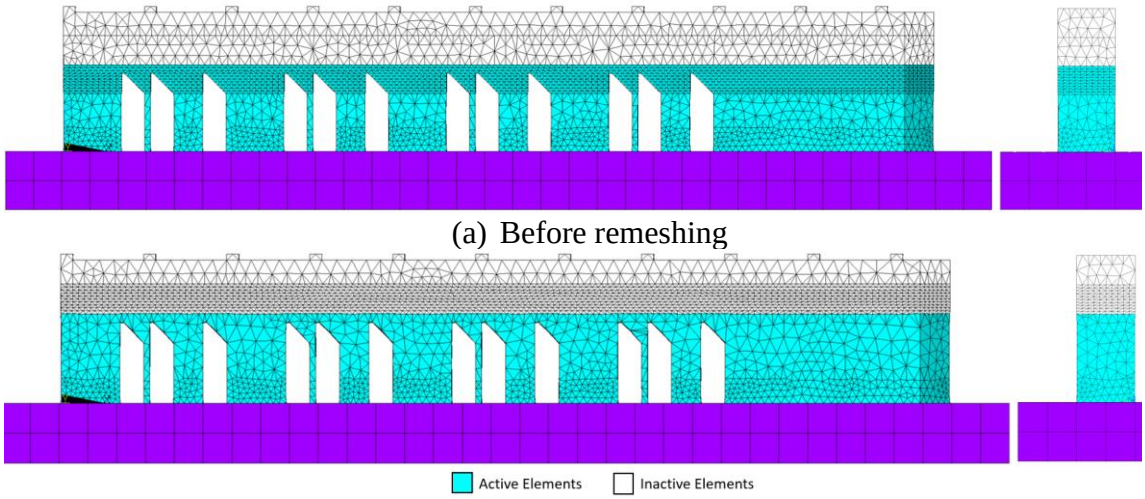


(a) Before remeshing

(b) After remeshing

**Figure 3. 5.** Mesh configuration with N=10 and C=3.5

The value of *N* controls the remeshing frequency and significantly affects the computational time. A large N value would keep high number of nodes throughout the simulation and results in longer solver computational time but shorted remapping and remeshing time. Small *N* values result in higher remeshing and remapping time, but shorter

solver time. Thus, there is an optimal *N* for each part at which the computational time can be optimized.

Another controllable parameter during adaptive remeshing is the level of mesh coarsening (C). The value of C controls number of nodes and stiffness matrix size after remeshing takes place. However, it is worth mentioning that mapping solution during adaptive remeshing could be associated with significant loss of data if the new mesh is coarser. Therefore, the C value should be chosen to accuracy is maintained while computational time could be minimized. An example of how two mesh coarsening levels control mesh size is shown in Figure 3.6. A large *C* value can significantly reduce the number of nodes. However, temperature, stress, and strain distributions after remapping might not be close to those of previous mesh. Therefore, the mesh coarsening level is constrained to ensure accurate remapping and keep the fine details at high strain gradient regions. The effect of *N* and *C* values is investigated in this study.

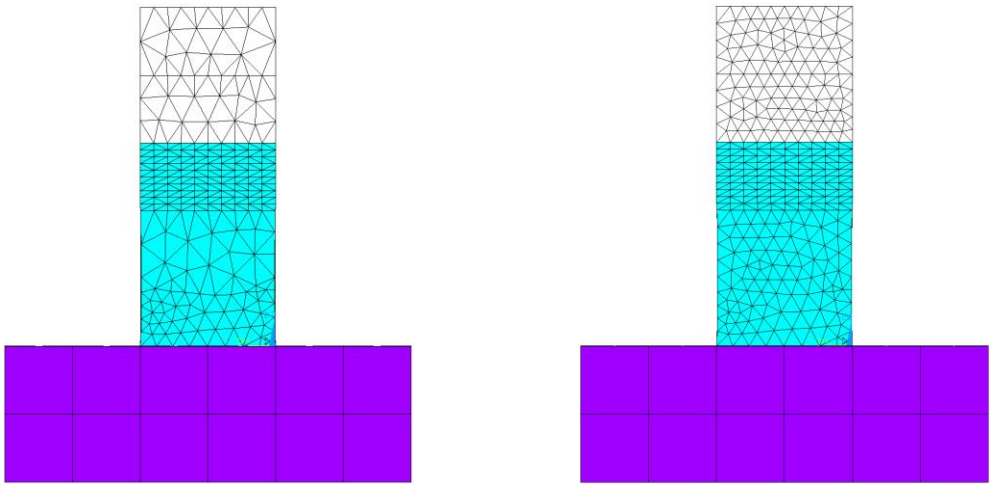

(a) C= 3.5 (b) C=1.75

**Figure 3. 6.** Mesh configuration for two different coarsening levels

The fully automated framework for the thermomechanical problem with adaptive remeshing, developed in Python, is shown in Figure 3.7, where the three main inputs include CAD file for build part, value of assumed layer thickness, and remeshing related parameters (N and C values). The initial generated mesh, Figure 3.4, includes a fine mesh at the first N layers and coarse mesh at all future layers (deactivated elements). A developed Python code reads the mesh information and generates the input files for the thermal and structural problem accordingly. Solving the thermomechanical problem works by solving the thermal problem first and use the thermal solution as a boundary condition to the structural problem where the thermal stresses are calculated. Once the first N layers are solved, this fine mesh is coarsened using the remeshing engine, and the next set N+1 to 2N layers are refined. Changing the mesh during solving is being performed under the rezoning framework, and the solver proceeds with the new mesh.

The process continues until all layers are built. The main adaptive remeshing parameters introduced in this work are: i) the number of layers being solved between remeshings (N), and ii) the adaptive remeshing coarsening level (C). These parameters are controllable and significantly affect the computational time. Three case studies were considered for this framework validation: (1) IN718 canonical part, Figure 3.8, (2) IN625 NIST AMB2018-01 cantilever [64], Figure 3.4, and (3) Ti6Al4V bridge part. Distortion for the canonical part takes place during manufacturing, while for the NIST cantilever and bridge, it takes place due to the spring back effect after cutting the support structure. The canonical part was primarily used to show the advantages of the proposed tetrahedral mesh-based adaptive remeshing technique compared to the adaptive remeshing technique, based on

voxels with octree H-adaptivity layerwise remeshing, proposed in [36, 65]. The assumed layer thickness value was assumed 0.25 mm for the NIST cantilever and bridge parts and 0.5 mm for the canonical part. The simulations were run on modest computational resources and only a single core (processor i7-7700) is used for each run.

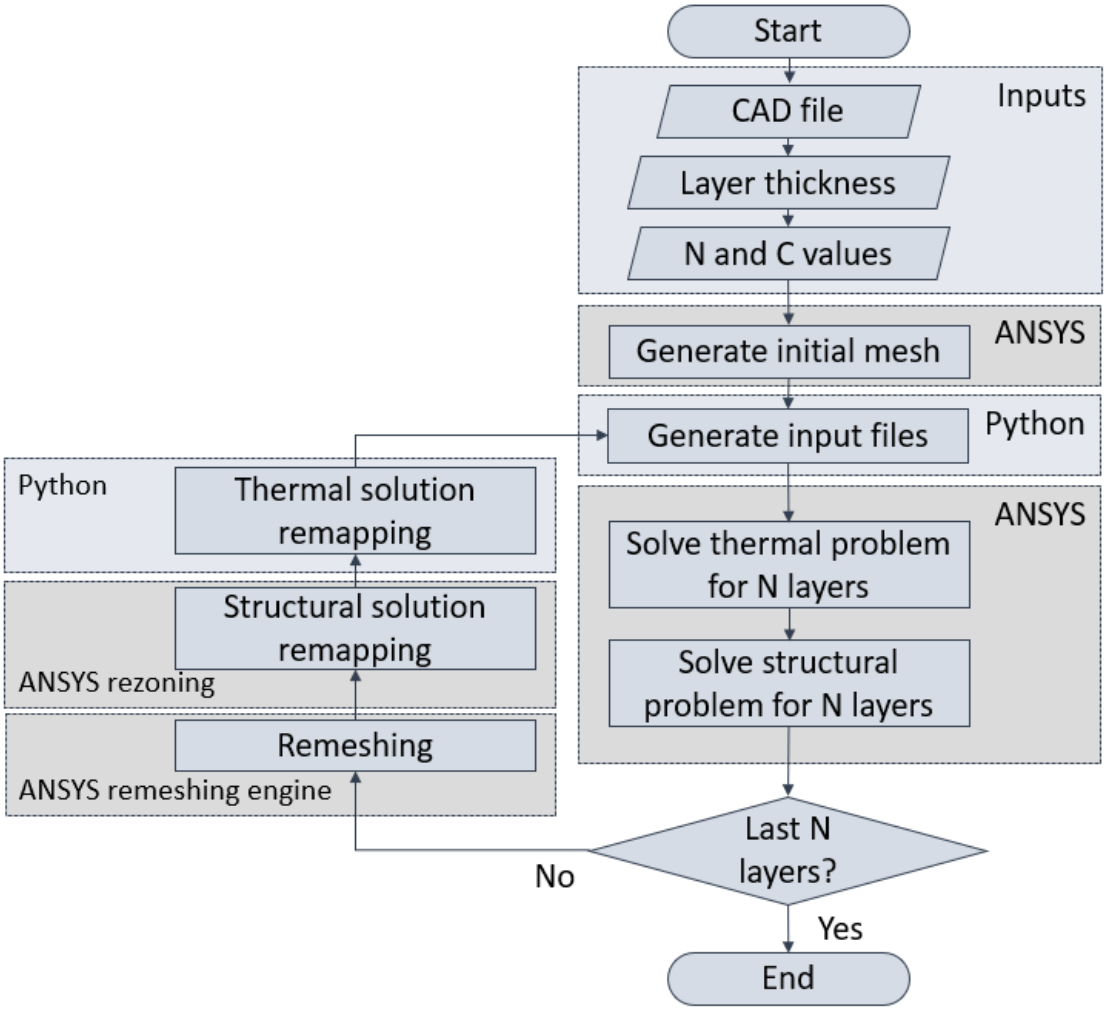


**Figure 3. 7.** Framework for the thermomechanical problem with adaptive remeshing

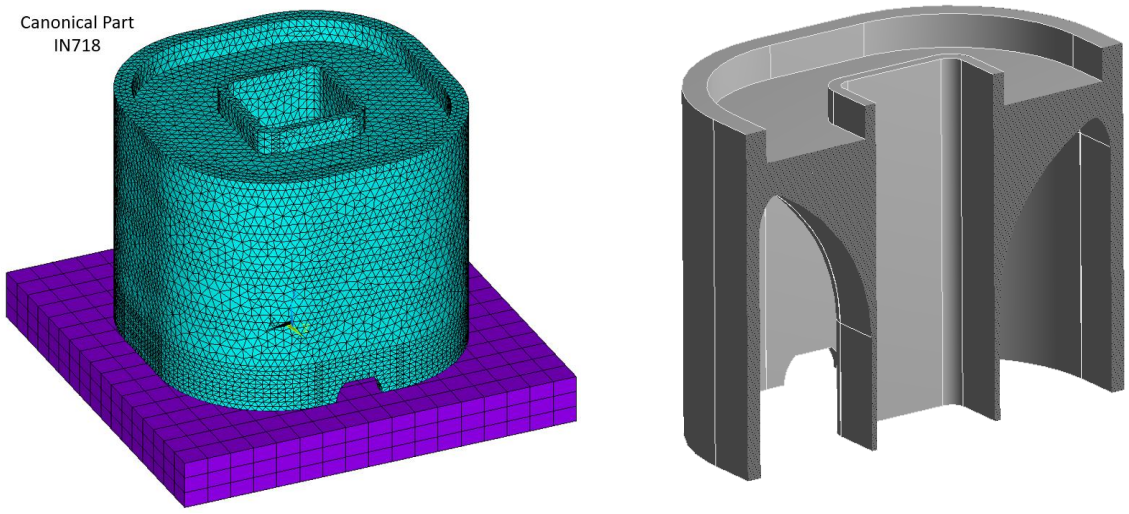


(a) Initial mesh configuration (b) Part thin walls

**Figure 3. 8.** IN718 square canonical part

### 3.4.3. Thermomechanical Material Modeling

Parts manufactured by the LPBF were reported to have different mechanical properties from parts manufactured from wrought materials. The differences could be due to the porosity that have a significant effect on the properties and microstructure. In thermomechanical modeling of LPBF process, material properties from experimental measurements of additively manufactured parts were used. One challenge is that mechanical properties for additively manufactured parts by the same machine exhibit high variability compared to other manufacturing techniques [66]. This variation can have a significant effect on solution accuracy. For instance, the parts' induced residual elastic strain during the process is linearly proportional to the yield strength value. Thus, the material parameters assumption is critical as they affect model accuracy.

Three materials were validated and used in the current framework: (1) IN625, (2) IN718, and (3) Ti6Al4V. The yield strength, Young's modulus and thermal expansion coefficient were taken from the manufacturer datasheet [67]–[69], Table 3.1. The plasticity curves at the room temperature were obtained from [70]–[72], and calculated from the thermal softening coefficient at high temperature [72]–[74], Figure 3.9, such that:

$$\sigma = (A + B\varepsilon^n)\left(1 - \left(\frac{T-T_0}{T_m-T_0}\right)^m\right) \qquad \text{Eq. 3. 1}$$

Where A, B, n, and m are material constants. A represents the initial yield strength, B and n represent the strain hardening effect, m is the softening coefficient that represents the temperature dependency, T is the temperature, $T_m$ is the melting temperature, and $T_0$ is the reference temperature. Eq. 3.1 was obtained from Johnson-Cook equation that can represent the material behavior at high temperatures after eliminating the strain rate sensitivity effects [75].

Table 3. 1. Mechanical and thermal properties for IN625, IN718, and Ti6Al4V

| | | IN625 | IN718 | Ti6Al4V |
|---|---|---|---|---|
| Elasticity modulus E(T) | [GPa] | 170-0.1146*T | 170-0.0615*T | 107-0.0229*T |
| Poisson's ratio | | 0.3 | 0.3 | 0.3 |
| Thermal conductivity K(T) | [W/m.K] | 9.5+0.0119*T | 9.5+0.0078*T | 5.8+0.015*T |
| Specific heat $C_p(T)$ | [KJ/Kg.K] | 429+0.1*T | 429+0.127*T | 542+0.17*T |
| Density | [$Kg/m^3$] | 8440 | 8150 | 4405 |
| Melting Temperature | [$^oC$] | 1300 | 1300 | 1630 |

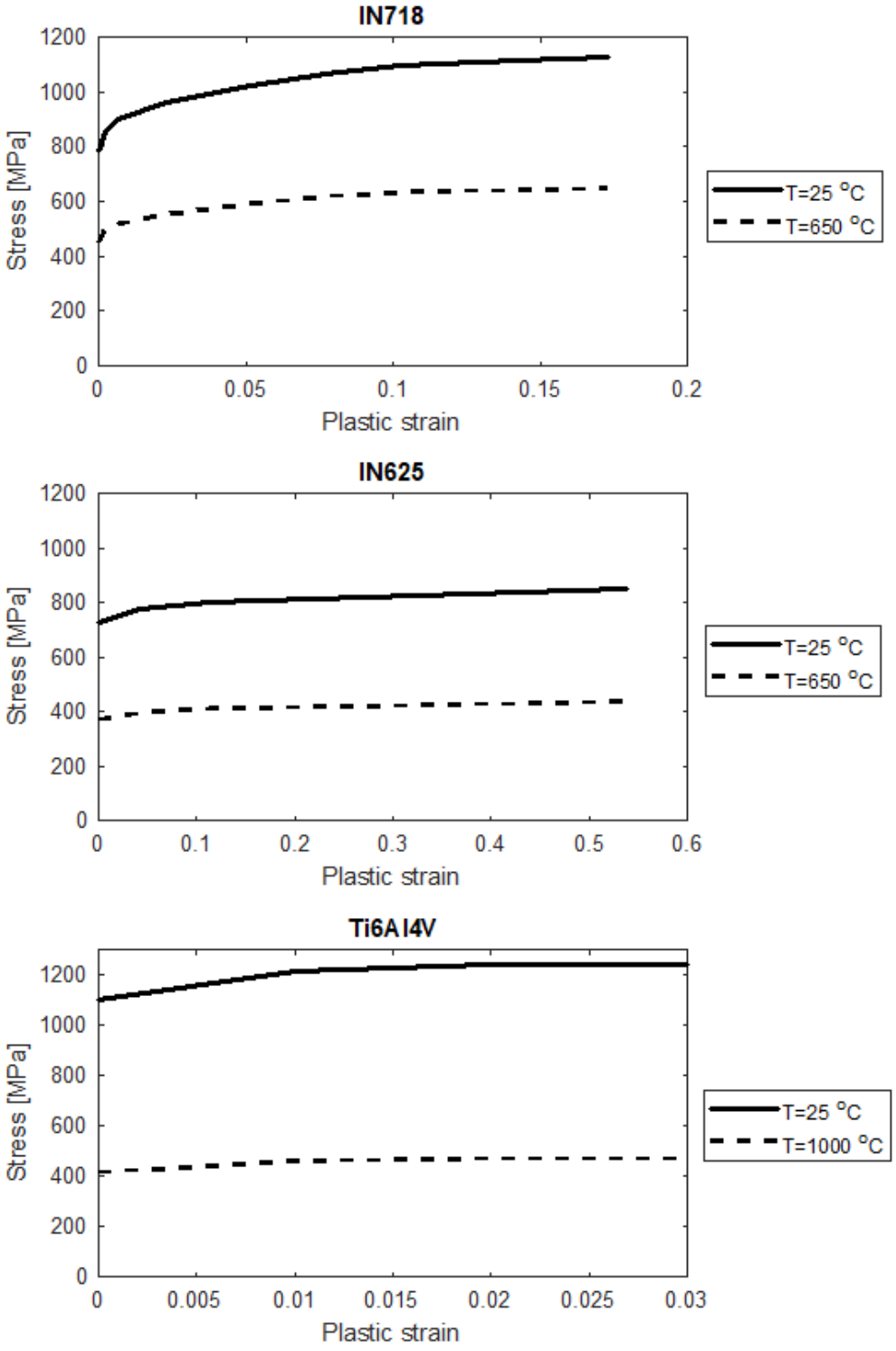


**Figure 3. 9.** Stress strain curves for IN718, IN625, and Ti6Al4V

It was assumed that the material properties reference temperature is the melting temperature. In other words, when the layer is heated to the melting temperature, the material does not thermally expand. However, the layer shrinkage during the cooling steps results in thermal stresses that are the main cause of the induced residual stresses and distortions. The thermal strain caused by the shrinkage can be calculated as

$$\varepsilon_{th} = \alpha(T)(T - T_{ref}) \qquad \text{Eq. 3. 2}$$

where $\alpha(T)$ is the temperature dependent thermal expansion coefficient, $T$ is the applied temperature, and $T_{ref}$ is the material reference temperature. Also, it is mentionable that the material properties may change as the process parameters change or from one location to another based on the part features. These effects will be investigated in future studies.

## 3.5. 3D Thermomechanical Modeling: Model Validation

### *3.5.1. NIST Cantilever*

The geometrical details for the IN625 NIST AMB2018-01 are shown in Figure 3.10. The predictions of the thermomechanical modeling of the cantilever are validated by the residual elastic strain and stresses and distortion solution which were published on NIST website [76] and also available in [64]. For model validation purposes, the problem was initially run at N=10 and C=7 assuming layer thickness of 0.25 mm, where the total number of mechanical equivalent layers was 50 layers.

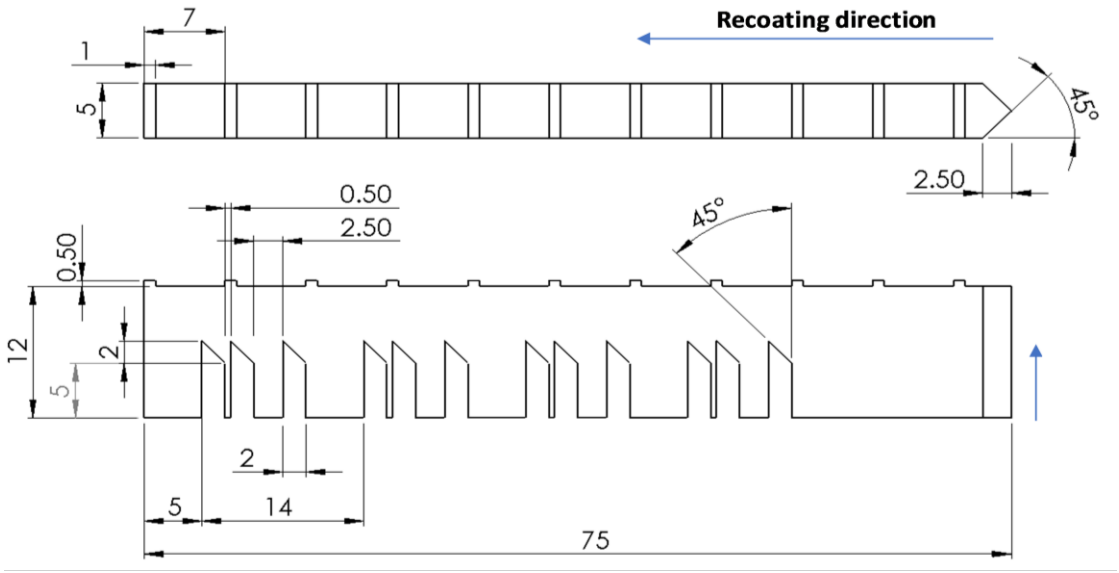


**Figure 3. 10.** Top and elevation views of the NIST AMB2018-01 bridge structure geometry. (Source: NIST [77])

The elastic residual strain results before and after cutting supports at the cantilever center plane are shown in Figure 3.11. The residual elastic strains in x direction before cutting the supports are tensile at the overhangs where the maximum value is at the top of the cantilever, Figure 3.11 (a). The residual elastic strains in z direction (build direction) were mainly highly compressive close to the build plate and moderately compressive at the overhangs, but highly tensile close to the edges, Figure 3.11 (b). These predicted results can find a good agreement with the experimentally measured strains by X-ray diffraction in [64], previous finite element predictions results for this cantilever in [78], and also previous cantilever studies in [55, 59]. Cutting supports was simulated by deactivating the base elements under the support structure. It is obvious that cutting the support structure contributed to reducing the residual elastic x strains at the overhangs, except for the points close to the edges and above the cantilever base. The residual elastic z strains, however,

were not significantly affected by cutting the supports except for the points close to the edges.

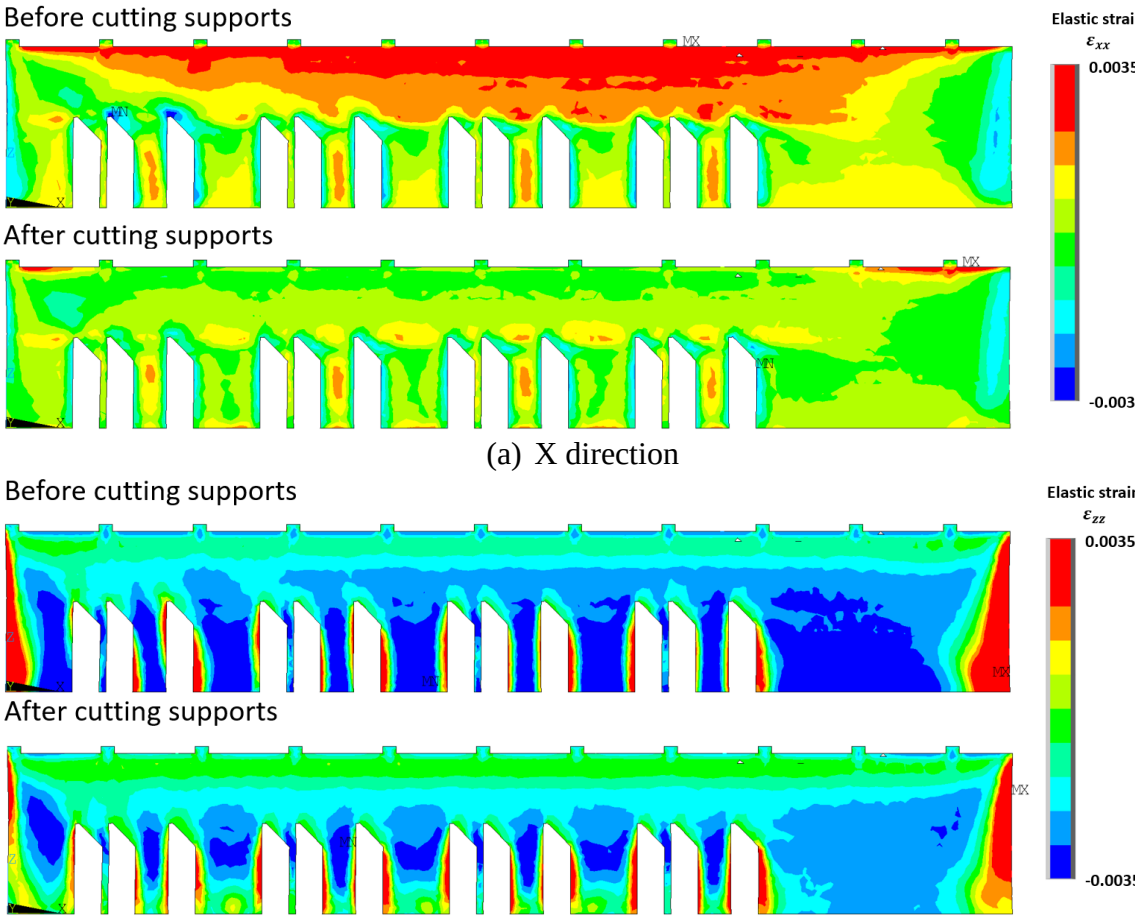


(a) X direction

(b) Z direction

**Figure 3. 11.** Elastic strains before and after cutting supports (N=10)

The detailed elastic strain history during the process simulation and supports cutting is shown in Figure 3.12. Eighteen points at three different z levels were chosen to demonstrate the elastic strain evolution, Figure 3.12 a. Firstly, the fluctuations in the elastic strain results during the solution due to the heating and cooling cycles can be seen in Figure 3.12 b, c and d. The elastic strains at all points are affected by the build of the consecutive layers, except for the last two layers as they represent the small displacement measurement tabs and do not influence results. Secondly, as mentioned earlier, before cutting the supports, the elastic strains stabilities at high tensile values in x direction, and compressive in z direction, except for points close to the edges that exhibit different behavior (A1, B1, C1, A6, B6, and C6). This spatial correlation was previously shown in Figure 3.11. After cutting the supports, a sudden decrease in the elastic strains takes place. Thirdly, elastic strains history does not show significant errors caused by the remeshing steps. The smooth evolution of elastic strains also indicates that high remapping accuracy is evident.

The remapping accuracy is further demonstrated by evaluating the residual elastic strains in x direction just before and after remapping, and after solving 40 layers, Figure 3.13. Although high *C* value was used, high remapping accuracy even at the high strain gradient regions is obvious. The reasons behind this accuracy is the efficient and accurate remapping algorithm that ANSYS has, and the use of high order elements with four integration points at which solution is mapped.

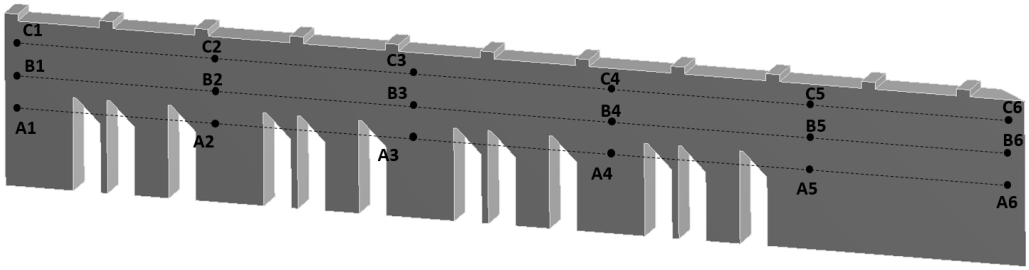


(a) Measurement location

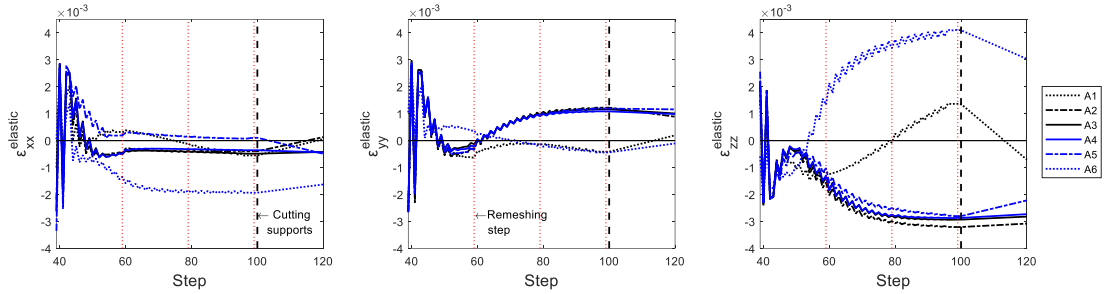


(b) Points A1 to A6 (z=5 mm)

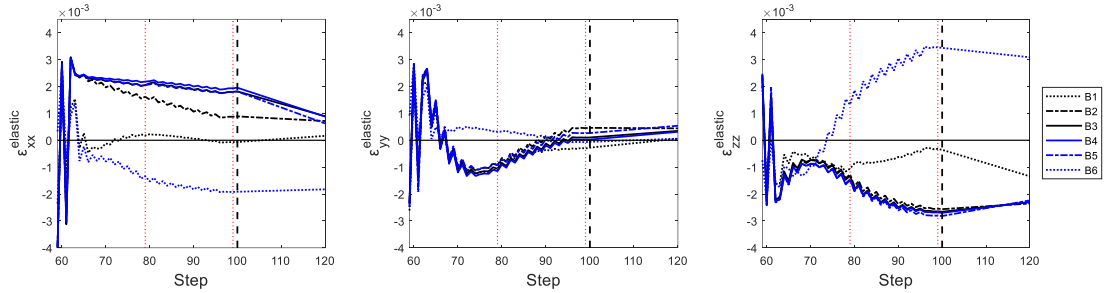


(c) Points B1 to B6 (z=7.5 mm)

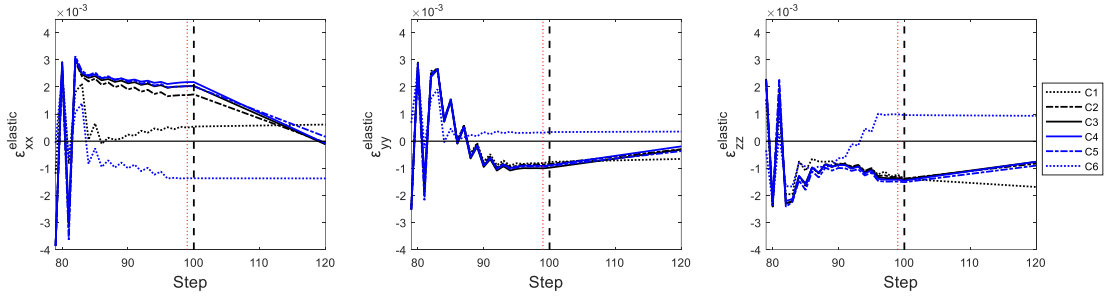


(d) Points C1 to C6 (z=10 mm)

**Figure 3. 12.** Elastic and total strain history at multiple locations

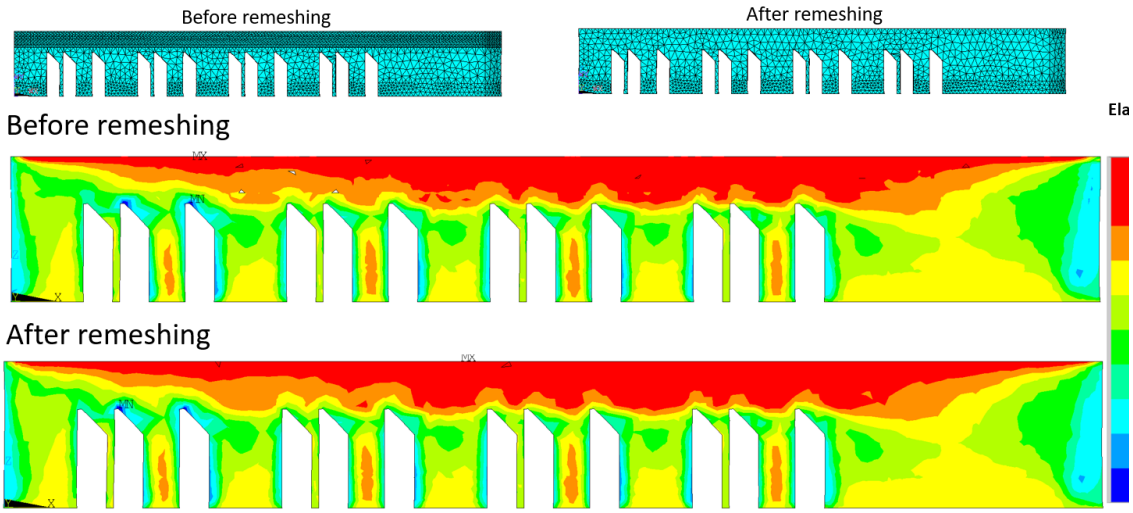


**Figure 3. 13.** Elastic strains distribution before and after remapping (C=3.5)

The predicted residual stresses in x direction before cutting supports find good agreement with the experimentally measured using the contour method at one of the cantilever legs [64], Figure 3.14. The stresses are compressive near the build plate and leg center. However, residual stresses turn tensile at the overhang reaching its maximum value at the top.

The release of the elastic strains by cutting supports was the main reason for parts' distortion through the spring back effect, Figure 3.11. The distorted NIST cantilever is shown in Figure 3.15, where the predicted maximum vertical displacement at the measurement tab was 0.9433 mm. The predicted maximum displacement is underestimated compared to the reported experimentally measured value of 1.276 mm. This deviation could be due to the simplifications of the heat source model and the assumption of uniform material properties throughout the cantilever. However, the predicted distortion result can

be further improved by utilizing the inherent strain approach as in [59] or scaling the yield strength value up to allow more tensile elastic strains. This is, however, out of the scope of this paper as this solution was also obtained without adaptive remeshing.

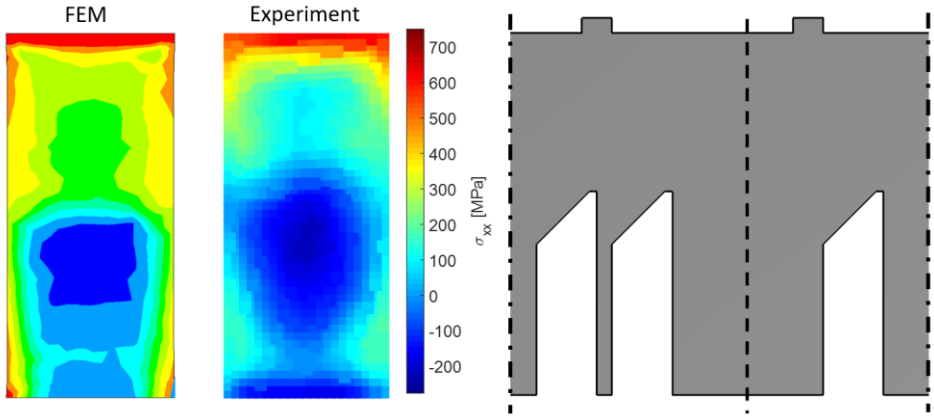


**Figure 3. 14.** X stresses at X=31mm

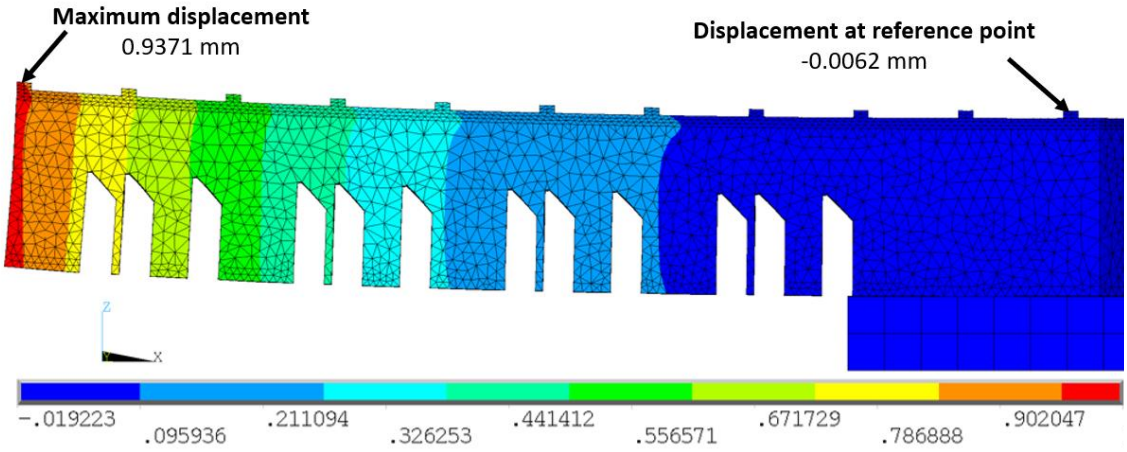


**Figure 3. 15.** Displacement results [79]

### *3.5.2. Bridge Structure*

The case of bridge structure was also investigated. The dimensions of the bridge structure are shown in Figure 3.16. The build of the bridge structure was simulated considering a layer thickness of 0.25 mm, where the total number of layers was 32 layers. Like the cantilever case, high tensile residual elastic strains in x directions were observed at the top surface, Figure 3.17 a. After the left leg was released by deactivating the build plate elements under the bridge left leg, the tensile elastic residual strains were released, Figure 3.17 b, resulting in the bridge structure deformation. These observations find an agreement with the residual stresses results predicted finite element modeling in [45]. The final deformation after the release from the build plate is shown in Figure 3.18. This deformation behavior finds an agreement with the experimental solution for the same structure in [80] and finite element predictions in [45]. The curling angle in this model, which was found to be 4.23$^{o}$. This value is overestimated by 50% when compared to the experimentally measured value of 2.8$^{o}$.

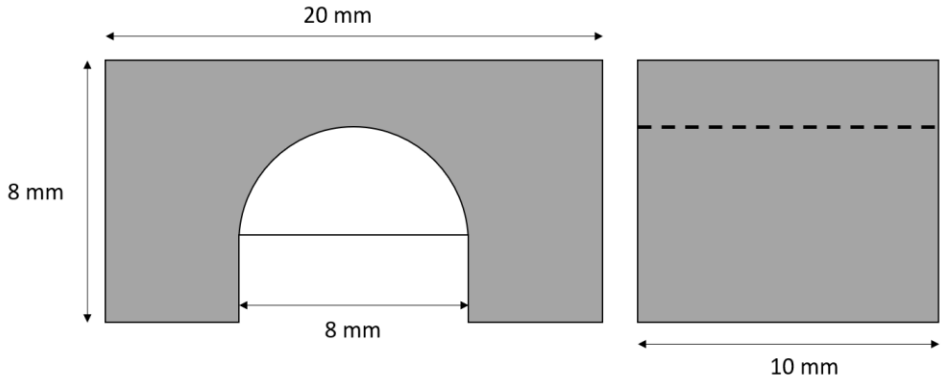


**Figure 3. 16.** Bridge structure dimensions

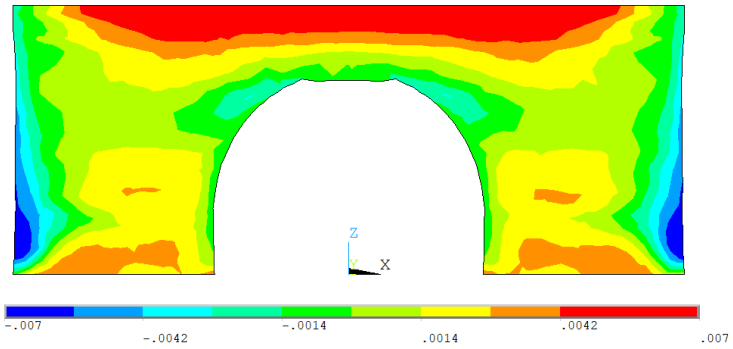


(a) Before cutting left leg

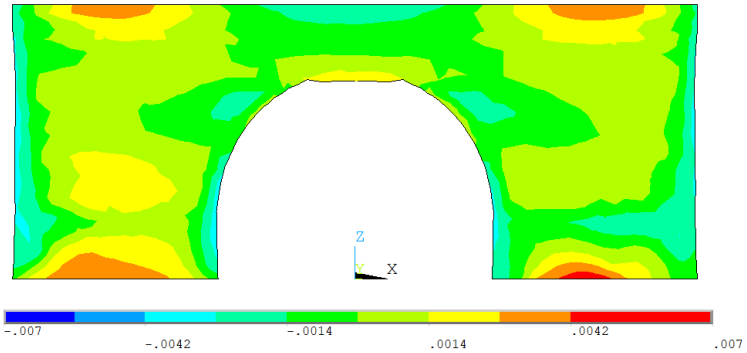


(b) After cutting left leg

**Figure 3. 17.** Residual elastic strain in x direction before and after removing from build plate.

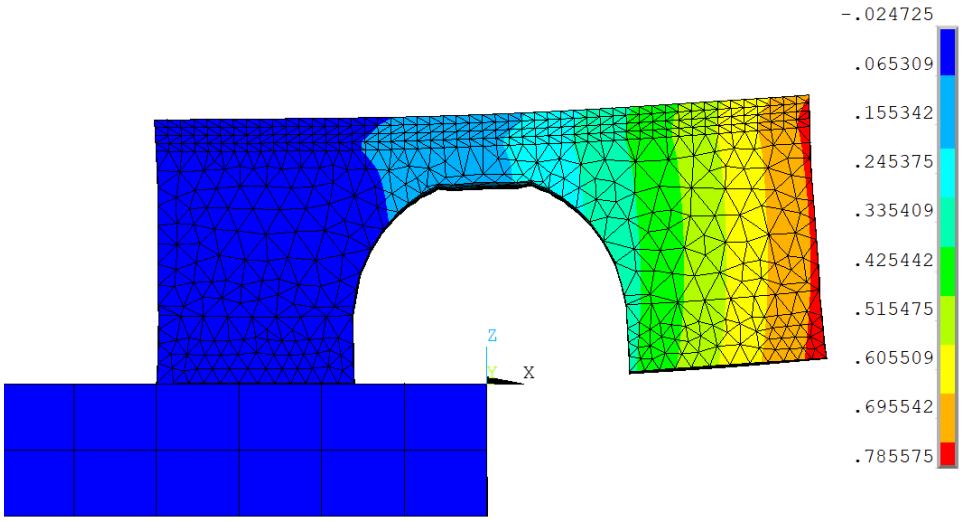

(a) Vertical displacement (mm)

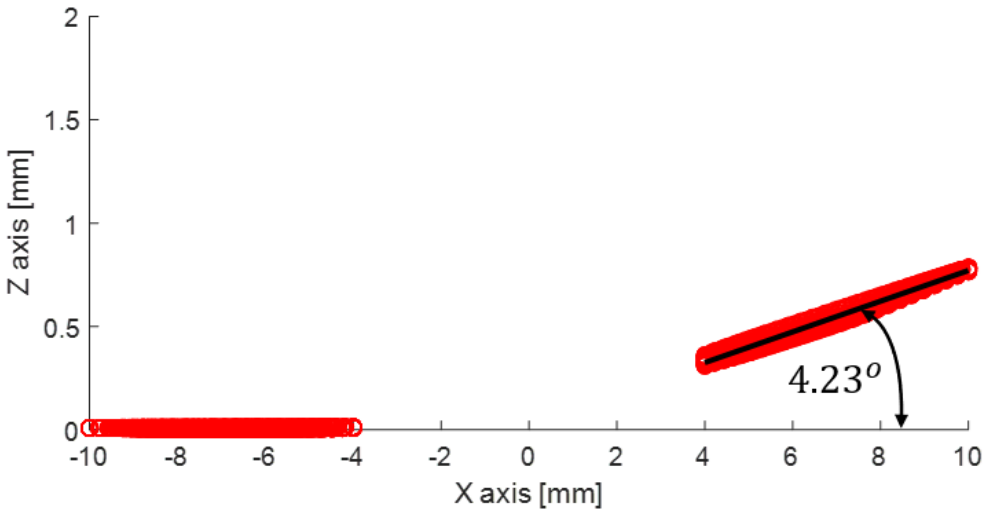


(b) Curling angle calculated from bridge bottom nodes

**Figure 3. 18.** Bridge structure deformation after cutting the bridge left leg

### *3.5.3. Canonical Part*

The build of the square canonical part was simulated assuming a layer thickness of 0.5 mm, where the total number of layers is 50. Figure 3.19 shows the predicted elastic strains for the square canonical models with and without adaptive remeshing after the build is complete. The comparisons show some differences in the elastic x strain distribution at the center of each side. This can be due to mesh coarsening at thin walls, Figure 3.20. Although the high-order element adopted in the analysis can capture the strain gradient, using one element to represent thin walls might be associated with some mapping errors and different history. Thus, a compromise between accuracy and computational time must be achieved.

For parts including thin features like this part, distortions take place during the process. The current ANSYS features do not map the displacement solution after remeshing, and the final displacement solution could be obtained by comparing the final deformed mesh to the initial mesh. Thus, final displacement values were calculated only at final nodes location. The horizontal displacement at the square canonical face center is shown in Figure 3.21. This displacement behavior finds an agreement with the experimental solution in [36], though the maximum displacement value is underestimated by 25%. In addition, the predicted distortions show slight differences compared to the case without adaptive remeshing. In other words, the coarse mesh at the thin walls did not significantly affect solution accuracy. As mentioned earlier, predictions accuracy can always be improved by changing the material properties as microstructure and mechanical properties for thin walls could be different.

A comparison between the proposed approach and the NetFabb adaptive remeshing approach discussed in [36] is shown in Table 3.2. The proposed approach could help achieving reduced number of nodes and elements. With using only one core, the average computational time per step using the current approach is 1.68 min/step, which is four times higher than that reported by NetFabb when using 26 cores. The current limitation of the proposed approach is that the ANSYS rezoning feature which is responsible for remapping does not support distributed computing mode.

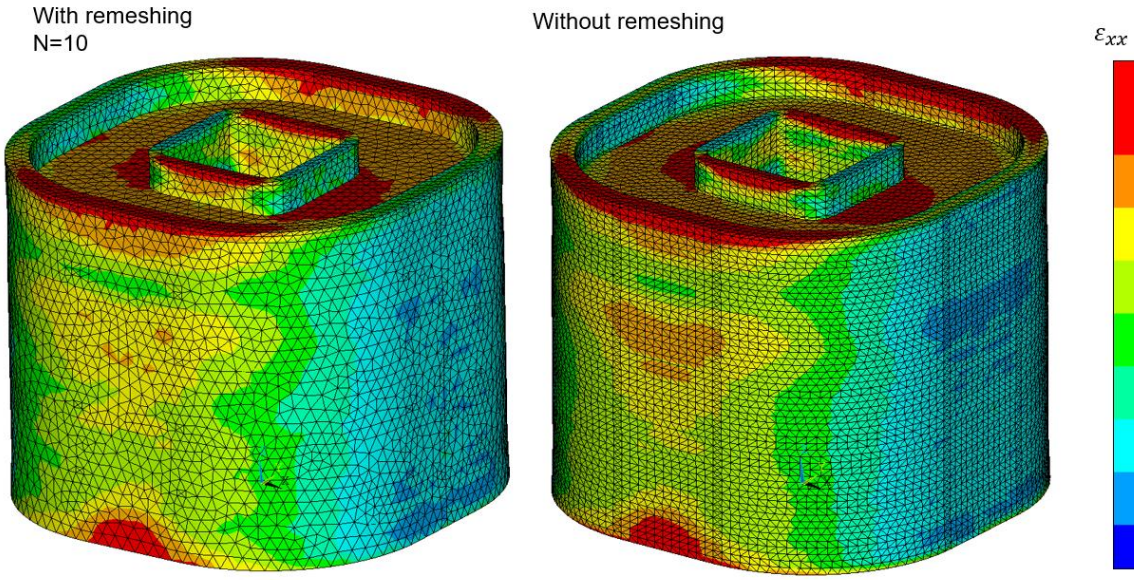


**Figure 3. 19.** Elastic strain in x direction wish and without adaptive remeshing

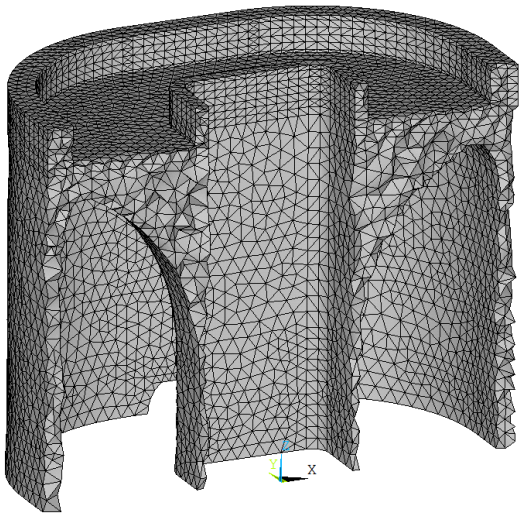


**Figure 3. 20.** Final mesh for canonical part (N=9)

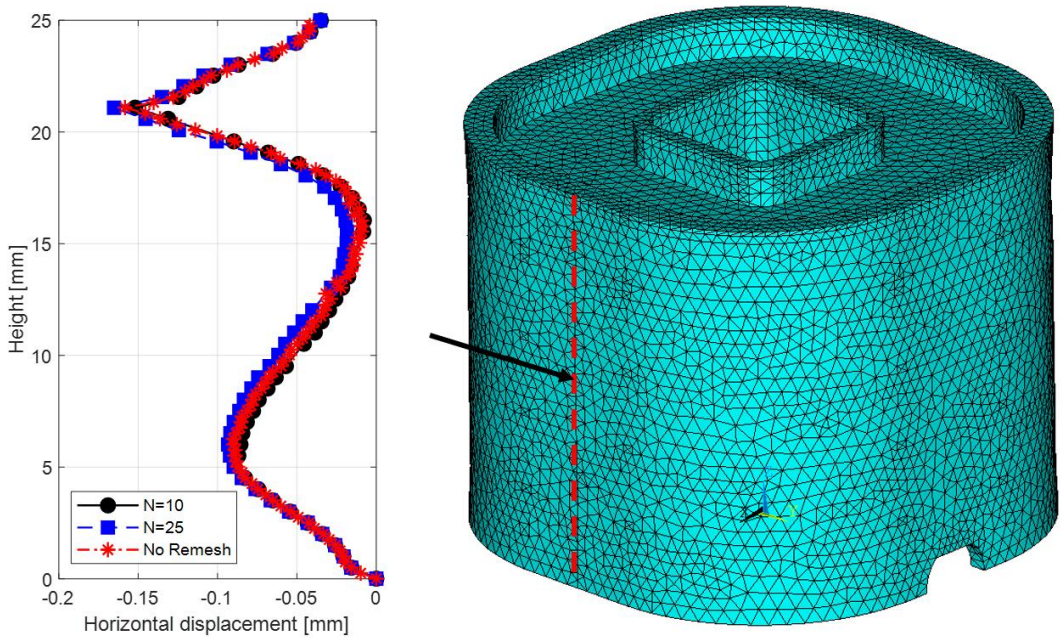


**Figure 3. 21.** Distortions for the canonical part

Table 3. 2. Comparison between the proposed approach and NetFabb [36] for the square canonical part.

| | | NetFabb (Gouge et al. [36]) | Proposed approach |
|---|---|---|---|
| Model | Number of nodes (Last layer) | 357,162 (4 adaptivity levels) | 152,604 (N=10) |
| | Number of elements (Last layer) | 194,066 | 91,764 (N=10) |
| | Number of structural simulation steps | 32 | 100 |
| Solution | Maximum displacement | 0.19 mm (13% error) | 0.165 mm (25% error) |
| Computational resources | Number of cores | 24 (2.2 GHz) | 1 (3.6 GHz) |
| | RAM (Available, not used) | 192 GB | 24 GB (only 7 GB were used) |
| | Total computational time | 13 min 49 s (2.6% of build time) | 2.8 hr (32% of build time) |
| | Time per step | 0.43 min | 1.68 min |

## *3.6. Effect of Adaptive Remeshing*

### 3.6.1. Effect of adaptive remeshing on computational efficiency

The effect of the number of layers between remeshing (*N)* on the computational time for the NIST cantilever with C=1.75 is shown in Figure 3.22. The total computational time includes the solver time (spent on solving the thermal and structural problems), remeshing time, and remapping time. Overall, the total computational time reduction is significant and could reach up to 50% when the proposed adaptive remeshing framework is utilized. In addition, the *N* value affects the computational efficiency. When *N* is small (*N*=5), less time was spent in solving but more time was spent in remeshing and remapping. As *N* value increases, the total computational time is being decreased until reaching the minimum at an optimal *N* value, after which the computational time starts to increase again. The optimal *N* for the NIST cantilever with assumed layer thickness of 0.25 mm and C=1.75 was found to be 9 layers. This optimal *N* value will change from one part to another and also based on the mesh configuration. This can be explained further by Figures 3.23 and 3.24 where the RAM usage and number of nodes throughout the simulation steps are shown. The reduction in RAM usage and number of nodes is positively proportional to the *N* value. A reduction of 80% in RAM usage and 50% in the number of nodes could be achieved with *N*=5. Thus, low *N* values can always be the solution when the computational resources are limited.

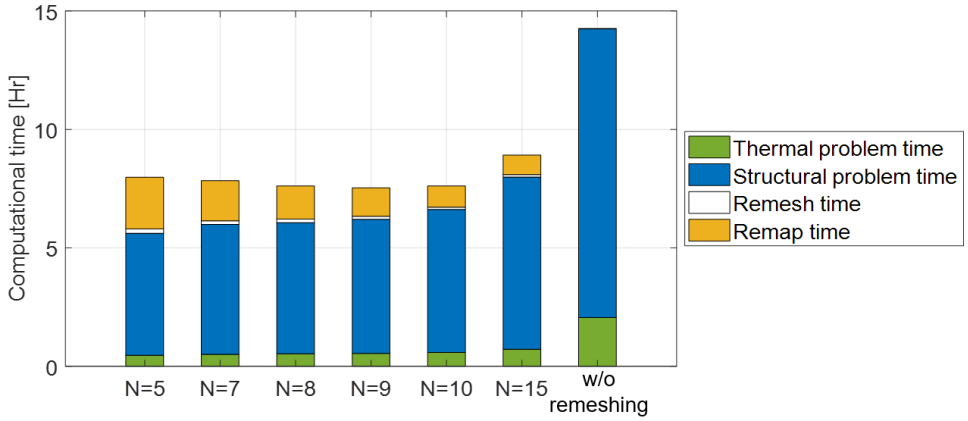


**Figure 3. 22.** Effect of number of layers per task on computational time for NIST Cantilever (C=1.75)

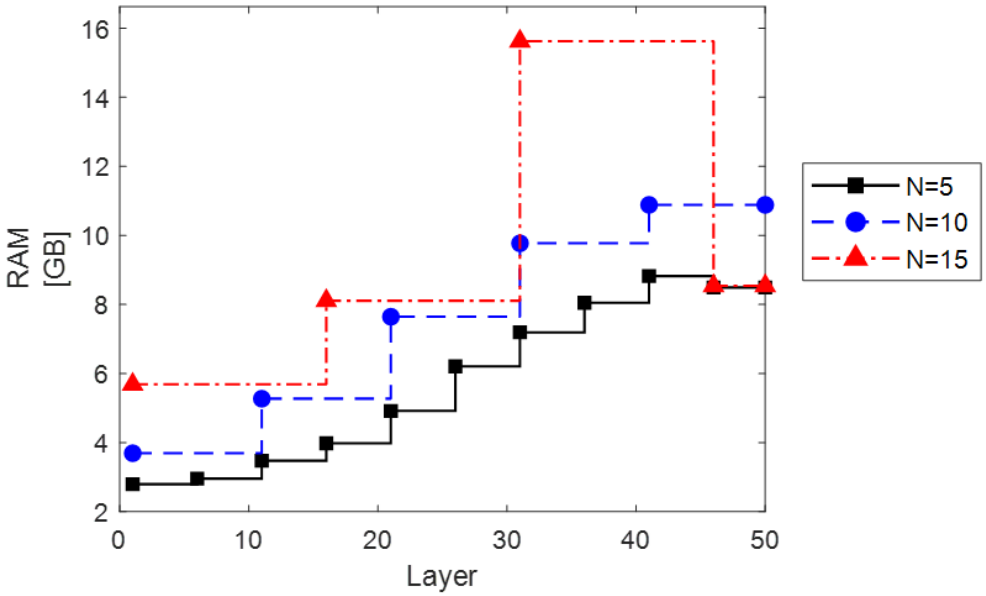


**Figure 3. 23.** Effect of the number of layers per task on RAM

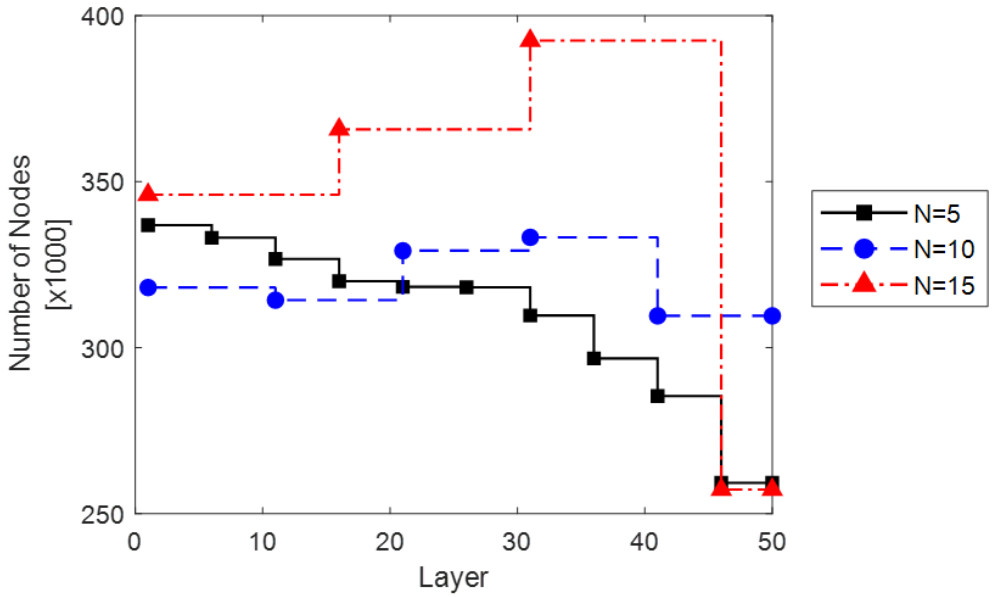


**Figure 3. 24.** Effect of the number of layers per task on RAM number of nodes during solution

The effect of the mesh coarsening level (*C*) on the computational time and solution was also investigated. Two *C* levels were used; 1.75 and 3.5. The effect of *C* value on the total computational time at different *N* values is shown in Figure 3.25. As shown, a higher reduction (up to 70%) in the computational time could be achieved at higher mesh coarsening value. This could be justified by the reduced number of nodes and RAM usage compared to those with low *C* values, Figures 3.26 and 3.27.

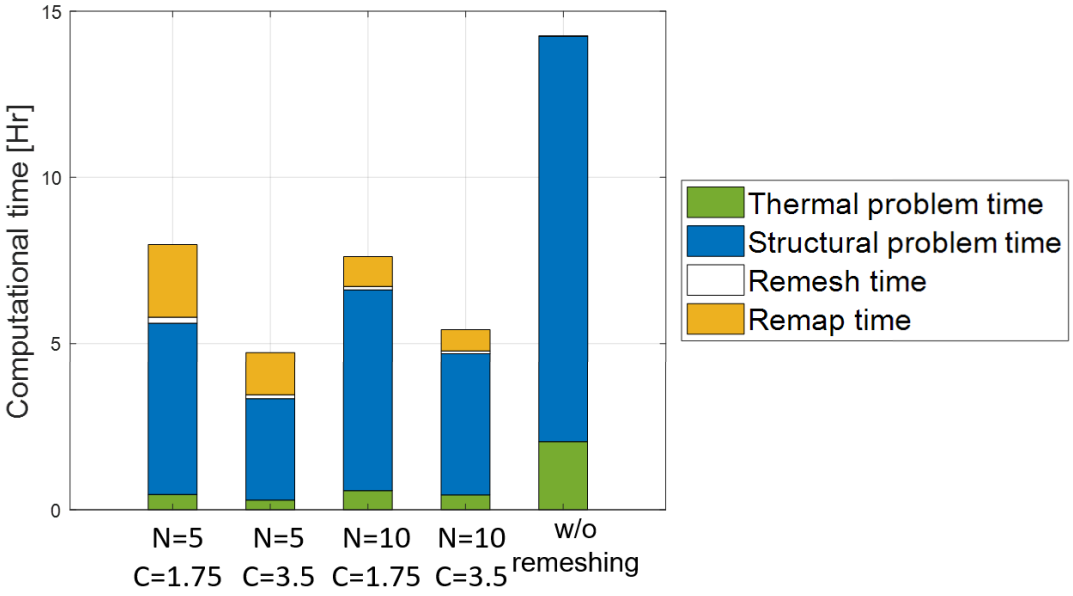


**Figure 3. 25.** Effect of coarsening level on the total computational time for different N values

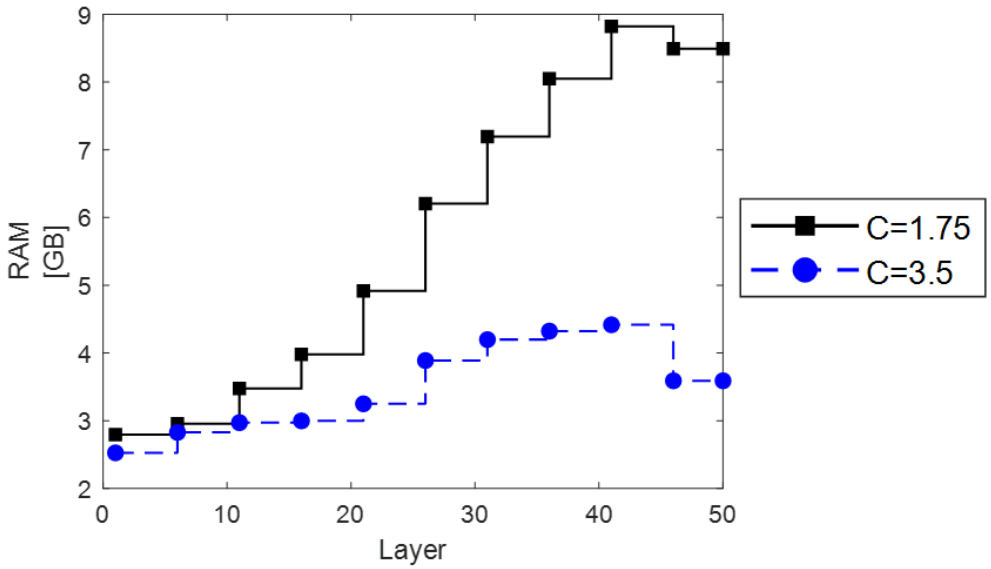


**Figure 3. 26.** Effect of coarsening level on the RAM utilization at N=5

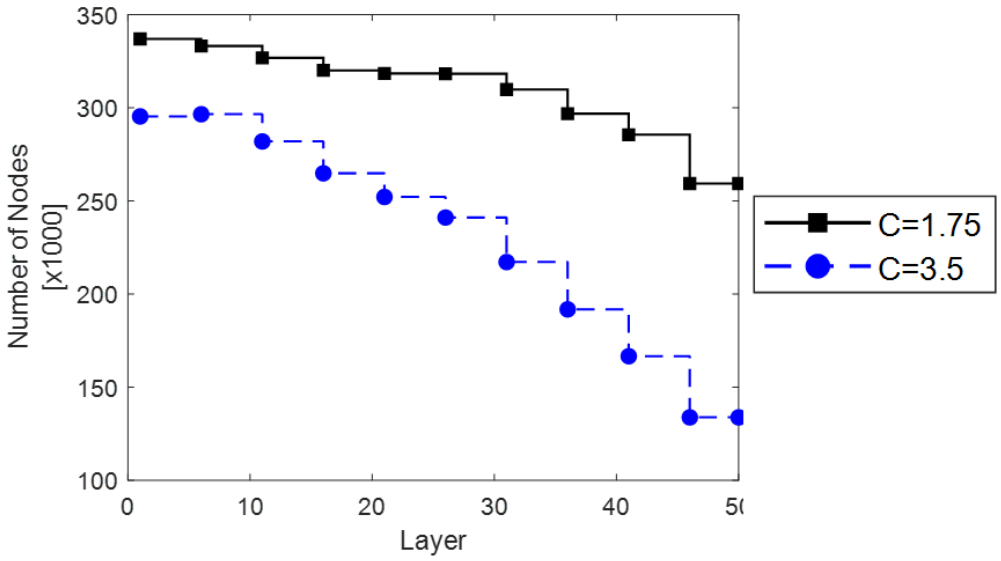


**Figure 3. 27.** Effect of coarsening level on the number of nodes at N=5

### *3.6.2. Effect of adaptive remeshing on solution*

The effect of *N* and *C* on the results was also investigated. As previously mentioned, high *C* values can, however, result in significant loss in accuracy. The new mesh must be acceptable for accurate stresses, strains, and temperature remapping. If the mesh size is large, the high strain and temperature gradients near edges and features cannot be well captured within few elements, and solution accuracy will be questionable. The effect of *C* value on the residual elastic stain results is shown in Figure 3.28. It can be seen, even with some slight differences, elastic strain results are almost identical. The solution with C=1.75 could keep the highlighted details that could not captured with C=3.5. Solution differences, however, would be much larger at higher *C* values. Thus, depending on parts' feature, an appropriate *C* values must be chosen. Low *C* values are more appropriate for parts that include complex features and thin walls.

The adaptive remeshing parameters effect on solution are further demonstrated by the final displacement solution. Figures 3.29 and 3.30 show the differences between the predicted cantilever distortions and experimental results. It is obvious all predictions are underestimated from the experimental solution, and the deviation within the predicted results at different N and C combinations can hardly be observed. The solution, however, may significantly change at higher *C* values.

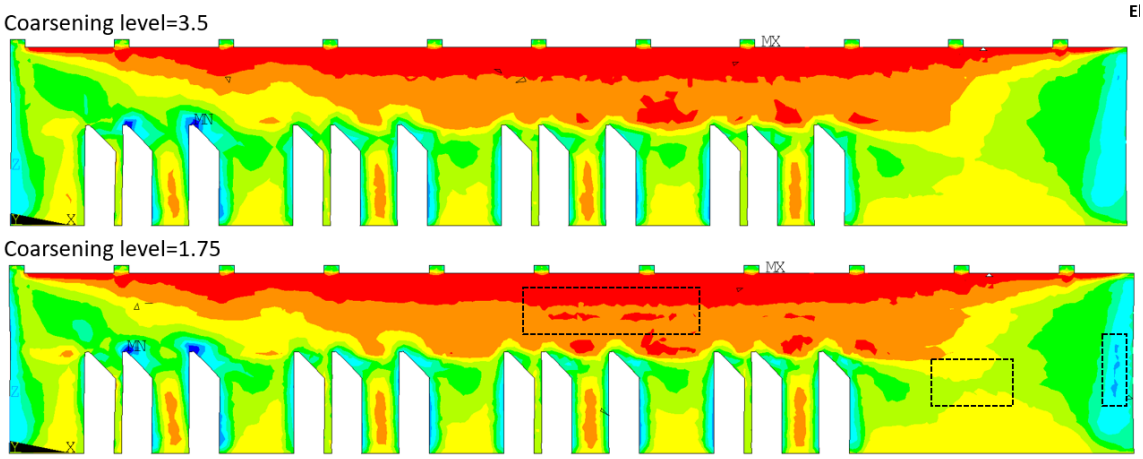


**Figure 3. 28.** Effect of coarsening level on final elastic strains in x direction before cutting supports.

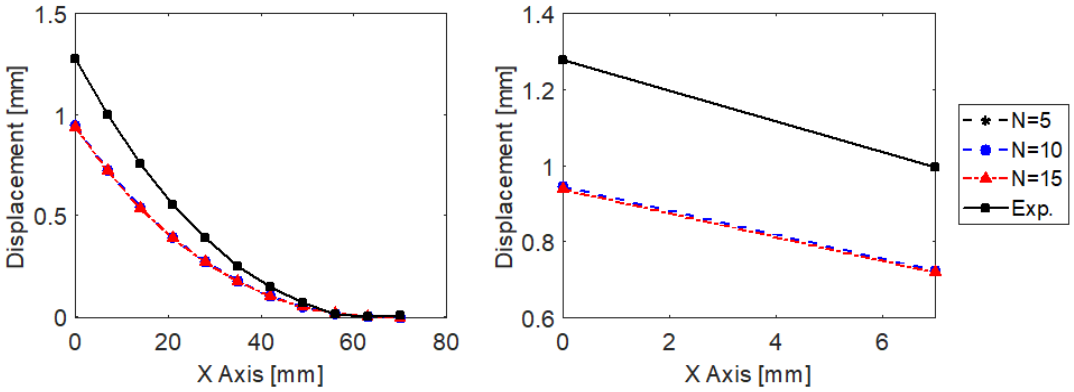


**Figure 3. 29.** Displacement results at different levels of N compared to the experimental measurement in [64]

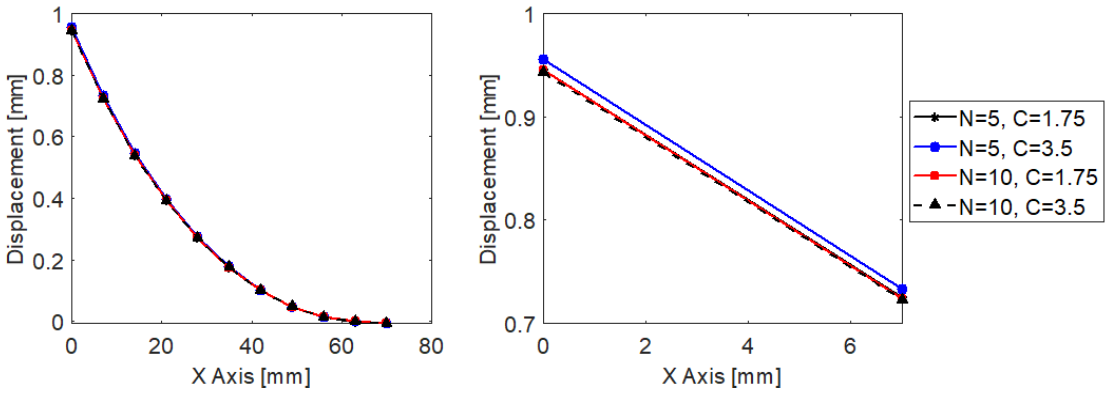


**Figure 3. 30.** Displacement results at different levels of N and C

# 4. Model validation framework for the LPBF process

## *4.1. Literature Review*

The accuracy of the computational models depends on the included physics of the process. In Finite element based thermal models, in addition to the several assumptions being made, the melt pool fluid dynamics are ignored. These assumptions may include the material behavior modeling, process parameters value assumptions, and heat source modeling. Process parameters are associated with uncertainties since a precise measurement of each parameters is not always possible. In addition, the process parameters such as laser power, scan speed, and even powder particles randomness cause fluctuations that reduce the predictive model capability.

The laser power is a critical controllable parameter that greatly affects the final part quality. During the process the laser power may change due to a drift in the galvanometer control system and heating of optics causing loss and fluctuation of laser power that result in nonuniform melt pool dimensions. It had been reported that experimentally measured power value is 14% less than machine input value [43]. The value of powder layer thickness, one of the main controlled parameters, depends on the motion and position of the build platform and recoater arm. The effective layer thickness is different from the nominal value due to the uncertainties related to the build platform motion, powder bed density, and the motion of recoater arm [44].

The heat source model is also associated with some assumptions that have a great effect on the predictive model accuracy, such as absorptivity, and laser beam diameter. Absorptivity mainly depends on the powder particles shape, size, and distribution. Previous finite element simulations were always associated with uncertain absorptivity value, where is it assumed that the Ti-6Al-4V powder particles absorptivity is like bulk material [32], 0.35 in [81], or 0.7 in [28]. In addition, it was also found that absorptivity is temperature dependent [23]. Direct measurement of absorptivity during the experiments is difficult. Another factor included in the heat source model is the laser beam diameter. Although laser beam diameter can be measured experimentally, it changes during the process due to the fact when the lens slightly deforms as they heat up. This causes a change of the laser beam diameter during the process. Therefore, both absorptivity and beam diameter add to the predictive model uncertain parameters.

### *4.2. Research Motivation*

The author's objective in this chapter is to develop a general framework that can be used for calibration and validation in the application of LPBF considering limited experimental data. A systematical calibration and validation framework for the LPBF process based on multi-fidelity models (i.e., the finite element models and meta-models) and limited experimental data is needed. The objective is to validate the highly efficient meta-models so that uncertainty quantification of the LPBF process performance of interest (e.g., melt pool, residual stress, porosity, etc.) can be conducted effectively and, furthermore, reliability and quality analysis based on the meta-model could be trustworthy. Compared with the pure data-driven approach using machine learning methods and abundant

experimental data, the proposed method requires only limited experimental data to build an accurate meta-model because of the incorporation of the physics knowledge from the finite element model. Compared with the physics-based finite element modeling, the proposed method dramatically improves the model prediction efficiency using the machine learning methods. In addition, the framework is to be utilized to calibrate the parameters associated with high uncertainty such as the absorptivity.

### *4.3. Calibration and validation framework for the LPBF process*

Development of FEM for the LPBF process is a critical step in the proposed calibration and validation framework because it provides a solid foundation for predicting different parts thermal behaviors with various parameter settings. Data-driven modeling based on experiments using different DOE techniques, on the other hand, requires many experiments covering the whole operation domain, hence is very expensive and time consuming. In addition, such training model only works for one part and must be trained again and again for different parts. With physics-based modeling, i.e., the FEM of the LPBF process, thermal behaviors of any new part structure can be predicted. If the model prediction can be validated with the aid of a few experiments, the model can serve as a design tool to identify the optimal process parameters for the LPBF process or could be used for online quality control of the parts. The technical challenge is that the FEM of the LPBF process is still computational expensive which make it not suitable for design purpose. This section hence proposes a multi-fidelity modeling approach for the LPBF process with the aid of a few experiment data. Basically, a meta-model, with high computational efficiency, will be constructed based on the FEM, then this meta-model will be validated based on limited

experiment data. Due to the integration of the meta-model with the physics-based FEM, such meta-model can be easily constructed for any new part structure without requiring many new experiment data.

### 4.3.1. Overall framework

The proposed overall calibration and validation framework is shown in Figure 4.7. Based on the physics-based LPBF model, melt pool prediction, e.g., width and depth, can be obtained at any set of process parameters. For the purpose of building a meta-model, DOE technique can be employed to run the physical model at predetermined parameter settings which may include laser power, spot diameter, scanning speed, and absorptivity. To build a meta-model with a given set of inputs and outputs, any machine learning models can be employed. This paper employs the Gaussian process (GP) regression model due to its proved accuracy for many engineering applications [82]–[84]. With such a meta-model, the important step is to improve its accuracy while maintaining the high efficiency based on available experiment data. Researches in model calibration and validation [51–55] can thus be employed in this study with the main purpose of characterizing model bias of the meta-model and identifying the inherent randomness of some model parameters, e.g., absorptivity and spot diameter. Integrating the meta-model with its bias function and calibrated model parameters, a corrected meta-model can be achieved to further validate its accuracy with the aid of validation experiment data. If there is no evidence that the corrected meta-model is inaccurate, the calibration and validation process is completed, and the corrected model can be used for various purposes. Otherwise, the process should

be updated by adding some new experiment data for bias characterization and parameter uncertainty quantification.

### 4.3.2. Problem formulation

Let $Y_m(\bullet)$ indicates the meta-model prediction of the melt pool, e.g., melt pool width or depth. Model parameters could include laser power, scanning speed, spot diameter, powder absorptivity, etc. Among them, some parameters, such as laser power and scanning speed, are controllable, measurable, and their randomness may be ignored. Other parameters, such as spot diameter and powder absorptivity, are noncontrollable and contain inherent randomness during the process, and their realizations in real experiment cannot be easily measured. If $x$ and $\theta$ are used to denote the controllable and noncontrollable parameters, respectively, meta-model prediction is represented as $Y_m(\mathbf{x}, \boldsymbol{\theta})$, where the bolded symbol means a set of parameters. For both physics-based LPBF model and the learned meta-model, model prediction demands the explicit input of $\mathbf{x}$ and $\boldsymbol{\theta}$. In addition, it is assumed that the randomness of $\boldsymbol{\theta}$ does not change when $\mathbf{x}$ changes.

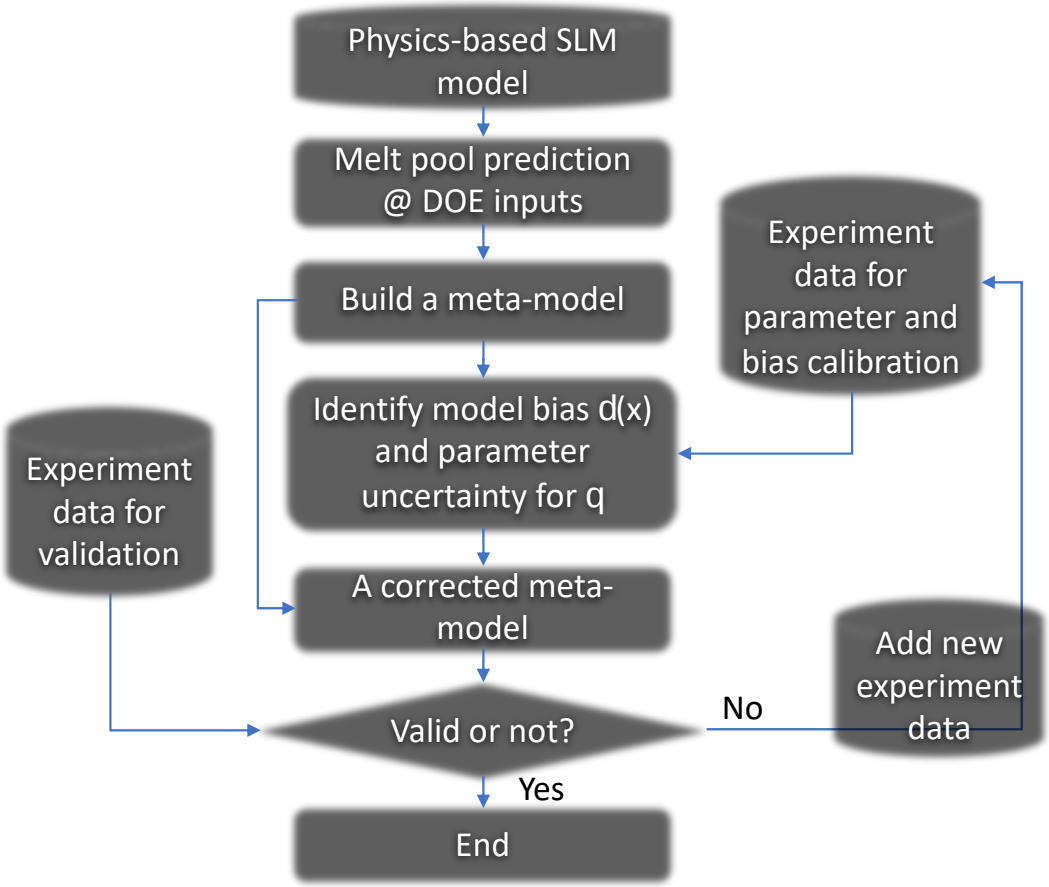


**Figure 4. 1.** Proposed calibration and validation framework for the LPBF process based on multi-fidelity models

Let $Y_t(\bullet)$ stands for the melt poor measurement in experiment. Controllable parameters, i.e., **x,** are known during the experiment, but the realization of uncontrollable parameter $\boldsymbol{\theta}$ is unknown. Hence, the melt pool measurement from experiment can be represented as $Y_t(\mathbf{x}, \boldsymbol{\theta}^*)$, where $\boldsymbol{\theta}^*$ indicates the realization of the parameter $\boldsymbol{\theta}$ during the measurement. The challenge is that the true value of $\boldsymbol{\theta}^*$ is unknown in experiment. As such, it is impossible to obtain one unique meta-model prediction under the exact same condition as experiments. Acknowledging that the meta-model has inherent model inadequacy for representing the real physical system and assuming that the difference between meta-model prediction and

experiment can be modeled by a bias function $\delta(\bullet)$, then the functional form can be formulated with respect to the controllable parameter, i.e., $\delta(\mathbf{x})$, but with inherent uncertainty due to the unknown parameter $\boldsymbol{\theta}$. It is worth noting that $\boldsymbol{\theta}$ is not included in the bias function because it is not measurable in experiment and hence an explicit bias function with respect to $\boldsymbol{\theta}$ cannot be obtained [89].

As a summary, Eq. 4.1 formulates the relationship for the meta-model prediction, bias function, and the experiment measurement, by assuming that experiment and measurement error can be ignored.

$$Y_m(\mathbf{x}, \boldsymbol{\theta}) + \delta(\mathbf{x}) = Y_t(\mathbf{x}, \boldsymbol{\theta}^*) \qquad \text{Eq. 4. 1}$$

The objective in this section is to characterize the bias function $\delta(\mathbf{x})$ and the randomness of parameter $\boldsymbol{\theta}$ such that any experiment measurement at any new operation conditions, i.e., right side of Eq. 4.1, can be accurately predicted from the corrected meta-model, i.e., left side of Eq. 4.1. Due to limited number of experiment data, e.g., only one melt pool measurement at given $\mathbf{x}$, accurate prediction from the corrected meta-model means that there would be no statistical evidence to reject that the corrected meta-model is valid.

### 4.3.3. Bias calibration

To determine the bias function $\delta(\mathbf{x})$ and the randomness of parameter $\boldsymbol{\theta}$, the calibration framework proposed in [90] is followed with some modifications. The first step is to determine the bias function $\delta(\mathbf{x})$ at different controllable parameter $\mathbf{x}$, given some limited experiment data and an assumed prior distribution of $\boldsymbol{\theta}$. The second step is to calibrate the randomness of $\boldsymbol{\theta}$ given the predetermined bias function $\delta(\mathbf{x})$. Such decoupling process was

employed in [90] and is reasonable because the randomness of $\boldsymbol{\theta}$ mainly changes the uncertainty bound at the left side of Eq. 4.1 and the bias function δ(x) mainly affects the bias magnitude at different controllable settings. In this paper, a set of bias training data can be obtained as

$$\delta(\mathbf{x}) = \mathbb{E}[Y_t(\mathbf{x}, \boldsymbol{\theta}^*)] - \mathbb{E}[Y_m(\mathbf{x}, \boldsymbol{\theta})] \qquad \text{Eq. 4. 2}$$

where $\mathbb{E}[*]$ is the expectation of a function under given randomness of parameter $\boldsymbol{\theta}$. If there were enough experiment measurement at different controllable parameter $\mathbf{x}$, the realizations of $\boldsymbol{\theta}^*$ would truly represent the distribution of $\boldsymbol{\theta}$. As such, the expectation would be certain and there is no epistemic uncertainty for the bias function δ($\mathbf{x}$). In reality, the number of measurements is always limited, e.g., only one measurement at given $\mathbf{x}$. Hence, epistemic uncertainty would be presented when constructing the bias function after obtaining a set of training data using Eq. 4.2. For bias prediction at new parameter $\mathbf{x}_*$, the GP regression model is employed which is formulated as

$$\delta(\mathbf{x}_*) = K(\mathbf{x}_*, \mathbf{x})[K(\mathbf{x}, \mathbf{x}) + \sigma_n^2 I]^{-1}\delta(\mathbf{x}) \qquad \text{Eq. 4. 3}$$

where $K(\mathbf{x}_*, \mathbf{x})$ stands for $n_* \times n$ covariance matrix calculated at all pairs of training and prediction points; n and $n_*$ are the number of training and prediction points, respectively; $K(\mathbf{x}, \mathbf{x})$ is the n×n covariance matrix at all training points; $\sigma_n$ is the standard deviation of noisy observation of the bias function due to the epistemic uncertainty; and $I$ is the identity matrix. For each element in the covariance matrix, a commonly used squared-exponential covariance function is selected with the following form as

$$k(\mathbf{x}, \mathbf{x}') = \sigma_\delta^2 \exp\left[-\frac{(\mathbf{x}-\mathbf{x}')(\mathbf{x}-\mathbf{x}')^T}{2l^2}\right] \qquad \text{Eq. 4. 4}$$

where **x**' is the dummy variable of **x**; $\sigma_\delta^2$ and $l$ represent the bias variance and the characteristic length scale, respectively. Optimal parameters of the GP regression model, i.e., $\sigma_\delta$, $l$, and $\sigma_n$, can be determined based on the training data with the maximum likelihood estimation [91].

### 4.3.4. Parameter uncertainty calibration

With predetermined bias function and available experiment data for melt pool prediction, the objective of this section is to calibrate parameter uncertainty of $\boldsymbol{\theta}$ e.g., powder absorptivity and spot diameter, such that the corrected model prediction in Eq. 4.1 could reach the best agreement with experiment data under unknown realization of $\boldsymbol{\theta}^*$. To quantify the degree of agreement between model prediction under uncertainty of $\boldsymbol{\theta}$ and several experiment data at different configurations, u-pooling metric [92] is adopted since it can pool experiment data at different configurations to form an accuracy measurement of the simulation model. In particular, the calibration problem can be formulated as

$$\min U[Y_m(\mathbf{x}, \boldsymbol{\theta}) + \delta(\mathbf{x}), Y_t(\mathbf{x}, \boldsymbol{\theta}^*)] \qquad \text{Eq. 4. 5}$$

where U[•,•] is the u-pooling metric measuring the degree of agreement between the corrected model prediction and available experiment data, and the smaller u-pooling value the better with the range from 0 to 0.5. The optimization in Eq. 4.5 is to adjust the distribution of $\boldsymbol{\theta}$ such that the metric is minimized. If arbitrary distribution would be used, then the first four statistical moments of $\boldsymbol{\theta}$, i.e., mean, standard deviation, skewness and kurtosis, can be used as optimization parameters combining with any probability estimation methods such as the Pearson system, Johnson system, saddle-point approximation,

etc.[93]. For simplicity, Normal distribution could be assumed by calibrating only the mean and standard deviation of the parameter $\boldsymbol{\theta}$.

The u-pooling metric is dependent on the number of experiment data. Assuming that there are total $n$ experiment data under $n$ different configurations defined by parameter $\mathbf{x}$, i.e., one experiment datum at each configuration, the cumulative distribution function (CDF) value realization of such experiment datum at corresponding model prediction can be calculated by quantifying the CDF of the corrected model prediction under given $\boldsymbol{\theta}$, i.e., $u_i = F_{Ym+\delta}(Y_{ti})$ where $F_{Ym+\delta}(\bullet)$ is the CDF from the corrected model prediction; $Y_{ti}$ is the $i^{th}$ experiment datum; and $i = 1, 2, \ldots, n$. According to u-pooling metric, the empirical CDF formed by $u_i$ should follow the standard uniform distribution if experiment data were truly random realizations from the model prediction. Otherwise, such empirical CDF would deviate greatly from the standard uniform distribution. As such, the area difference between the empirical CDF and the standard uniform distribution is defined as the u-pooling metric. Since the empirical CDF is employed, evaluation of the model accuracy using the u-pooling metric should not only check the absolute metric value but also the total number of experiment data.

### 4.3.5. Validation hypothesis test based on the u-pooling metric

Since u-pooling is used to quantify the degree of agreement of model prediction versus experiment data at different configurations, validation hypothesis test based on a set of new experiment data can also be conducted based on the u-pooling metric. The statistic inference developed earlier in [86] is adopted to include the effects from different number of experiment data. The general procedure is presented as follows.

*Step 1:* Generate *n* number of random samples from a standard Normal distribution, where *n* corresponds to the number of experiment data for validation;

*Step 2:* Calculate the CDF value of those *n* samples;

*Step 3:* Calculate the u-pooling metric;

*Step 4:* Repeat Steps 1 to 3 sufficient times, e.g., 100,000, to obtain the u-pooling metric distribution given *n* samples;

*Step 5:* Obtain one-side confidence level, e.g., 95%, for the u-pooling metric given *n* samples.

For validation hypothesis testing with *n* experiment data, if the calculated u-pooling metric is located outside predefined confidence level, e.g., 95%, then the null hypothesis should be rejected.

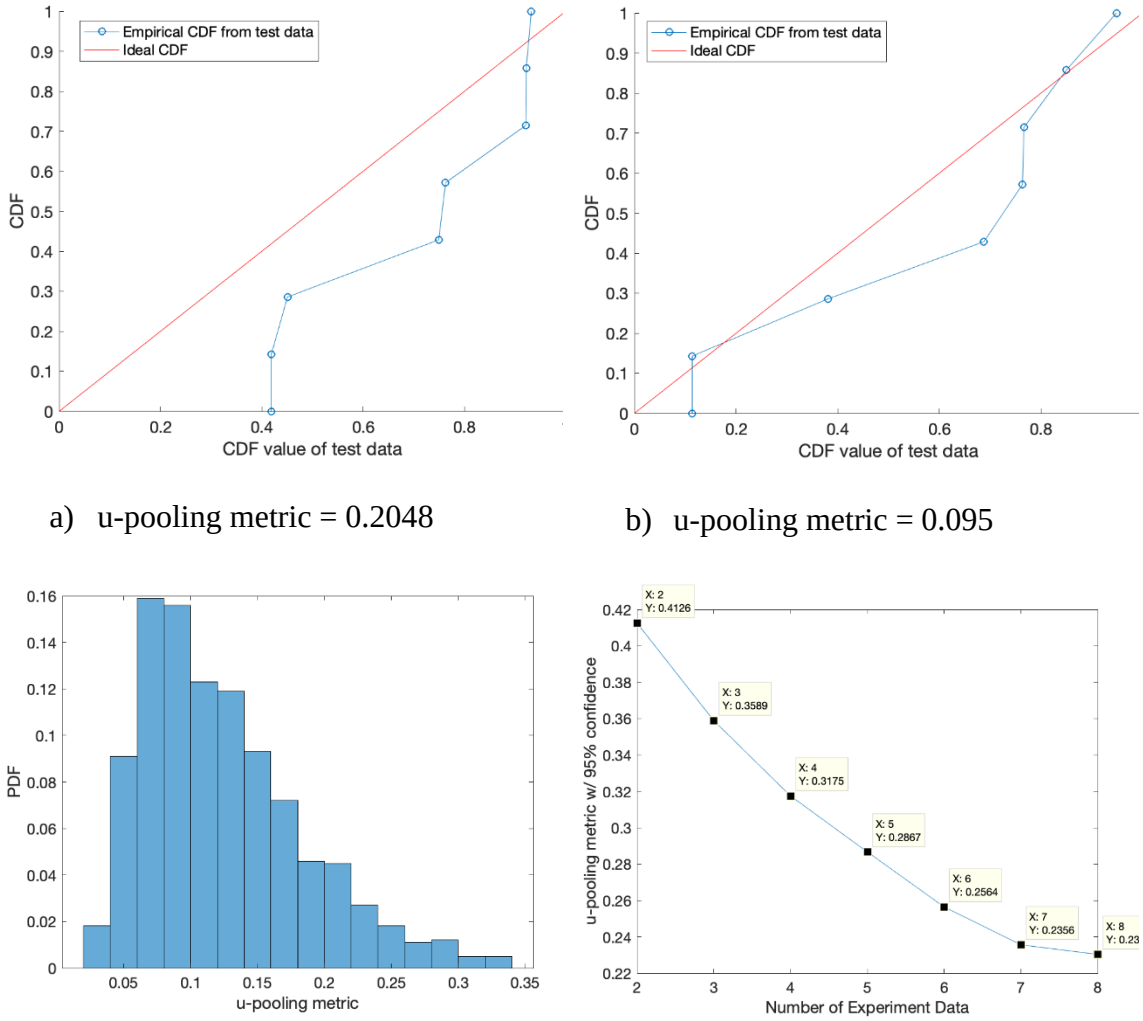


a) u-pooling metric = 0.2048

b) u-pooling metric = 0.095

c) u-pooling metric distribution with 7 experiment data

d) 95% confidence level of the u-pooling metric with different number of experiment data

**Figure 4. 2.** u-pooling metric calculation, distribution, and 95% confidence levels

Figure 4.8 a-c shows such an example with assumed 7 experiment data for validation. Due to limited number of experiment data and their random realizations, u-pooling metric could be different as shown in Figure 4.8 a-b even though experiment data are generated from the simulation distribution. As such, if sufficient such calculations are repeated, the u-pooling metric distribution can be obtained as shown in Figure 3.8 c, which forms the foundation for hypothesis test based on the u-pooling metric. Since u-pooling is the smaller the better case, one side confidence level should be used, which is identified as 0.2356 with 95% confidence level for 7 experiment data. Similar study can be conducted for different number of experiment data and the results are shown in Figure 4.8 d when experiment data range from 2 to 8.

### *4.4. Meta-modeling using the GP regression model*

It is not suitable to determine the optimal parameter setting for the LPBF process based on the FEM especially when parameter uncertainties should be considered as well. Based on the FEM, however, a low-fidelity model can be constructed using machine learning methods. In particular, the GP regression model was employed in this paper. Latin hypercube sampling was adopted and a total of 94 finite element (FE) simulations were run at different levels of four process parameters, i.e., laser power, scanning speed, powder absorptivity, and laser spot diameter. Since FE simulation contains numerical errors as shown in Figures 4.1 to 4.3, the mean of the melt pool width and depth was used as deterministic outputs for the meta-model construction. Figure 4.9 shows the melt pool prediction results based on the GP regression model. For visualization, the results are shown with respect to the change of each variable while fixing the other variables at the

fixed level, i.e., power = 123 $W$, speed = 833 $mm/s$, absorptivity = 0.57, and diameter = 85 $\mu m$. The results make sense because both melt-pool width and depth increase with increased laser power, or reduced scanning speed, or increased powder absorptivity. Only the laser spot diameter shows nonmonotonic behaviors while fixing the other process parameters.

It is worth noting a few important things of the meta-model. Firstly, the meta-model is certainly extremely efficient compared to the FE simulations. Hence, it can ideally be used for various purposes such as design considering uncertainty or tools for online quality control for the LPBF process. Secondly, the meta-model contains model bias compared to the FE simulations in the whole parameter domain as shown in Figure 4.9. The degree of bias is determined by the amount of training data generated from the FE simulations. This chapter treats the meta-model as a baseline model for model calibration and validation, hence, the bias between the meta-model and FE simulations is not studied. If the meta-model is not accurate, more experiment data would be required for calibration and validation because the bias between the meta-model and experiments could be significant; otherwise, less experiment data may be needed. As such, FEM and corresponding meta-model should be reasonably accurate to alleviate the need of many experiment data for model calibration and validation.

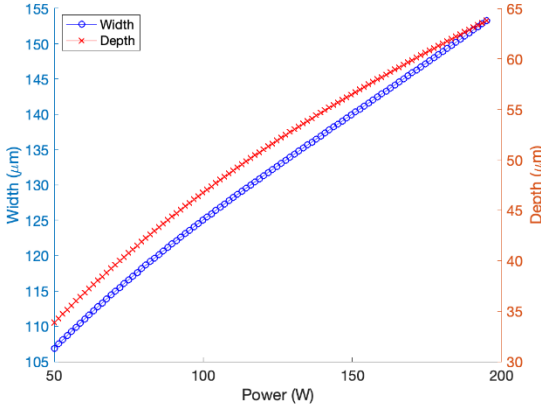


Melt pool size with respect to laser power

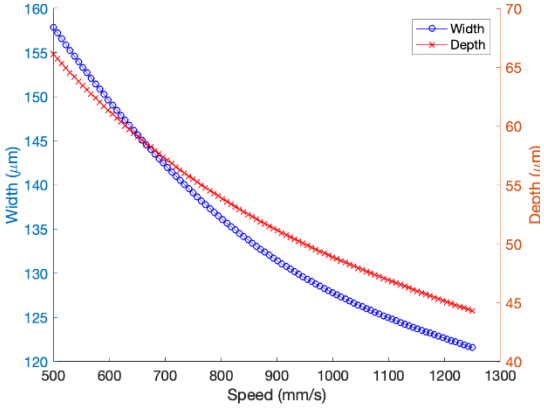


Melt pool size with respect to laser scanning speed

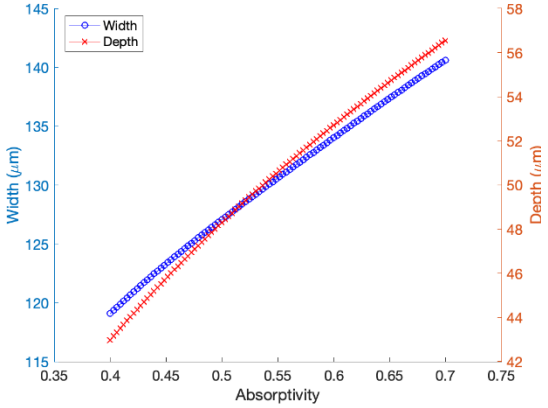


Melt pool size with respect to powder absorptivity

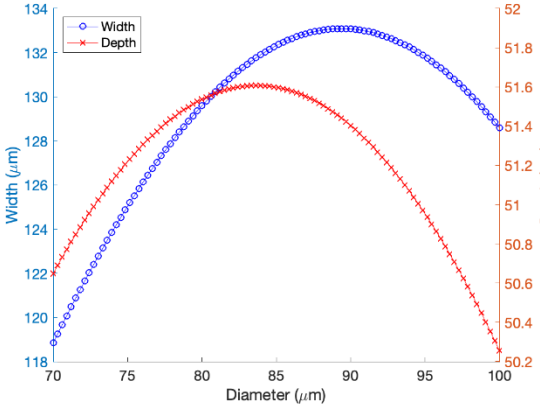


Melt pool size with respect to laser spot diameter

**Figure 4. 3.** Melt pool width and depth with respect to four process parameters based on the GP regression model

### 4.4.1. Experimental data for bias and parameter calibration

Experiment data in [42] were used for model calibration and validation for the LPBF process. Table 4.1 shows a set of training configurations, where the melt pool width and depth were measured at different power and speed levels. Powder absorptivity and laser

spot diameter were not measured and hence are treated as unknown random parameters which need to be calibrated. The objective is to calibrate the randomness of unknown model parameters along with the bias calibration based on the training data shown in Table 4.1.

With prior assumption for randomness of powder absorptivity and spot diameter, i.e., absorptivity ~ $Normal(0.55,\ 0.05^2)$ and spot diameter ~ $Normal(85,\ 5^2)$, Monte Carlo simulation (MCS) were employed to quantify the melt pool size uncertainty at nine training configurations based on the meta-model learned in Section 4.1. The results are shown in Figure 4.10 where the box plots indicate the uncertainty distribution from the meta-model and the star symbol is one experiment datum at each training configuration. It is observed that the meta-model prediction has noticeable magnitude difference compared to the experiment data, although the overall trend is consistent with the experiment results. For example, both melt pool width and depth decrease with increased scanning speed at fixed power levels, which are both reflected from simulation and experiment data.

Table 4. 1 **:** Training data for bias and parameter calibration

| Training ID | Power [Watt] | Speed [mm/s] | Width (μm) | Depth (μm) |
|---|---|---|---|---|
| #1 | 50 | 500 | 67.0 | 17.5 |
| #2 | 50 | 1000 | 45.0 | 10.0 |
| #3 | 100 | 500 | 118.1 | 43.6 |
| #4 | 100 | 1200 | 72.2 | 22.1 |
| #5 | 150 | 500 | 145.2 | 101.2 |
| #6 | 150 | 750 | 135.0 | 71.7 |
| #7 | 150 | 1200 | 108.3 | 48.9 |
| #8 | 195 | 750 | 161.2 | 110.0 |
| #9 | 195 | 1200 | 122.5 | 64.6 |

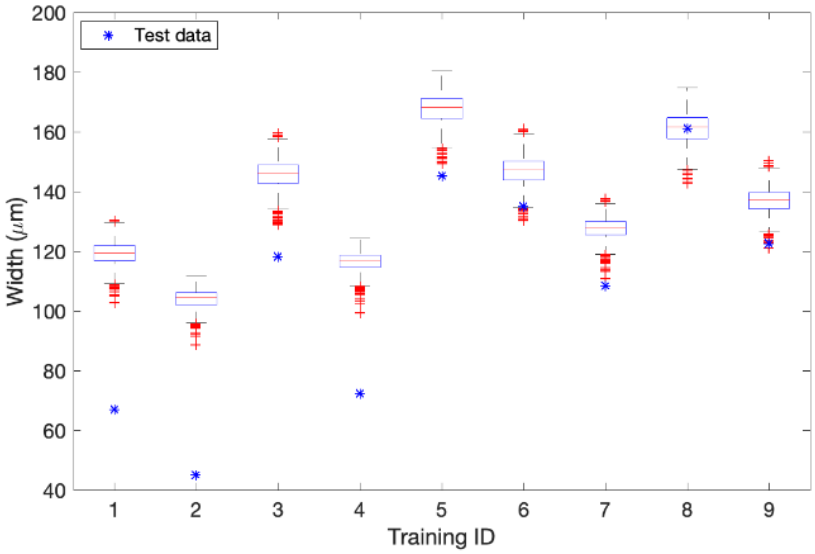


a) Melt pool width comparison

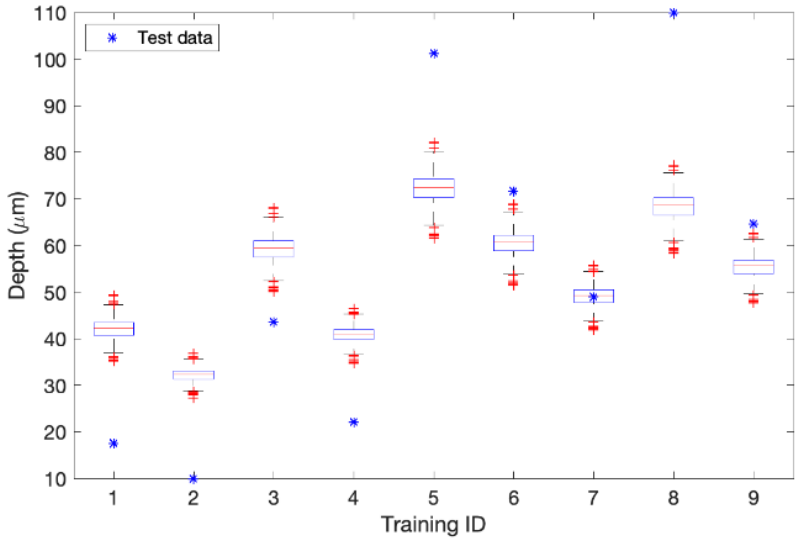


b) Melt pool depth comparison

Figure 4. 4. Melt pool estimation vs. experiment data before bias calibration at nine training configurations

After bias calibration based on Eqs. 3.2 and 3.3, bias of the meta-model was characterized by two GP regression models for melt pool width and depth, respectively. It should be noted that the expected model bias at nine training configurations contains epistemic uncertainties since there is only one experiment datum at each configuration. Consequently, the noisy parameter in the GP regression model should be estimated together with the two parameters in the covariance function. By considering such bias models as a function of laser power and scanning speed, accuracy of the corrected meta-model at nine training configurations would be dramatically improved. Figure 4.11 shows the corrected model prediction after incorporating the calibrated model bias, where all experiment data are located inside certain confidence intervals from the model prediction. It is worth noting that experiment data should not be at the median or mean value of the model prediction for all nine training configurations, which is extremely unlikely because of the random realization of two unknown model parameters, i.e., absorptivity and spot diameter. As such, u-pooling is an ideal metric to quantify such degree of agreement at different configurations. Figure 4.12 shows u-pooling metric for both responses, where reasonable degree of agreement is observed for both melt pool width and depth predictions.

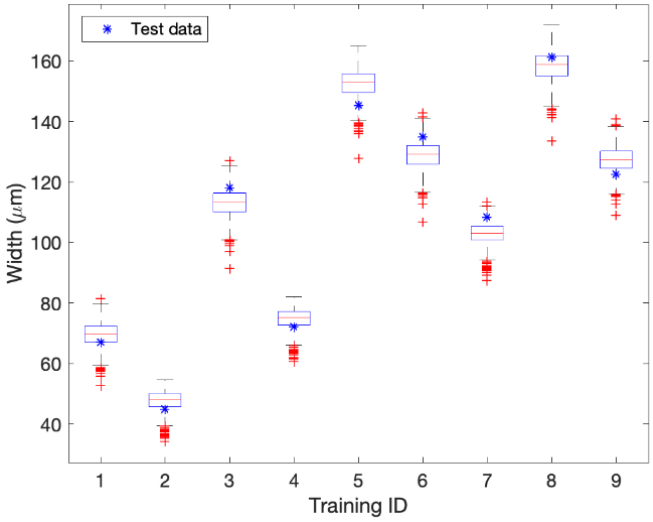


a) Melt pool width comparison

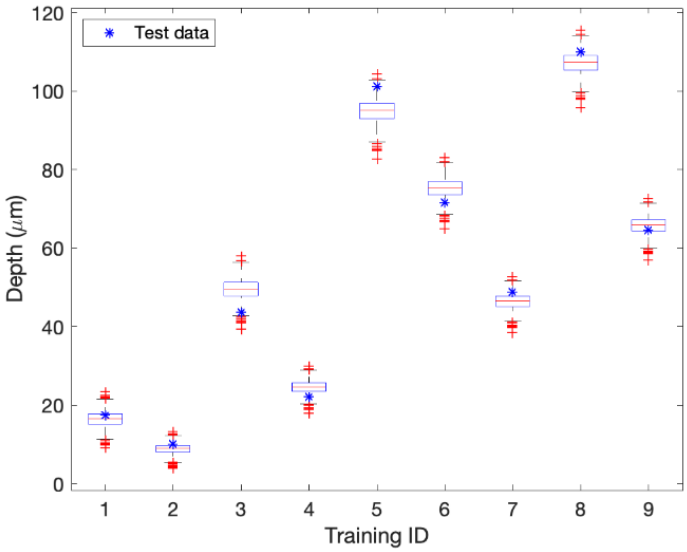


b) Melt pool depth comparison

**Figure 4. 5.** Melt pool estimation vs. experiment data after bias calibration at nine training configurations

With predetermined model bias, the degree of agreement can be further improved through the calibration of unknown random parameters, i.e., powder absorptivity and spot diameters, based on Eq. 4.5. Since there are two model responses under the same random realizations, the objective was defined to minimize the u-pooling summation for both melt pool width and depth. In addition, both parameters were assumed to follow Normal distributions. The u-pooling results are shown in Figure 4.13 at the optimal parameter distributions, i.e., absorptivity ~ Normal (0.56, $0.05^2$) and spot diameter ~ Normal (81.3, $1.8^2$). Before and after the parameter calibration, the u-pooling summation, i.e., the objective function, was reduced from 0.2148 to 0.1846, indicating better overall degree of agreement with 14.06% u-pooling reduction.

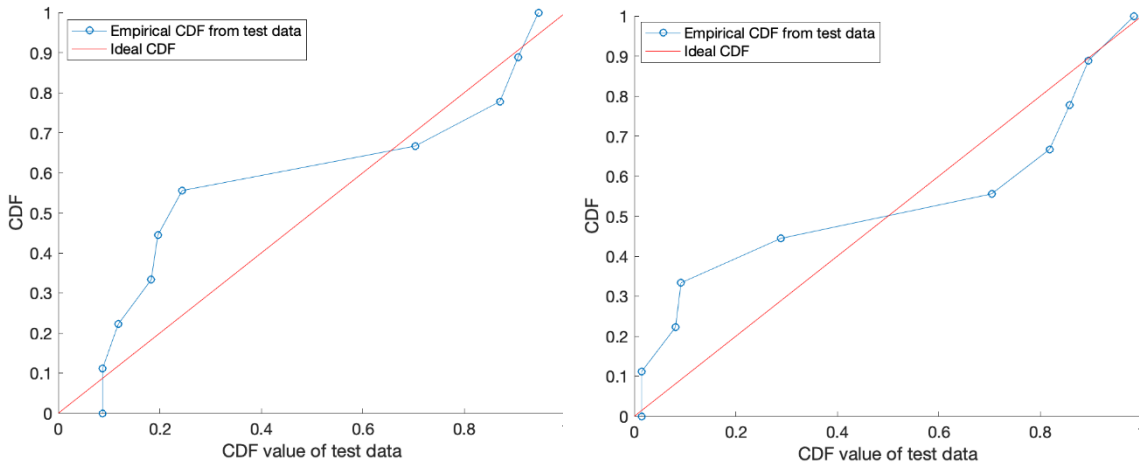


a) U-pooling metric: U = 0.1100 b) U-pooling metric: U = 0.1048

**Figure 4. 6.** u-pooling quantification of the melt pool estimation vs. experiment data after bias calibration at nine training configurations

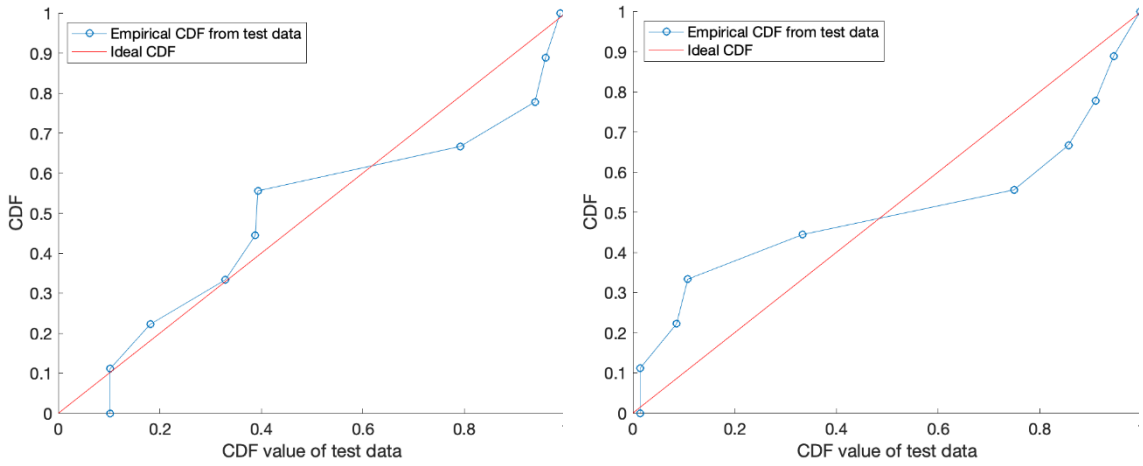


a) U-pooling metric: U = 0.0665 b) U-pooling metric: U = 0.1181

**Figure 4. 7.** u-pooling quantification of the melt pool estimation vs. experiment data after bias and parameter calibration at nine training configurations

### 4.4.2. Validation of the corrected meta-model

The objective of this section is to validate the corrected meta-model by employing new experiment data under new printing configurations. Instead of observing the comparison one by one at each configuration, validation hypothesis test was used based on the u-pooling metric for a set of new configurations. In particular, validation configurations and melt pool measurements are shown in Table 4.2, which is a subset of the experiment results in [42].

Melt pool prediction at five new configurations was obtained based on the corrected meta-model using the MCS and their comparison with experiment data is shown in Figure 4.14 a-b for the melt pool width and depth, respectively. For each configuration, experiment datum is located inside certain confidence intervals from the model prediction, where the

melt pool uncertainty is due to the randomness of powder absorptivity and spot diameter which has been calibrated based on the training data. Considering all five validation configurations, u-pooling metric was calculated and results are shown in Figure 4.14 c-d. In particular, u-pooling metric is 0.2107 and 0.2923 for melt pool width and depth, respectively. According to the u-pooling metric with 95% confidence interval in Figure 4.14 d, the threshold to reject the model is 0.2867 with five experiment data. Hence, melt pool depth prediction should be further improved by adding new experiment data for bias and parameter calibration, and there is no statistical evidence to reject the corrected meta-model for melt pool width prediction.

Table 4. 2. Experiment data for model validation at five new configurations

| Validation ID | Power [Watt] | Speed [mm/s] | Width (μm) | Depth (μm) |
|---|---|---|---|---|
| #1 | 50 | 750 | 50.0 | 12.0 |
| #2 | 100 | 750 | 98.4 | 31.9 |
| #3 | 100 | 1000 | 75.3 | 23.9 |
| #4 | 150 | 1000 | 116.1 | 52.6 |
| #5 | 195 | 1000 | 130.4 | 81.3 |

Firstly, whether the model is valid or not depends on the validation data, e.g., the number and their specific configurations. In Table 4.2, validation configurations include power ranging from 50 W to 195 W and speed as 750 mm/s and 1000 mm/s. Hence, the interpretation of a valid model should not be beyond the calibration and validation range, i.e., the parameter range shown in Table 4.1 and Table 4.2. If more validation data could be collected, e.g., melt pool measurement at other power and speed levels, the conclusion

would be more certain. On the other hand, even if model may not be valid considering all validation configurations, the model could be valid at certain reduced parameter range. As such, the model may be partially trustable for design purpose.

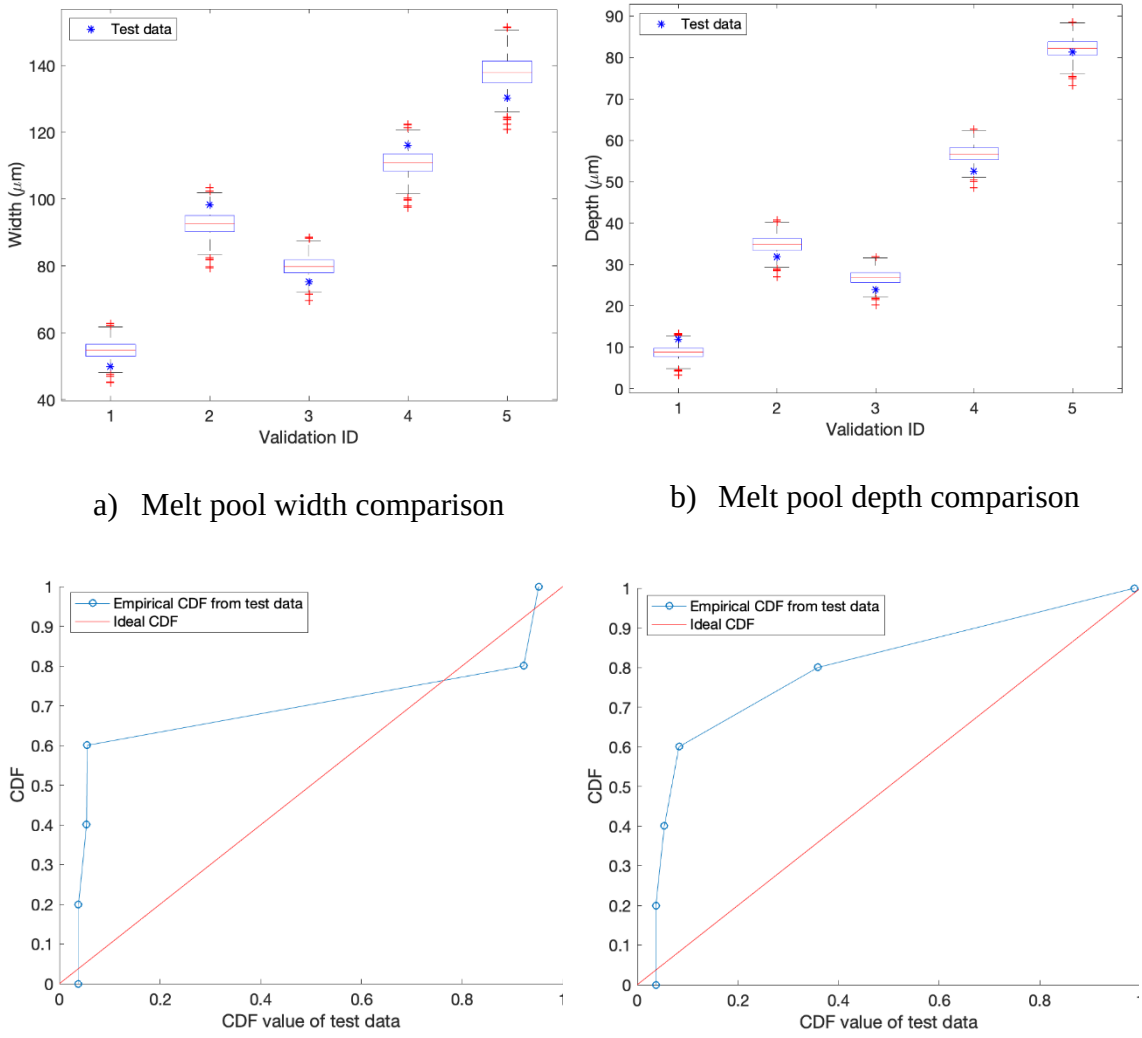


a) Melt pool width comparison

b) Melt pool depth comparison

c) Width u-pooling metric: U = 0.2107

d) Depth u-pooling metric: U = 0.2923

**Figure 4. 8.** Melt pool size estimation, comparison, and accuracy quantification of the corrected meta-model after bias and parameter calibration

Secondly, selection of representative training data is critical for bias and parameter calibration. Ideally, training data should include the interested operation domain of the LPBF process. For example, training data in Table 4.1 cover power from 50 W to 195 W and speed from 500 mm/s to 1200 mm/s. Under such conditions, the amount of training data would be critical. Generally, more training data indicate more accurate bias modeling and parameter uncertainty quantification over the whole operation domain. Otherwise, the bias model could either be overfitted or contain too much uncertainties, depending on specific modeling technique, due to the lack of information. For example, if training configurations #2 and #7 in Table 4.1 were removed and included as validation data, the corrected meta-model would not be valid for both melt pool width and depth predictions.

Thirdly, GP regression model was employed for bias modeling and only the mean function was used for bias estimation at validation configurations. Such bias estimation contains epistemic uncertainties due to: i) limited training data, and ii) inaccurate bias estimation because of only one experiment observation at each training configuration. By incorporating the bias uncertainty, e.g., variance of the bias estimation in the GP model, uncertainty range in Figure 4.14 a-b would be increased, which would further affect the u-pooling metric in Figure 4.14 c-d. Typically, it would be less likely to reject the model with larger uncertain range. However, the model prediction would also be less practically useful due to too wide uncertain range. As such, balance should be made to reduce the epistemic uncertainty in bias modeling with reasonable amount of training data.

# 5. Contribution and Future Work

## *5.1. Contribution*

The dissertation focuses on developing efficient and accurate physics-based modeling for Laser Powder Bed Fusion (LPBF) process. The first chapter highlights the quality issues and mechanical properties variation for parts manufactured by LPBF as the process parameters change, and the importance of understanding the process behavior and postprocessing techniques towards manufacturing reliable and high-quality parts.

In the second chapter, the thermal modeling of LPBF was investigated. The developed models using finite element method with adaptive remeshing were used to predict melt pool size and its location dependency, lack of fusion porosity, and thermal history during manufacturing parts from Ti-6Al-4V alloys. The finite element model predictions were validated against experimental results from the literature. In addition, the thermal modeling with adaptive remeshing was proven to be much more computationally efficient compared to models without adaptive remeshing where over 85% of the computational time could be reduced.

In the third chapter, the thermally induced residual stresses and strains and distortions were investigated during the build of different parts (NIST AMB-2018-01 cantilever, bridge and square canonical parts) using thermomechanical finite element modeling with adaptive remeshing. The residual stresses and strains, and distortion solution was validated by the experimental results published by NIST and other studies.

The results were validated against the experimental results published by NIST and other studies. In addition, different configurations of adaptive remeshing were investigated where the computational time and RAM utilization could be reduced by up to 80%.

In the fourth chapter, a general calibration and validation framework for the LPBF process based on physics-based multi-fidelity models was proposed. The framework effectively integrates finite element modeling of the LPBF process, meta-modeling using the Gaussian Process regression, and model calibration and validation techniques to develop an extremely efficient and accurate meta-model for melt pool size predictions under intended process parameters configurations. The effectiveness of the proposed work has been demonstrated with the aid of experiment data for both melt pool width and depth measurements under 14 process parameters configurations. With reasonable accuracy of the finite element model, the meta-model learned from the finite element model, and a few selected training data for model bias and parameter calibration, the corrected meta-model can estimate the melt pool size accurately under different printing configurations. Unlike direct machining learning methods relying on abundant experiment data, the proposed framework relies on only limited experiment data for model calibration and validation. Furthermore, due to physics-based modeling using the finite element analysis, the modeling mechanism can be easily extended to different additive manufacturing structures without repeatedly requiring a large amount of experiment data.

### *5.2. Future work*

The modeling work in this dissertation is one step towards developing an understanding of how part quality could be improved during LPBF. In the modeling direction, improving and making the numerical modeling much faster (e.g. by developing reduced-order models) will be of a great importance. Such fast finite element thermal modeling will be helpful optimizing the process parameters, controlling porosity and microstructure, and eventually have high reliable parts that may not require postprocessing heat treatment processes.

In addition, the thermomechanical modeling part can be very beneficial in designing parts. A closed-loop design optimization can be developed to reduce residual stresses and parts distortions utilizing the fast-thermomechanical finite element modeling approach proposed in this work. Such framework will be very beneficial for the design community to reduce design cycles time. In addition, the modeling with adaptive remeshing could be extended for the use in the other additive manufacturing processes including Directed Energy Deposition, etc.

Future work on the model calibration can address improving the predictive model capability to accurately predict the distortion and residual stresses distributions. The material properties reported by the manufacturer datasheet and assumed in this work may change if there is a change in the part size, build orientation, or process parameters. In addition, the material properties may change within the same part from a location to another as heating and cooling rates are different. In this regard, a calibration model in which material properties (such as the yield strength) are calibrated at different sets of build conditions would be of a great interest.

# 6. References


[1] K. N. Amato *et al.*, “Microstructures and mechanical behavior of Inconel 718 fabricated by selective laser melting,” *Acta Mater.*, vol. 60, no. 5, pp. 2229–2239, 2012, doi: 10.1016/j.actamat.2011.12.032.

[2] A. Iveković *et al.*, “Selective laser melting of tungsten and tungsten alloys,” *Int. J. Refract. Met. Hard Mater.*, vol. 72, no. December 2017, pp. 27–32, 2018, doi: 10.1016/j.ijrmhm.2017.12.005.

[3] J. Kruth, P. Mercelis, J. Van Vaerenbergh, L. Froyen, and M. Rombouts, “Binding mechanisms in selective laser sintering and selective laser melting,” *Rapid Prototyp. J.*, vol. 11, no. 1, pp. 26–36, Feb. 2005, doi: 10.1108/13552540510573365.

[4] H. Gong, K. Rafi, H. Gu, T. Starr, and B. Stucker, “Analysis of defect generation in Ti–6Al–4V parts made using powder bed fusion additive manufacturing processes,” *Addit. Manuf.*, vol. 1–4, pp. 87–98, Oct. 2014, doi: 10.1016/j.addma.2014.08.002.

[5] I. Gibson, D. Rosen, and B. Stucker, *Additive Manufacturing Technologies*. 2015.

[6] I. Yadroitsev, *Selective laser melting: Direct manufacturing of 3D-objects by selective laser melting of metal powders*. LAP Lambert Academic Publishing, 2009.

[7] H. Gong, K. Rafi, H. Gu, G. D. Janaki Ram, T. Starr, and B. Stucker, “Influence of defects on mechanical properties of Ti–6Al–4V components produced by selective laser melting and electron beam melting,” *Mater. Des.*, vol. 86, pp. 545–554, Dec. 2015, doi: 10.1016/j.matdes.2015.07.147.

[8] S. Leuders *et al.*, “On the mechanical behaviour of titanium alloy TiAl6V4 manufactured by selective laser melting: Fatigue resistance and crack growth performance,” *Int. J. Fatigue*, vol. 48, pp. 300–307, Mar. 2013, doi: 10.1016/j.ijfatigue.2012.11.011.

[9] H. Gong *et al.*, “Melt pool characterization for selective laser melting of Ti-6Al-4V pre-alloyed powder,” *Solid Free. Fabr. Symp. Proc.*, pp. 256–267, 2014.

[10] L. Thijs, F. Verhaeghe, T. Craeghs, J. Van Humbeeck, and J.-P. Kruth, "A study of the microstructural evolution during selective laser melting of Ti–6Al–4V," *Acta Mater.*, vol. 58, no. 9, pp. 3303–3312, May 2010, doi: 10.1016/j.actamat.2010.02.004.

[11] H. Ali, H. Ghadbeigi, and K. Mumtaz, "Effect of scanning strategies on residual stress and mechanical properties of Selective Laser Melted Ti6Al4V," *Mater. Sci. Eng. A*, vol. 712, pp. 175–187, Jan. 2018, doi: 10.1016/j.msea.2017.11.103.

[12] J. Kruth, M. Badrossamay, E. Yasa, J. Deckers, L. Thijs, and J. Van Humbeeck, "Part and material properties in selective laser melting of metals," *16th Int. Symp. Electromachining*, pp. 1–12, 2010.

[13] S. Zhang, Q. Wei, L. Cheng, S. Li, and Y. Shi, "Effects of scan line spacing on pore characteristics and mechanical properties of porous Ti6Al4V implants fabricated by selective laser melting," *Mater. Des.*, vol. 63, pp. 185–193, Nov. 2014, doi: 10.1016/j.matdes.2014.05.021.

[14] C. Leyens and M. Peters, *Titanium an Titanium Alloys*. 2003.

[15] B. E. Carroll, T. A. Palmer, and A. M. Beese, "Anisotropic tensile behavior of Ti-6Al-4V components fabricated with directed energy deposition additive manufacturing," *Acta Mater.*, vol. 87, pp. 309–320, 2015, doi: 10.1016/j.actamat.2014.12.054.

[16] R. Wauthle *et al.*, "Effects of build orientation and heat treatment on the microstructure and mechanical properties of selective laser melted Ti6Al4V lattice structures," *Addit. Manuf.*, vol. 5, pp. 77–84, 2015, doi: 10.1016/j.addma.2014.12.008.

[17] X. Zhao *et al.*, "Comparison of the microstructures and mechanical properties of Ti–6Al–4V fabricated by selective laser melting and electron beam melting," *Mater. Des.*, vol. 95, pp. 21–31, Apr. 2016, doi: 10.1016/j.matdes.2015.12.135.

[18] M. Shunmugavel, A. Polishetty, and G. Littlefair, "Microstructure and Mechanical Properties of Wrought and Additive Manufactured Ti-6Al-4V Cylindrical Bars," *Procedia Technol.*, vol. 20, no. July, pp. 231–236, 2015, doi: 10.1016/j.protcy.2015.07.037.

[19] P. Edwards and M. Ramulu, “Fatigue performance evaluation of selective laser melted Ti-6Al-4V,” *Mater. Sci. Eng. A*, vol. 598, pp. 327–337, 2014, doi: 10.1016/j.msea.2014.01.041.

[20] J. Zhao, M. Easton, M. Qian, M. Leary, and M. Brandt, “Effect of building direction on porosity and fatigue life of selective laser melted AlSi12Mg alloy,” *Mater. Sci. Eng. A*, vol. 729, pp. 76–85, Jun. 2018, doi: 10.1016/j.msea.2018.05.040.

[21] E. Wycisk, A. Solbach, S. Siddique, D. Herzog, F. Walther, and C. Emmelmann, “Effects of Defects in Laser Additive Manufactured Ti-6Al-4V on Fatigue Properties,” *Phys. Procedia*, vol. 56, pp. 371–378, 2014, doi: 10.1016/j.phpro.2014.08.120.

[22] S. A. Khairallah and A. Anderson, “Mesoscopic simulation model of selective laser melting of stainless steel powder,” *J. Mater. Process. Technol.*, vol. 214, no. 11, pp. 2627–2636, 2014, doi: 10.1016/j.jmatprotec.2014.06.001.

[23] S. A. Khairallah, A. T. Anderson, A. Rubenchik, and W. E. King, “Laser powder-bed fusion additive manufacturing: Physics of complex melt flow and formation mechanisms of pores, spatter, and denudation zones,” *Acta Mater.*, vol. 108, pp. 36–45, Apr. 2016, doi: 10.1016/j.actamat.2016.02.014.

[24] H. W. Mindt, O. Desmaison, M. Megahed, A. Peralta, and J. Neumann, “Modeling of Powder Bed Manufacturing Defects,” *J. Mater. Eng. Perform.*, vol. 27, no. 1, pp. 32–43, 2018, doi: 10.1007/s11665-017-2874-5.

[25] D. Pal *et al.*, “A Generalized Feed-Forward Dynamic Adaptive Mesh Refinement and Derefinement Finite-Element Framework for Metal Laser Sintering—Part II: Nonlinear Thermal Simulations and Validations $^{2}$,” *J. Manuf. Sci. Eng.*, vol. 138, no. 6, p. 061003, 2016, doi: 10.1115/1.4032078.

[26] A. Hussein, L. Hao, C. Yan, and R. Everson, “Finite element simulation of the temperature and stress fields in single layers built without-support in selective laser melting,” *Mater. Des.*, vol. 52, pp. 638–647, Dec. 2013, doi: 10.1016/j.matdes.2013.05.070.

[27] S. Roy, M. Juha, M. S. Shephard, and A. M. Maniatty, “Heat transfer model and

finite element formulation for simulation of selective laser melting," *Comput. Mech.*, vol. 62, no. 3, pp. 273–284, 2018, doi: 10.1007/s00466-017-1496-y.

[28] K. Karayagiz *et al.*, "Numerical and experimental analysis of heat distribution in the laser powder bed fusion of Ti-6Al-4V," *IISE Trans.*, pp. 1–17, Apr. 2018, doi: 10.1080/24725854.2018.1461964.

[29] A. K. Mishra and A. Kumar, "Numerical and experimental analysis of the effect of volumetric energy absorption in powder layer on thermal-fluidic transport in selective laser melting of Ti6Al4V," *Opt. Laser Technol.*, vol. 111, pp. 227–239, Apr. 2019, doi: 10.1016/j.optlastec.2018.09.054.

[30] C. H. Fu and Y. B. Guo, "Three-Dimensional Temperature Gradient Mechanism in Selective Laser Melting of Ti-6Al-4V," *J. Manuf. Sci. Eng.*, vol. 136, no. 6, p. 061004, 2014, doi: 10.1115/1.4028539.

[31] J. Irwin and P. Michaleris, "A Line Heat Input Model for Additive Manufacturing," *J. Manuf. Sci. Eng.*, vol. 138, no. 11, p. 111004, Jun. 2016, doi: 10.1115/1.4033662.

[32] I. A. Roberts, C. J. Wang, R. Esterlein, M. Stanford, and D. J. Mynors, "A three-dimensional finite element analysis of the temperature field during laser melting of metal powders in additive layer manufacturing," *Int. J. Mach. Tools Manuf.*, vol. 49, no. 12–13, pp. 916–923, 2009, doi: 10.1016/j.ijmachtools.2009.07.004.

[33] T. P. Moran, P. Li, D. H. Warner, and N. Phan, "Utility of superposition-based finite element approach for part-scale thermal simulation in additive manufacturing," *Addit. Manuf.*, vol. 21, no. March, pp. 215–219, 2018, doi: 10.1016/j.addma.2018.02.015.

[34] N. Patil *et al.*, "A Generalized Feed Forward Dynamic Adaptive Mesh Refinement and Derefinement Finite Element Framework for Metal Laser Sintering—Part I: Formulation and Algorithm Development," *J. Manuf. Sci. Eng.*, vol. 137, no. 4, p. 041001, Aug. 2015, doi: 10.1115/1.4030059.

[35] Z. Luo and Y. Zhao, "Numerical simulation of part-level temperature fields during selective laser melting of stainless steel 316L," *Int. J. Adv. Manuf. Technol.*, vol. 104, no. 5–8, pp. 1615–1635, Oct. 2019, doi: 10.1007/s00170-019-03947-0.

[36] M. Gouge, E. Denlinger, J. Irwin, C. Li, and P. Michaleris, “Experimental validation of thermo-mechanical part-scale modeling for laser powder bed fusion processes,” *Addit. Manuf.*, vol. 29, no. June, p. 100771, 2019, doi: 10.1016/j.addma.2019.06.022.

[37] Z. Luo and Y. Zhao, “A survey of finite element analysis of temperature and thermal stress fields in powder bed fusion Additive Manufacturing,” *Addit. Manuf.*, vol. 21, no. March 2017, pp. 318–332, 2018, doi: 10.1016/j.addma.2018.03.022.

[38] B. Song, S. Dong, B. Zhang, H. Liao, and C. Coddet, “Effects of processing parameters on microstructure and mechanical property of selective laser melted Ti6Al4V,” *Mater. Des.*, vol. 35, pp. 120–125, Mar. 2012, doi: 10.1016/j.matdes.2011.09.051.

[39] E. R. Denlinger, J. C. Heigel, and P. Michaleris, “Residual stress and distortion modeling of electron beam direct manufacturing Ti-6Al-4V,” *Proc. Inst. Mech. Eng. Part B J. Eng. Manuf.*, vol. 229, no. 10, pp. 1803–1813, Oct. 2015, doi: 10.1177/0954405414539494.

[40] M. Boivineau *et al.*, “Thermophysical properties of solid and liquid Ti-6Al-4V (TA6V) alloy,” *Int. J. Thermophys.*, vol. 27, no. 2, pp. 507–529, 2006, doi: 10.1007/PL00021868.

[41] L. C. Wei, L. E. Ehrlich, M. J. Powell-Palm, C. Montgomery, J. Beuth, and J. A. Malen, “Thermal conductivity of metal powders for powder bed additive manufacturing,” *Addit. Manuf.*, vol. 21, pp. 201–208, 2018, doi: 10.1016/j.addma.2018.02.002.

[42] J. J. S. Dilip *et al.*, “Influence of processing parameters on the evolution of melt pool, porosity, and microstructures in Ti-6Al-4V alloy parts fabricated by selective laser melting,” *Prog. Addit. Manuf.*, vol. 2, no. 3, pp. 157–167, Sep. 2017, doi: 10.1007/s40964-017-0030-2.

[43] W. E. King *et al.*, “Observation of keyhole-mode laser melting in laser powder-bed fusion additive manufacturing,” *J. Mater. Process. Tech.*, vol. 214, no. 12, pp. 2915–2925, 2014, doi: 10.1016/j.jmatprotec.2014.06.005.

[44] T. Moges, G. Ameta, and P. Witherell, “A Review of Model Inaccuracy and Parameter Uncertainty in Laser Powder Bed Fusion Models and Simulations,” *J. Manuf. Sci. Eng.*, vol. 141, no. 4, Apr. 2019, doi: 10.1115/1.4042789.

[45] C. Li, Z. Y. Liu, X. Y. Fang, and Y. B. Guo, “On the Simulation Scalability of Predicting Residual Stress and Distortion in Selective Laser Melting,” *J. Manuf. Sci. Eng.*, vol. 140, no. 4, Apr. 2018, doi: 10.1115/1.4038893.

[46] A. Olleak and Z. Xi, “A scan-wise adaptive remeshing framework for thermal simulation of the selective laser melting process,” *Int. J. Adv. Manuf. Technol.*, vol. 107, no. 1–2, pp. 573–584, Mar. 2020, doi: 10.1007/s00170-020-04995-7.

[47] J. L. Bartlett and X. Li, “An overview of residual stresses in metal powder bed fusion,” *Addit. Manuf.*, vol. 27, pp. 131–149, May 2019, doi: 10.1016/j.addma.2019.02.020.

[48] T. Q. Phan *et al.*, “Elastic Residual Strain and Stress Measurements and Corresponding Part Deflections of 3D Additive Manufacturing Builds of IN625 AM-Bench Artifacts Using Neutron Diffraction, Synchrotron X-Ray Diffraction, and Contour Method,” *Integr. Mater. Manuf. Innov.*, vol. 8, no. 3, pp. 318–334, Sep. 2019, doi: 10.1007/s40192-019-00149-0.

[49] T. Mukherjee, J. S. Zuback, W. Zhang, and T. DebRoy, “Residual stresses and distortion in additively manufactured compositionally graded and dissimilar joints,” *Comput. Mater. Sci.*, vol. 143, pp. 325–337, Feb. 2018, doi: 10.1016/j.commatsci.2017.11.026.

[50] D. D. Gu *et al.*, “components : materials , processes and mechanisms Laser additive manufacturing of metallic components : materials , processes and mechanisms,” vol. 6608, 2013, doi: 10.1179/1743280411Y.0000000014.

[51] T. Mukherjee, V. Manvatkar, and T. Debroy, “Scripta Materialia Mitigation of thermal distortion during additive manufacturing,” vol. 127, pp. 79–83, 2017, doi: 10.1016/j.scriptamat.2016.09.001.

[52] D. Buchbinder, W. Meiners, N. Pirch, K. Wissenbach, and J. Schrage, “Investigation on reducing distortion by preheating during manufacture of aluminum components using selective laser melting,” *J. Laser Appl.*, vol. 26, no. 1,

p. 012004, Feb. 2014, doi: 10.2351/1.4828755.

[53] J. Ning, D. E. Sievers, H. Garmestani, and S. Y. Liang, “Analytical modeling of transient temperature in powder feed metal additive manufacturing during heating and cooling stages,” *Appl. Phys. A Mater. Sci. Process.*, vol. 125, no. 8, pp. 1–11, 2019, doi: 10.1007/s00339-019-2782-7.

[54] C. Li, C. H. Fu, Y. B. Guo, and F. Z. Fang, “A multiscale modeling approach for fast prediction of part distortion in selective laser melting,” *J. Mater. Process. Technol.*, vol. 229, pp. 703–712, Mar. 2016, doi: 10.1016/j.jmatprotec.2015.10.022.

[55] C. Li, J. F. Liu, X. Y. Fang, and Y. B. Guo, “Efficient predictive model of part distortion and residual stress in selective laser melting,” *Addit. Manuf.*, vol. 17, pp. 157–168, Oct. 2017, doi: 10.1016/j.addma.2017.08.014.

[56] X. Liang, L. Cheng, Q. Chen, Q. Yang, and A. C. To, “A modified method for estimating inherent strains from detailed process simulation for fast residual distortion prediction of single-walled structures fabricated by directed energy deposition,” *Addit. Manuf.*, vol. 23, pp. 471–486, Oct. 2018, doi: 10.1016/j.addma.2018.08.029.

[57] Mechanical APDL 2019 R2, “Advanced Analysis Guide,” in *ANSYS® Academic Research Mechanical*, 2019.

[58] N. Keller and V. Ploshikhin, “New Method for Fast Predictions of Residual Stress and Distortion of AM Parts,” in *Proceeding of the 25th Solid Freeform Fabrication Symposium*, 2014, p. 1229.

[59] Q. Chen *et al.*, “An inherent strain based multiscale modeling framework for simulating part-scale residual deformation for direct metal laser sintering,” *Addit. Manuf.*, vol. 28, pp. 406–418, Aug. 2019, doi: 10.1016/j.addma.2019.05.021.

[60] M. Bugatti and Q. Semeraro, “Limitations of the inherent strain method in simulating powder bed fusion processes,” *Addit. Manuf.*, vol. 23, pp. 329–346, Oct. 2018, doi: 10.1016/j.addma.2018.05.041.

[61] R. K. Ganeriwala *et al.*, “Evaluation of a thermomechanical model for prediction of residual stress during laser powder bed fusion of Ti-6Al-4V,” *Addit. Manuf.*,

vol. 27, pp. 489–502, May 2019, doi: 10.1016/j.addma.2019.03.034.

[62] V. Premkumar, “Adapting Large Deflection Simulations Confidently with Nonlinear Adaptivity (NLAD).”

[63] D. Umbrello, R. M’Saoubi, and J. C. Outeiro, “The influence of Johnson–Cook material constants on finite element simulation of machining of AISI 316L steel,” *Int. J. Mach. Tools Manuf.*, vol. 47, no. 3–4, pp. 462–470, Mar. 2007, doi: 10.1016/j.ijmachtools.2006.06.006.

[64] T. Q. Phan *et al.*, “Elastic Residual Strain and Stress Measurements and Corresponding Part Deflections of 3D Additive Manufacturing Builds of IN625 AM-Bench Artifacts Using Neutron Diffraction, Synchrotron X-Ray Diffraction, and Contour Method,” *Integr. Mater. Manuf. Innov.*, vol. 8, no. 3, pp. 318–334, Sep. 2019, doi: 10.1007/s40192-019-00149-0.

[65] C. Li, E. R. Denlinger, M. F. Gouge, J. E. Irwin, and P. Michaleris, “Numerical verification of an octree mesh coarsening strategy for simulating additive manufacturing processes,” *Addit. Manuf.*, p. 100903, Oct. 2019, doi: 10.1016/j.addma.2019.100903.

[66] L. Dowling, J. Kennedy, S. O’Shaughnessy, and D. Trimble, “A review of critical repeatability and reproducibility issues in powder bed fusion,” *Mater. Des.*, vol. 186, p. 108346, Jan. 2020, doi: 10.1016/j.matdes.2019.108346.

[67] EOS and EOS GmbH - Electro Optical Systems, “Material data sheet - EOS Nickel Alloy IN625,” vol. 49, no. 0, pp. 1–5, 2011.

[68] E. O. S. Nickelalloy, E. O. S. Nickelalloy, P. Set, and P. Set, “Material Datasheet: EOS Nickel IN718,” *EOS GmbH Electro Opt. Syst. Tech. Rep., 2015. [Online]. Available http//www.eos.info/material-m*, vol. 49, no. 0, pp. 1–7, 2015.

[69] EOS GmbH, “Material Data Sheet for EOS Titanium Ti64,” vol. 49, no. 9011, pp. 1–4, 2007.

[70] I. Yadroitsev, L. Thivillon, P. Bertrand, and I. Smurov, “Strategy of manufacturing components with designed internal structure by selective laser melting of metallic powder,” *Appl. Surf. Sci.*, vol. 254, no. 4, pp. 980–983, 2007, doi: 10.1016/j.apsusc.2007.08.046.

[71] D. Zhang, W. Niu, X. Cao, and Z. Liu, “Effect of standard heat treatment on the microstructure and mechanical properties of selective laser melting manufactured Inconel 718 superalloy,” *Mater. Sci. Eng. A*, vol. 644, pp. 32–40, Sep. 2015, doi: 10.1016/j.msea.2015.06.021.

[72] A. Roguev *et al.*, “Epistasis Map in Fission Yeast,” *October*, vol. 405, no. 2008, pp. 127–136, 2009, doi: 10.1016/S0924-0136(97)00302-6.

[73] H. K. Farahani, M. Ketabchi, and S. Zangeneh, “Determination of Johnson–Cook Plasticity Model Parameters for Inconel718,” *J. Mater. Eng. Perform.*, vol. 26, no. 11, pp. 5284–5293, Nov. 2017, doi: 10.1007/s11665-017-2990-2.

[74] H. R. Abedi, A. Z. Hanzaki, M. Azami, M. Kahnooji, and D. Rahmatabadi, “The high temperature flow behavior of additively manufactured Inconel 625 superalloy,” *Mater. Res. Express*, vol. 6, no. 11, 2019, doi: 10.1088/2053-1591/ab44f6.

[75] G. R. Johnson and W. H. Cook, “A Computational Constitutive Model and Data for Metals Subjected to Large Strain, High Strain Rates and High Pressures,” *Seventh Int. Symp. Ballist.*, pp. 541–547, 1983.

[76] NIST, “ADDITIVE MANUFACTURING BENCHMARK TEST SERIES (AM-BENCH).” [Online]. Available: https://www.nist.gov/ambench.

[77] NIST, “AMB2018-01 Description.” [Online]. Available: https://www.nist.gov/ambench/amb2018-01-description.

[78] Y. Yang, M. Allen, T. London, and V. Oancea, “Residual Strain Predictions for a Powder Bed Fusion Inconel 625 Single Cantilever Part,” *Integr. Mater. Manuf. Innov.*, vol. 8, no. 3, pp. 294–304, 2019, doi: 10.1007/s40192-019-00144-5.

[79] A. Olleak and Z. Xi, “Efficient LPBF process simulation using finite element modeling with adaptive remeshing for distortions and residual stresses prediction,” *Manuf. Lett.*, vol. 24, pp. 140–144, Apr. 2020, doi: 10.1016/j.mfglet.2020.05.002.

[80] J.-P. Kruth, J. Deckers, E. Yasa, and R. Wauthlé, “Assessing and comparing influencing factors of residual stresses in selective laser melting using a novel analysis method,” *Proc. Inst. Mech. Eng. Part B J. Eng. Manuf.*, vol. 226, no. 6, pp. 980–991, Jun. 2012, doi: 10.1177/0954405412437085.

[81] K. Zeng, D. Pal, and B. Stucker, “A review of thermal analysis methods in Laser Sintering and Selective Laser Melting,” *Solid Free. Fabr. Symp.*, pp. 796–814, 2012, doi: 10.1109/OCEANSSYD.2010.5603594.

[82] J. Hensman, R. Mills, S. G. Pierce, K. Worden, and M. Eaton, “Locating acoustic emission sources in complex structures using Gaussian processes,” *Mech. Syst. Signal Process.*, vol. 24, no. 1, pp. 211–223, Jan. 2010, doi: 10.1016/j.ymssp.2009.05.018.

[83] J. Yu, “State of health prediction of lithium-ion batteries: Multiscale logic regression and Gaussian process regression ensemble,” *Reliab. Eng. Syst. Saf.*, vol. 174, pp. 82–95, Jun. 2018, doi: 10.1016/j.ress.2018.02.022.

[84] Y. Wang, W. Zhao, G. Zhou, Q. Gao, and C. Wang, “Optimization of an auxetic jounce bumper based on Gaussian process metamodel and series hybrid GA-SQP algorithm,” *Struct. Multidiscip. Optim.*, vol. 57, no. 6, pp. 2515–2525, Jun. 2018, doi: 10.1007/s00158-017-1869-z.

[85] Y. Xiong, W. Chen, K.-L. Tsui, and D. W. Apley, “A better understanding of model updating strategies in validating engineering models,” *Comput. Methods Appl. Mech. Eng.*, vol. 198, no. 15–16, pp. 1327–1337, Mar. 2009, doi: 10.1016/j.cma.2008.11.023.

[86] B. C. Jung, J. Park, H. Oh, J. Kim, and B. D. Youn, “A framework of model validation and virtual product qualification with limited experimental data based on statistical inference,” *Struct. Multidiscip. Optim.*, vol. 51, no. 3, pp. 573–583, Mar. 2015, doi: 10.1007/s00158-014-1155-2.

[87] Z. Xi, H. Pan, and R.-J. Yang, “Time dependent model bias correction for model based reliability analysis,” *Struct. Saf.*, vol. 66, pp. 74–83, May 2017, doi: 10.1016/j.strusafe.2017.02.001.

[88] S. Bae, N. H. Kim, and S. Jang, “Reliability-based design optimization under sampling uncertainty: shifting design versus shaping uncertainty,” *Struct. Multidiscip. Optim.*, vol. 57, no. 5, pp. 1845–1855, May 2018, doi: 10.1007/s00158-018-1936-0.

[89] Z. Xi, “Model-Based Reliability Analysis With Both Model Uncertainty and

Parameter Uncertainty," *J. Mech. Des.*, vol. 141, no. 5, May 2019, doi: 10.1115/1.4041946.

[90] M. C. Kennedy and A. O'Hagan, "Bayesian calibration of computer models," *J. R. Stat. Soc. Ser. B (Statistical Methodol.*, vol. 63, no. 3, pp. 425–464, Aug. 2001, doi: 10.1111/1467-9868.00294.

[91] J. Quiñonero-Candela and C. E. Rasmussen, "A Unifying View of Sparse Approximate Gaussian Process Regressio," *J. Mach. Learn. Res.*, vol. 6, pp. 1939–1959, 2005.

[92] S. Ferson, W. L. Oberkampf, and L. Ginzburg, "Model validation and predictive capability for the thermal challenge problem," *Comput. Methods Appl. Mech. Eng.*, vol. 197, no. 29–32, pp. 2408–2430, May 2008, doi: 10.1016/j.cma.2007.07.030.

[93] Z. Xi, C. Hu, and B. D. Youn, "A comparative study of probability estimation methods for reliability analysis," *Struct. Multidiscip. Optim.*, vol. 45, no. 1, pp. 33–52, Jan. 2012, doi: 10.1007/s00158-011-0656-5.